Field and Current Induced Magnetization Reversal in Patterned Pseudo Spin Valve Devices

by

Irénée A. Colin

Ingénieur de l'Ecole Polytechnique
Palaiseau, France.

SUBMITTED TO THE DEPARTMENT OF MATERIALS SCIENCE AND ENGINEERING IN PARTIAL FULFILLMENT OF THE REQUIREMENTS FOR THE DEGREE OF

MASTER OF SCIENCE IN MATERIALS SCIENCE AND ENGINEERING
AT THE
MASSACHUSETTS INSTITUTE OF TECHNOLOGY

JUNE 2007

Signature of Author: _____
Department of Materials Science and Engineering
22nd May, 2007

Certified by: _____
Caroline A. Ross
Professor of Materials Science and Engineering
Thesis Supervisor

Accepted by: _____
Samuel M. Allen
POSCO Professor of Physical Metallurgy
Chair, Departmental Committee on Graduate Students

Abstract.

The field and current induced magnetization switchings of Pseudo-Spin-Valve (PSV) devices are described in this dissertation. An aligned sequence of three (one optical and two electron-beam) lithographies was used to define the devices and their electrical contacts. The PSV stack comprised a layer of soft ferromagnetic material $Ni_{80}Fe_{20}$ (NiFe or Py), a non-magnetic spacer layer of Cu, a hard ferromagnetic layer of Co and a capping layer of Au. The current flowed in plane (CIP) and the devices displayed giant magnetoresistance (GMR). Three different shapes were investigated: notched bars, elliptical rings and rhomboidal rings.

In the bars, the notches provided strong pinning potential wells for transverse domain walls in the NiFe layer, which, upon cycling an external field, reversed in a step-like fashion, with domain walls nucleating from both ends of the bars, due to strong magnetostatic coupling between both magnetic layers. Additional important magnetostatic coupling effects were measured and micromagnetic simulations confirmed the ubiquity of such coupling. Current induced magnetic switching (CIMS) experiments were conducted, and threshold densities of the order of 10^{11} A/m^2 were used to switch the magnetization under an external bias field, and the critical current decreased with increasing bias. Simulations showed that the Oersted field generated by the current was sufficiently strong to switch the magnetization in the soft NiFe layer, without taking into account spin-transfer torque effects.

Ring shaped devices allowed for a diversity of responses depending on the contact configurations used which may be divided into two categories: the classical configurations and the Wheatstone bridge configurations. The latter allowed for large effective GMR ratios up to 200 %, with low switching fields down to a few Oersted. Both types of contact configuration along with micromagnetic simulations enabled a deep understanding of the field-induced reversal of both elliptical and rhomboidal rings. Magnetostatic coupling effects were also found to play a key role. CIMS experiments were conducted, and the rhomboidal ring device successfully switched, in the Wheatstone bridge configuration, under zero bias with a threshold current density of the order of 10^{11} A/m^2. The density and length of current pulses was found to change the critical current density, which suggested that the spin structure of the domain walls in the NiFe layer was modified by the current.

Table of Contents.

Chapter 1

Introduction

1.1 Magnetic Random Access Memories.

1.2 Magnetic sensors and logic devices.

1.3 Thesis Overview.

Spintronics is a new field of physics that combines electrical transport phenomena and magnetism through the spin of the electrons. The idea is to exploit the extra degree of freedom of the electron: its spin. Spin-polarized current is an interesting example of how magnetism can modify electrical transport properties. In a ferromagnetic material, the spins of the conduction electrons will have a higher probability of being aligned with the local magnetization. Moreover, the spin of the electron shows a long coherence (relaxation time): it tends to stay up or down for a long time (compared to orbital states which are modified by scattering processes). Such properties can be utilized to generate very important magnetoresistive effects, i.e. a change of resistance as a function of the magnetization state of the device measured. For instance, giant magnetoresistance (GMR) and tunneling magnetoresistance arise in multilayered thin film structures such as Pseudo Spin Valves (PSV), Spin Valves (SV) or Magnetic Tunnel Junctions (MTJ) and can be used in devices that display very high sensitivity to changing magnetic field. Read heads for high-capacity hard drives rely on the GMR effect. A great advantage of devices displaying TMR and GMR is that they can be tailored in terms of switching field and magnitude of the magnetoresistive change amplitude by adapting the materials in each layer, the thicknesses of each layer, the layer sequence, as well as the device geometry.

Magnetic Random Access Memories (MRAM), magnetic sensors and to some lesser extent magnetic logic devices mostly rely on such phenomena as GMR and TMR. In the rest of this chapter, an overview of these applications is provided.

1.1 Magnetic Random Access Memories.

1.1.1 Description.

Random Access Memories (RAM) are able to write and read a memory bit like any memory, but they also allow the stored data to be accessed very fast independently of the physical position of the particular memory bit that needs to be written or read, therefore without the physical movement of the storage medium or a physical reading head like in a hard drive. Because of these characteristics, RAM is used as primary storage in computers: it is used for loading, displaying and manipulating applications and data. The disadvantages of classical RAM over physically moving media are its cost, and the loss of data when power is turned off. For these reasons, computers have disc storage as "secondary storage".

Magnetic Random Access Memory (MRAM) is likely to be the next type of RAM, since it retains the magnetic information even when the power is switched off and, unlike non-volatile memories such as Flash memories, it needs low write and erase voltages, displays very high writing speed, and high write-erase endurance. The most likely competitor of MRAM is Ferromagnetic RAM (FRAM), but MRAM promises to be denser and more robust.

The first generation of MRAM developed by Honeywell in the mid 1980s relied on anisotropic magnetoresistance (AMR). After the discovery of GMR, a new generation of faster and denser MRAM rose. The last generation of MRAM uses TMR in magnetic tunneling junctions (MTJ) cells. For these MRAMs, the reading is done by measuring the

resistance of the device while the writing is done by applying a local field provided by current flowing through wires placed on top and/or bottom of each cell.

1.1.2 Pseudo Spin Valve (PSV) MRAM.

A Pseudo Spin Valve is a multilayer structure that comprises two different ferromagnetic layers (by using different ferromagnetic materials and/or different thicknesses in each layer) separated by a non magnetic conductive spacer layer. One of the ferromagnetic layers is designed to be magnetically softer than the other so that it can be cycled with an external field while the harder layer remains unchanged. Such a structure displays GMR if the thickness of each layer is well below the mean free path of the electron and its spin coherence length. When the magnetizations in each ferromagnetic layer are aligned parallel, the resistance is at its lowest value $R_{\uparrow\uparrow}$ and when antiparallel, the resistance of the PSV is at its highest point $R_{\uparrow\downarrow}$. We define the maximum GMR ratio as:

$$r_{GMR} = \frac{R_{\uparrow\downarrow} - R_{\uparrow\uparrow}}{R_{\uparrow\uparrow}} \tag{1.1}$$

Typical ratios of 6% to 10% were obtained [1]. Reading was done by measuring the resistance of the PSV with a current in plane (CIP) called the sense current. The writing was achieved using the Oersted field that the current going through the word lines generated. Fig. 1.1 describes the writing of one memory bit.

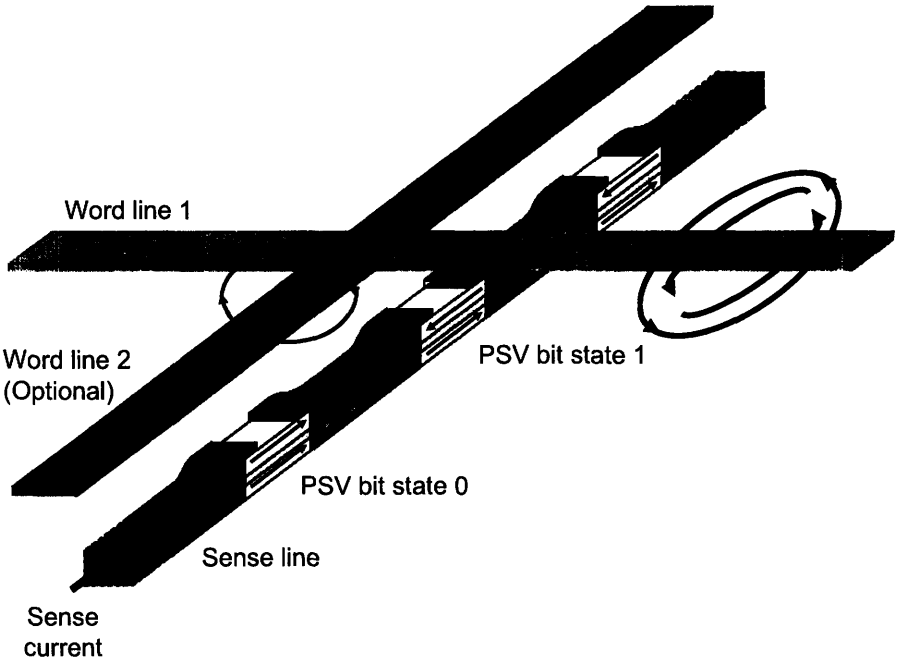

Figure 1.1: Reading and writing procedure of a PSV memory bit in an MRAM. Schematics show the Oersted field resulting from the current going through the word lines.

Applying a current through both word lines will allow the writing of one and only one memory bit (i.e. the one sitting underneath the intersection of the two word lines). The architecture of such MRAMs is therefore simple and can be dense [1] as illustrated in Fig. 1.2. An alternative method used to write is to use only one word line (word line 1) and increase the sensing current so that the sum of their Oersted fields enables the switching.

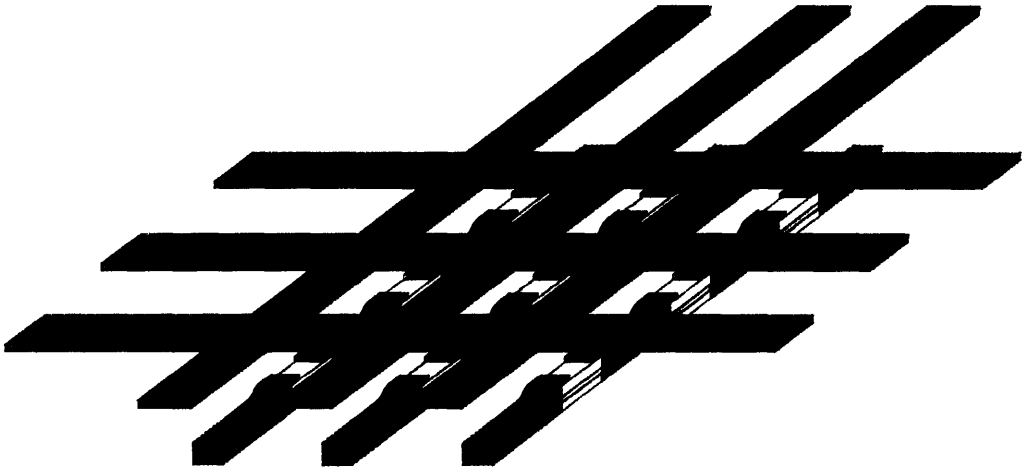

Figure 1.2: Architecture of a few bits in a PSV MRAM.

Such MRAM structures have a very good read access time (which is directly related to the GMR ratio of the unit cell) of few tens of ns [2]. However, spin dependent tunneling (SDT) devices display significantly higher magnetoresistance ratios and have thus the potential for higher speed.

1.1.3 Magnetic Tunnel junction (MTJ) MRAM

SDT devices, namely Magnetic Tunneling Junctions (MTJ) have recently been shown to display over 300% magnetoresistance (TMR) ratios [3]. An MTJ comprises also a hard and soft magnetic layer, but unlike in PSVs, those are separated by a thin layer of insulator (Al_2O_3 or MgO). The hard layer is usually pinned by an antiferromagnetic layer called the pinning layer. The sensing current flows perpendicular to the plane (CPP), which complicates the architecture for MRAM using such devices. The stack is patterned as an ellipse, geometry very convenient since the single domain approximation is mostly valid [4]. The writing procedure is similar to the one used in PSV MRAM. Typically, a technique called Toggle (with better selectivity to switch just one bit) is used to generate the rotation of the magnetization in the free layer. The hard axis field (word line current pulse Fig 1.3) is applied a little before the easy axis field (bit line current pulse Fig 1.3) is added, thus allowing a more homogeneous rotation of the magnetization. The current going through an MTJ must be less than 1mA to prevent heating as well as the dielectric breakdown [2]. Thus, when writing a memory bit, the sensing current cannot be used as in PSV MRAM to help switch the free layer. A transistor is placed on the sense line

below the MTJ: when the transistor is on, a low current is going through the MTJ, the memory bit is in reading mode. When the transistor is off, a higher current flows in the bit line, the memory bit is in writing mode, no current goes through the MTJ. A schematic of an MTJ memory bit in writing mode is given in Fig. 1.3.

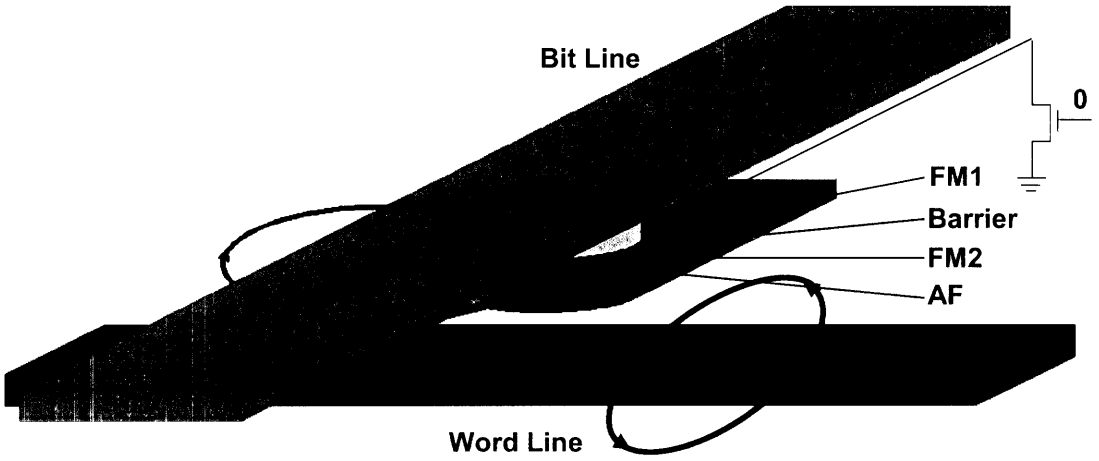

Figure 1.3: A single bit of an MTJ MRAM in writing mode with the transistor off. An MTJ is usually composed of an antiferromagnetic layer (AF) pinning a ferromagnetic layer called the pinned layer (FM2), separated from the free layer (FM1) by a thin insulating layer (Barrier).

Low time constants below 1ns can be attained in such MRAMs [5]. The drawback of SDT MRAM is a lower density than PSV MRAM due to the need for an individual transistor in each bit.

A different writing scheme was recently proposed and is intensely studied [6]. In this scheme, instead of switching the free layer of the MTJ via the Oersted field generated by the currents flowing in the word and bit lines, the switching is done directly by the electrons of the current going through the MTJ via a phenomena called spin transfer torque (STT). Such MRAMs are named STT-MRAM and may prove to be denser than classical SDT-MRAMs.

Alternative MRAMs are being investigated such as vertical MRAM (VMRAM) [7,8]. The idea finds its origins in the core memories invented by A. Wang, and was adapted to the patterned thin film research field by means of a magnetoresistive multilayer stack of patterned rings. The flux-closure magnetization state of a ferromagnetic ring is the so-called "vortex state" in which the magnetization is circular, either clockwise or counter clockwise. The high and low GMR state will correspond to successive rings having respectively opposite and identical vortex chiralities. In the vortex state, there is no stray field whatsoever, allowing such MRAM to be theoretically extremely dense. The main problem with this theoretical expectation is that small and narrow ferromagnetic rings have other stable magnetization states involving domain walls and therefore stray fields [8]. However, such intermediate states displaying therefore intermediate stable resistance

levels can be used to create memory cells that store more than 2 bits, thus compensating the loss of density by a gain in bits per cell. Moreover, reversing the free layer from clockwise vortex to anticlockwise vortex and back is not simple and complicated space consuming bit and word line designs have been proposed. The theoretical density is thus very unlikely to be ever reached.

GMR and TMR prove to have a promising future in different type of MRAMs. It also shows very interesting possibilities in sensors and logic devices, as detailed in the following section.

1.2 Magnetic sensors and logic devices.

1.2.1 Magnetic sensors.

The greatest industrial success of spintronics to date resides in one very particular sensor, namely the GMR read head for high density hard drives first developed and introduced by IBM in 1997 [10]. It is a 'digital' type sensor: it measures two opposite directions of small stray fields, corresponding to memory bits being in state 0 or 1, and resistance of the GMR being low $R_{\uparrow\uparrow}$ or high $R_{\uparrow\downarrow}$. Figure 1.4 gives schematics of such a device.

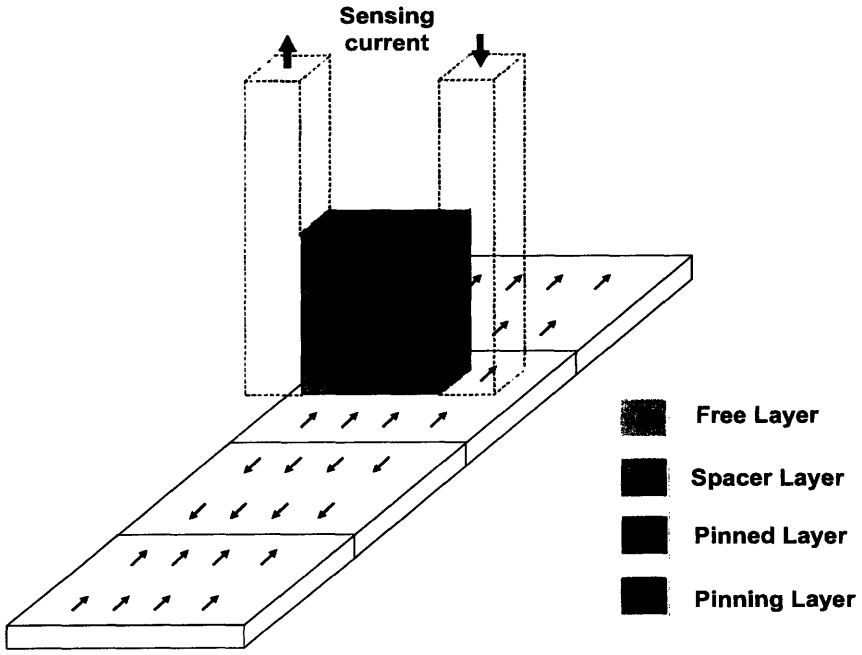

Figure 1.4: GMR reading head schematics. The stray fields emerging at the domain boundaries switch the magnetization of the free layer.

Another type of GMR sensor uses a different type of architecture that has the property of being at remanence (no applied field) in the high resistance state $R_{\perp}$ (the magnetostatic coupling between the two layer that depends on the spacer thickness is strong enough to overcome the shape anisotropy of the soft layer) [11]. This sensor is an 'analogous' type sensor: it measures the change in field as a gradual change in resistance. The sensor proposed comprises four identical GMR devices forming a Wheatstone bridge, and in each branch one of then is shielded from external magnetic field. An even more sensitive device [12] has been proposed that can detect and measure picotesla field using an MTJ device.

A concept that would utilize 360° domain walls for sensing purposes has been proposed [13]. It can measure an in plane revolution of a small magnetic field.

1.2.2 Magnetic logic.

Magnetic logic is mostly yet to be explored. A few concept have been proposed, the most interesting of which is the so-called 'chameleon processor' [14]. The logic element is based on a single MRAM cell as can be seen in Fig 1.5. The only difference resides in two additional word lines. Two word lines can reverse the soft layer but three are needed to reverse also the hard layer. Such a device can be set to operate either as an AND, or an OR, or a NAND or a NOR gate, hence the name chameleon.

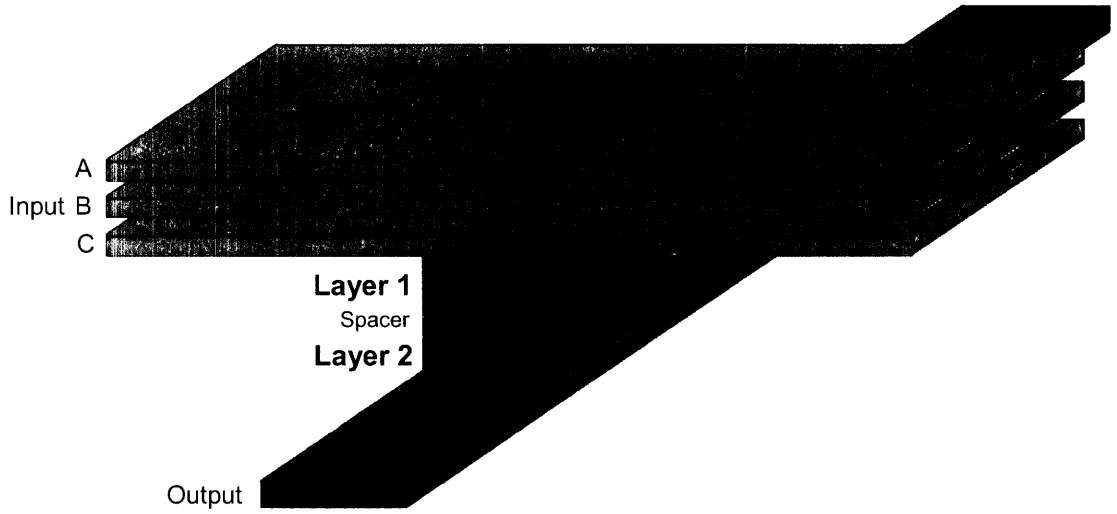

Figure 1.5: A single GMR logic cell with input lines A, B and C, and an output line. The thicker layer 1 is the soft layer.

Configuring the cell as in Fig1.5 can be achieved in a two step setting process: first a positive current is passed in the three word lines A, B and C, which configures the PSV in a parallel state with the magnetizations oriented like the one in the hard layer in Fig

1.5. Then a negative current is passed through both A and B, reversing only the soft layer 1.

Defining the 0 and 1 inputs as a negative and positive currents respectively, and the high and low PSV resistance as a 0 and 1 output respectively, the cell is then an AND gate:

A	B	Out
0	0	0
1	0	0
0	1	0
1	1	1

Programming the cell only with the first step of the AND setting, namely passing a positive current through all three word lines, generates an NAND gate.

A	B	Out
0	0	1
1	0	1
0	1	1
1	1	0

This concept is extremely interesting, but when the cell is set for instance in an AND mode, it has to be reset after being used, even if it is to keep the same AND functionality.

Other concepts have been proposed [15-17] and special attention has been brought on Magnetic Quantum Cellular Automata (MQCA), where magnetic 'dots' can 'communicate' their magnetization state to their neighbors (through magnetostatic interactions). MQCA is still only a very specific concept and realistic device concepts are yet to be imagined.

1.3 Thesis overview

This thesis is the experimental study of a range of patterned PSV devices and their behavior with an external bias field and internal current pulses. Chapter 2 gives an overview of ferromagnetism and an understanding of domains and domain walls. The mechanism of GMR is also explained, as well as the dynamics of micromagnetism and an introduction to the spin transfer torque phenomenon.

Chapter 3 describes how the devices were fabricated and how the methods used to characterize them.

Chapter 4 gives a detailed review of the results obtained for two PSV bars of 2.14 micrometers long and 270 nm wide.

Chapter 5 compares the field and current induced behaviors of PSV rings of two different shapes: elliptical and rhomboidal. Different contact configurations are explored, giving interesting GMR responses.

Finally, this dissertation ends with a conclusion giving an overview of the results obtained.

[1] B. A. Everitt, and A. V. Pohm, J. Vac. Sci. **16**, 1794-1800 (1998).
[2] J.M. Daughton, A. V. Pohm, R.T. Fayfield, and C. H. Smith, J. Phys. D **32**, R169-R177 (1999).
[3] S. S. P. Parkin, C. Kaiser, A. Panchula, P. M. Rice, B. Hughes, M. Samant, and S. H. Yang, Nat. Mat. **3** (12), 862-867 (2004).
[4] O. Fruchart, and A. Thiaville, C. R. Physique **6**, 921-933 (2005).
[5] S. S. P. Parkin, Intermag. Conf. paper GA-01 (1999).
[6] Z. Diao, Z. Li, S. Wang, Y. Ding, A. Panchula, E. Chen, L-C. Wang, and Y. Huai, J. Phys. Condens. Matter. **19**, 165209 (2007).
[7] M.T. Moneck, and J. G. Zhu, J. Appl. Phys. **99**, 08H709 (2006).
[8] J. M. Anderson, D. J. Brownell, G. A. Prinz, H. Huggins, L. V. Van, J. A. Christodoulides, and J. G. Zhu, J. Appl. Phys. **97**, 10P504 (2005).
[9] C.A. Ross, F.J. Castaño, D. Morecroft, W. Jung, H. I. Smith, T. A. Moore, T. J. Hayward, J. A. C. Bland, T. J. Bromwich, and A. K. Petford-Long, J. Appl. Phys. **99**, 08S501 (2006).
[10] S. S. P. Parkin, Annual Reviews of Mat. Sci. **25**, 357-388 (1995).
[11] J. M. Daughton, J. Brown, E. Chen, R. S. Beech, A. V. Pohm, and W. Kude, IEEE Trans. Magn. Vol **30** (6), 4608 (1994).
[12] M. Tondra, J. M. Daughton, D. X. Wang, R. S. Beech, A. Fink, and J. A. Taylor, J. Appl. Phys. Vol **83** (11), 6688 (1998).
[13] M. Diegel, R. Mattheis, and E. Halder, IEEE Trans. Magn. Vol **40** (4), 2655 (2004).
[14] A. Ney, C. Pampuch, R. Koch, and K. H. Ploog, Nature **425**, 485 (2003).
[15] D.A. Allwood, G. Xiong, M. D. Cooke, C. C. Faulkner, D. Atkinson, N. Vernier, and R. P. Cowburn, Science **296**, 2003 (2002).
[16] R.P. Cowburn, and M. E. Welland, Science **287**, 1466 (2000).
[17] A. Imre, G. Csaba, L. Ji, A. Orlov, G. H. Bernstein, W. Porod, Science **311**, 205 (2006).

Chapter 2

Overview on Ferromagnetism and Interactions between current and local magnetization.

2.1 Ferromagnetism and domain structures.

2.1.1 Classification of magnetic materials.
2.1.2 Exchange coupling in ferromagnetic materials.
2.1.3 Demagnetizing field.
2.1.4 Shape anisotropy.
2.1.5 Crystal anisotropy.
2.1.6 Surface anisotropy.
2.1.7 Magnetoelastic anisotropy.
2.1.8 Exchange anisotropy.
2.1.9 Energetics of a ferromagnet and its domain structure.

2.2 Interactions between current and local magnetization.

2.2.1 Band structure of transition metals.
2.2.2 Introduction to electronic transport in magnetic materials.
2.2.3 Effect of the current on the local magnetization.

2.1 Ferromagnetism and domain structures.

2.1.1 Classification of magnetic materials.

We define the local **magnetization** of a material:

$$\boxed{\vec{M}(\vec{r}) = \frac{\delta\vec{\mu}}{\delta V}} \tag{2.1}$$

where $\vec{\mu} = \sum_{atoms} \vec{\mu}_i$ is the magnetic moment of the volume δV located around $\vec{r}$. The units of the magnetization are Amperes per meters.
We then define the **bulk magnetic susceptibility** tensor as

$$\boxed{\vec{M} = \overline{\overline{\chi}} \bullet \vec{H}} \tag{2.2}$$

with

$$\chi_{ij} = \frac{\partial M_i}{\partial H_j} \tag{2.3}$$

where H is the magnetic field.
When the susceptibility is just a scalar, the magnetization and the field are parallel.

Depending on that susceptibility and its temperature dependance, one can sort materials into five different magnetic categories.

2.1.1.1 Diamagnetic materials. $\chi < 0$ and small (-10^{-5}).

When no external field is applied, the unit elements (e.g. the atoms) of a diamagnetic material have no individual magnetic moment, and when a field is applied, following Lenz's law, the orbital momentum will behave so as to generate a field opposed to the applied field, hence leading to a very weak and negative susceptibility. E.g. Bismuth, gold, copper.

2.1.1.2 Paramagnetic materials. $\chi > 0$ and small (10^{-4})

When no external field is applied, each unit element of a paramagnetic material has an individual magnetic moment, but there is no long range order, so at room temperature, their random alignment generates a net zero magnetization. However, when an external field is applied, in order to lower their energy, the individual magnetic moments align with the external field, fighting the thermal disorder effect, thus leading to a small and positive susceptibility. E.g. Aluminium.

2.1.1.3 Ferromagnetic materials. $\chi > 0$ and typically large (10^3)

When no external field is applied, each unit element of ferromagnetic materials has an individual magnetic moment, and, below the Curie temperature, there is a long range order due to exchange interaction (further discussed in section 2.1.2) which favors their parallel alignment, creating thus a net local magnetization. However, the local magnetization can organize into domains in order to minimize its energy (further discussed in section 2.1.9), and the magnetization of the whole sample can be 0. But if an external field is applied, the domains whose magnetization is most parallel to the field will grow at the expense of the others, leading to a net magnetization parallel to the field. Above the Curie temperature, a ferromagnet behaves like a paramagnet. E.g. Cobalt, Permalloy.

2.1.1.4 Antiferromagnetic materials. $\chi > 0$ and small.

When no external field is applied, the unit elements of paramagnetic materials each have individual magnetic moment, and below the Néel temperature, there is a long range order due to exchange interaction that favors their antiparallel alignment, creating thus a zero local magnetization. Just as ferromagnetic materials, antiferromagnets organize into domains. But if an external field is applied, the domains in which each individual spin is most parallel and antiparallel to the field will grow at the expense of the others, and each individual magnetic moment parallel to the field will be stabilized, whereas all antiparallel moments will become unstable and will eventually all flip to the parallel position as the field increases, leading to a net magnetization parallel to the field, thus leading to a small and positive susceptibility, with a very different temperature behavior than paramagnetic susceptibility. E.g. Chromium.

2.1.1.5 Ferrimagnetic materials. $\chi > 0$ and big.

They are ionic solids displaying different sublattices between which the moments are antiparallel like antiferromagnets but of different magnitude thus leading to a net magnetization. Their behaviour is very similar to that of ferromagnetic materials even with temperature. As the temperature decreases, some ferrimagnet display a point where the magnetization cancels. It is called the magnetization compensation point. E.g. Magnetite Fe_3O_4.

2.1.2 Exchange coupling in ferromagnetic materials.

In quantum mechanics, ferromagnetic and antiferromagnetic behaviour can be described by considering the Heisenberg Hamiltonian:

$$\hat{H} = -\frac{1}{2}\sum_{i,j,i\neq j} J(\vec{r}_{ij})\hat{\vec{S}}_i \bullet \hat{\vec{S}}_j \tag{2.4}$$

where $\hat{\vec{S}}_i$ and $\hat{\vec{S}}_j$ are the atomic spins at the *i*th and *j*th lattice sites and $J(\vec{r}_{ij})$ is called the **exchange integral** for the *i*th and *j*th atoms. It is usually negligible when the *i*th and *j*th atoms are not neighbours.

If $J(\vec{r}_{ij}) > 0$ for every pair of neighbouring atoms, parallel alignment is favored, thus leading to a ferromagnetic crystal.

If $J(\vec{r}_{ij}) < 0$ for every pair of neighbouring atoms, antiparallel alignment is favored, thus leading to an antiferromagnetic crystal.

This exchange coupling phenomenon is in fact a consequence of the **Pauli exclusion principle** and can be deduced from a purely electrostatic Hamiltonian in the example of the **hydrogen molecule** in the Heitler-London approximation (1927). This example is thoroughly studied in Appendix A.

This example shows how the purely quantum mechanical effect of electron exchange associated with the Pauli exclusion principle leads to interactions dependant on the relative alignment of the spins, even though the Hamiltonian does not contain any spin variable.

As seen in the case of the hydrogen molecule (A.22), **the Hamiltonian of a crystal is equivalent to the exchange Hamiltonian** (2.4) **for low energy levels** (temperature well below the Curie temperature) generating the correct energy spectrum of a magnetically ordered crystal near the ground state.

This exchange coupling does explain why a ferromagnetic material locally has a net magnetic moment, but does not account for the presence of a domain structure nor for a preferred orientation of the magnetization. The demagnetizing field is responsible for the arising of a domain structure and for the so-called shape anisotropy. The magnetization orientation also depends on the direction of the external field, on magnetocrystalline anisotropy, on surface anisotropy, on magnetoelastic anisotropy and in specific cases, on exchange anisotropy.

2.1.3 Demagnetizing field.

The magnetization of a ferromagnetic sample generates a magnetic field usually called the stray field when considering the field outside of the sample and the demagnetizing field when considering the field within the sample itself.

2.1.3.1 Theoretical calculation.

Maxwell's equations in a material can be written:

$$\vec{\nabla} \bullet \vec{D} = \rho \tag{2.5}$$

$$\vec{\nabla} \bullet \vec{B} = 0 \tag{2.6}$$

$$\vec{\nabla} \times \vec{E} = -\frac{\partial \vec{B}}{\partial t} \tag{2.7}$$

$$\vec{\nabla} \times \vec{H} = \vec{J} + \frac{\partial \vec{D}}{\partial t} \tag{2.8}$$

where $\vec{E}$ is the electric field, $\vec{D}$ the electric displacement, $\vec{H}$ the magnetic field, $\vec{B}$ the magnetic induction, ρ the volume electric charge distribution, $\vec{J}$ the current density.

$\vec{E}$ and $\vec{D}$ are related through the electrical polarization $\vec{P}$ by

$$\vec{D} = \varepsilon_0 \cdot \vec{E} + \vec{P} \tag{2.9}$$

$\vec{H}$ and $\vec{B}$ are related through the magnetization $\vec{M}$ by

$$\boxed{\vec{B} = \mu_0 \cdot \left(\vec{H} + \vec{M}\right)} \tag{2.10}$$

(2.6) implies

$$\vec{\nabla} \bullet \vec{M} = -\vec{\nabla} \bullet \vec{H} \tag{2.11}$$

With $\rho = 0$, we simplify (2.5) $\vec{\nabla} \bullet \vec{D} = 0$

We assume in the following discussion that the displacement current $\frac{\partial \vec{D}}{\partial t}$ is null.

(2.5) implies that one can define a potential vector usually named $\vec{A}$ such that

$$\boxed{\vec{\nabla} \times \vec{A} = \vec{B}} \tag{2.12}$$

to which is usually added the Coulomb gauge to define a unique potential vector:

$$\vec{\nabla} \bullet \vec{A} = 0 \tag{2.13}$$

Implementing (2.12) and (2.10) into (2.8), neglecting any free current, we obtain:

$$-\vec{\nabla}^2 \vec{A} = \mu_0 \cdot \nabla \times \vec{M} \tag{2.14}$$

If we therefore consider only the contribution of the magnetization, Poisson gives

$$\vec{A} = \frac{\mu_0}{4 \cdot \pi} \cdot \iiint_V \frac{\vec{\nabla} \times \vec{M}}{|\vec{r} - \vec{r}\,'|} d^3\vec{r}\,' + \iint_S \frac{\vec{M} \times \vec{n}}{|\vec{r} - \vec{r}\,'|} d^2 S \tag{2.15}$$

where $\vec{n}$ is the unit vector normal in each point to the closed surface, oriented outwards. The vector potential created by the magnetization is thus equivalent to that created by a current distribution of volume density $\vec{j}_v = \nabla \times \vec{M}$ and surface density $\vec{j}_s = \vec{M} \times \vec{n}$.

(2.15) can be further simplified:

$$\vec{A} = \frac{\mu_0}{4 \cdot \pi} \cdot \iiint_V \frac{\vec{M}(\vec{r}\,') \times (\vec{r} - \vec{r}\,')}{|\vec{r} - \vec{r}\,'|^3} d^3\vec{r}\,' \tag{2.16}$$

The total magnetic field will be the sum of the field created by the magnetization, the field created by the free current $\vec{J}$, called the Oersted field, and the externally applied field.

Implementing (2.16) into (2.12) and the result into (2.10), one can obtain **the magnetic field created by the magnetization of the sample inside that very sample, which is called the demagnetizing field** since it is in the opposite direction from the magnetization (hence usually from the external applied field along which the magnetization tends to align itself).

M Beleggia et al. [1] propose a Fourier space approach to efficiently calculate these last steps.

$$\vec{A}(\vec{k}) = \frac{i \cdot \mu_0}{k^2} \cdot \vec{M}(\vec{k}) \times \vec{k} \tag{2.17}$$

which implies that

$$\vec{H}_{demag} = -\frac{1}{8\pi^3} \iiint \frac{\vec{k}}{k^2} \left(\vec{M}(\vec{k}) \bullet \vec{k} \right) e^{i\vec{k} \bullet \vec{r}} \cdot d^3\vec{k} \tag{2.18}$$

If we assume that a uniform magnetization in the sample will generate a uniform field, defining a dimensionless shape function $D(\vec{r})$ (equal to unity inside our sample and 0 outside) allows us to calculate the **demagnetizing tensor** defined by :

$$\vec{H}_{demag} = -\overline{\overline{N}} \cdot \vec{M} \tag{2.19}$$

$$N_{ij} = \frac{1}{8\pi^3} \iiint \frac{k_i k_j}{k^2} D(\vec{k}) e^{i\vec{k} \bullet \vec{r}} \cdot d^3\vec{k} \tag{2.20}$$

In the case of uniform magnetization, since $\overline{\overline{N}}$ is positive and symmetric, it can be diagonalized, and therefore along its main axes,

$$H_{i_{demag}} = -N_i \cdot M_i \tag{2.21}$$

with

$$N_1 + N_2 + N_3 = 1 \tag{2.22}$$

2.1.3.2 Calculation inside a uniformly magnetized sphere.

For any ellipsoid, a uniform magnetization generates a uniform demagnetizing field (it is the only real shape for which it is rigorously true [2]).

We can therefore calculate the demagnetizing field at the center of the sphere, and we set the axis of magnetization along the z direction.

We have no free current, hence the curl of the magnetic field is zero, and we can therefore define a scalar potential which verifies:

$$\vec{H} = -\vec{\nabla}\Phi \tag{2.23}$$

which will in turn verify

$$\nabla^2\Phi = 0 \tag{2.24}$$

whose solution is

$$\Phi = -\frac{1}{4\pi}\iiint\frac{\vec{\nabla}'\bullet\vec{M}}{|\vec{r}-\vec{r}'|}d^3\vec{r}' + \frac{1}{4\pi}\iint\frac{\vec{M}\bullet\vec{n}}{|\vec{r}-\vec{r}'|}d^2S \tag{2.25}$$

It is equivalent to a potential created by volume 'charges' $\vec{\nabla}'\bullet\vec{M}$ and surface 'charges' $\vec{M}\bullet\vec{n}$.

Inside our sphere $\vec{\nabla}'\bullet\vec{M} = 0$ and therefore

$$\vec{H} = \frac{1}{4\pi}\iint\frac{\vec{M}\bullet\vec{n}}{|\vec{r}-\vec{r}'|^3}(\vec{r}-\vec{r}')d^2S \tag{2.26}$$

The detailed calculation is given in Appendix C. The result is:

$$\boxed{\vec{H} = -\frac{M_0}{3}\vec{e}_z} \tag{2.27}$$

Thus, for a **uniformly magnetized sphere, the demagnetizing factor along any axis is equal to 1/3**.

2.1.3.3 Demagnetizing factors inside a uniformly magnetized ellipsoid.

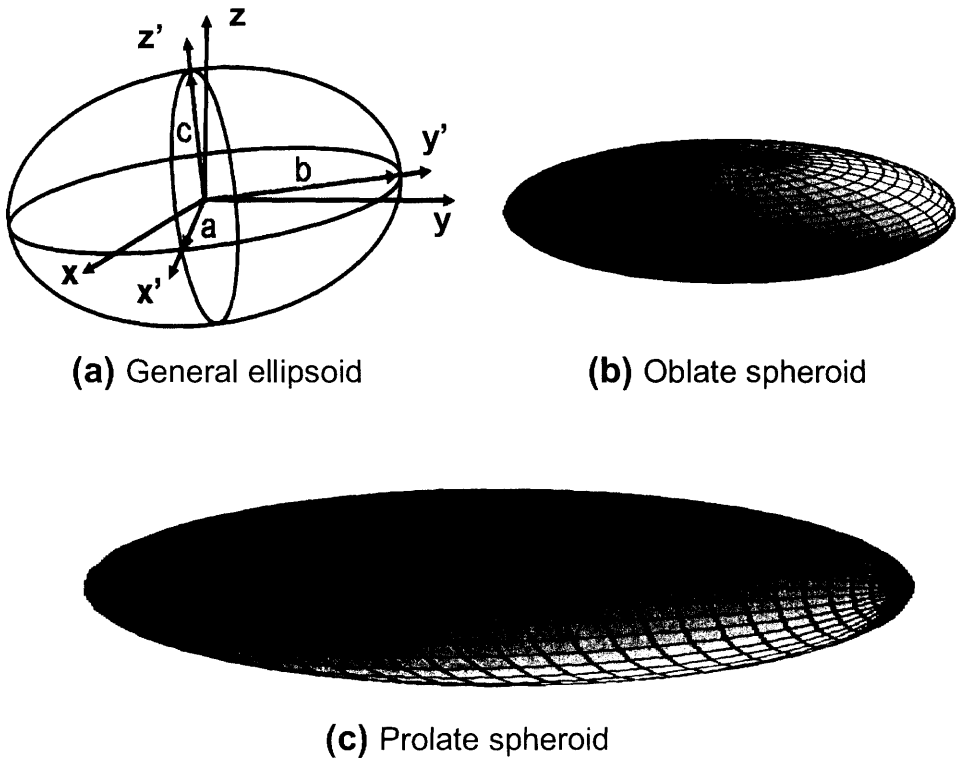

Figure 2.1 Ellipsoids

For a **prolate spheroid** [3] (Fig. 2.1.c), $a = b < c$, with $m = \frac{c}{a}$

$$N_c = \frac{1}{m^2 - 1}\left[\frac{m}{2\sqrt{m^2 - 1}} \ln\left(\frac{m + \sqrt{m^2 - 1}}{m - \sqrt{m^2 - 1}}\right) - 1\right] \tag{2.28}$$

$$N_a = N_b = \frac{1 - N_c}{2} \tag{2.29}$$

When $m >> 1$,

$$N_c = \frac{\ln(2m) - 1}{m^2} \tag{2.30}$$

$$N_a = N_b = \frac{1}{2}\left(1 - \frac{\ln(2m) - 1}{m^2}\right) \tag{2.31}$$

As m goes to infinity, $N_a = N_b \to \frac{1}{2}$ and $N_c \to 0$, which shows that **along the long axis, the demagnetizing field is the smallest**.

For an **oblate spheroid** [3] (Fig 2.1.b), $a < b = c$, with $m = \frac{c}{a}$

$$N_a = \frac{m^2}{m^2-1}\left[1 - \frac{1}{\sqrt{m^2-1}}\arcsin\left(\frac{\sqrt{m^2-1}}{m}\right)\right] \tag{2.32}$$

$$N_b = N_c = \frac{1-N_a}{2} \tag{2.33}$$

When $m >> 1$,

$$N_a = 1 - \frac{\pi}{2m} \to 1 \tag{2.34}$$

$$N_b = N_c = \frac{\pi}{4m} \to 0 \tag{2.35}$$

Hence, in the "**flat plane" the demagnetizing field is the lowest**, whereas it is very high along the out of plane direction.

2.1.3.4 Magnetostatic energy.

It is the energy of a magnetized sample in its own demagnetizing field.
The magnetostatic or stray field energy density is the opposite of the work done to bring the magnetization from zero to its actual value.

$$\boxed{e_{magnetostatic} = -w = -\mu_0 \int_0^{\vec{M}} \vec{H}_{demag}(\vec{M}) \bullet d\vec{M}} \tag{2.36}$$

If the demagnetizing field is uniform as in a uniformly magnetized ellipsoid (2.21), then

$$e_{magnetostatic} = \mu_0 \int_0^{(M_1,M_2,M_3)} \left(N_1 M_1 dM_1 + N_2 M_2 dM_2 + N_3 M_3 dM_3\right)$$

$$\boxed{e_{magnetostatic} = \frac{\mu_0}{2}\sum_i N_i M_i^2} \tag{2.37}$$

The magnetostaic energy can be interpreted as the dipole energy of the magnetized sample [4]. It is the **energy needed to assemble the atomic dipoles that constitute the solid**. If $d\vec{\mu} = \vec{M}dV$ is the dipole moment, its potential energy in the demagnetizing field is

$$dU = -\mu_0 d\vec{\mu} \bullet \vec{H}_{demag} = -\mu_0 \vec{M} \bullet \vec{H}_{demag} dV$$

Since the dipole pair interactions must be counted only once [5], the resulting energy of the sample is simply:

$$E_{magnetostatic} = -\frac{\mu_0}{2}\int_{sample} \vec{H}_{demag}(\vec{r}) \bullet \vec{M}(\vec{r}) dV \tag{2.38}$$

This contribution to the energy is **positive**, as can be seen after transforming that expression (the derivation from 2.38 to 2.39 is detailed in Appendix B) :

$$E_{magnetostatic} = \frac{\mu_0}{2}\int_{space} H^2_{demag}(\vec{r}) dV \tag{2.39}$$

2.1.4 Shape anisotropy.

To minimize its magnetostatic energy, a sample will prefer **a magnetization along the smallest demagnetizing principal direction** (with the smallest demagnetizing eigenvalue): for the prolate spheroid, the magnetization will prefer to align along the c axis where the demagnetizing factor goes to 0 as c goes to infinity. In the oblate spheroid, the magnetization will preferably be in the bc plane, showing that usually in thin films, the magnetization is in plane, and in thin patterned films, the magnetization is in plane and along the long axis of the pattern (e.g. in a wire, along the length of the wire).

2.1.5 Crystal anisotropy.

2.1.5.1 Spin-orbit coupling and crystal anisotropy.

This type of anisotropy is due to **spin-orbit coupling**, ie the interaction of the orbital electron motion with its spin. A classical hydrogen atom model can enable us to understand the origin of that coupling. The atom is modeled as an electron with velocity $\vec{v}$ around a proton which is much heavier and thus considered fixed in our frame of reference.
In the referential frame of the electron, the proton move at velocity $-\vec{v}$, thus creating a magnetic field (Biot and Savart)

$$\vec{B} = \frac{\mu_0 q \cdot \vec{r} \times \vec{v}}{4\pi \cdot r^3} = \frac{\mu_0 q \cdot \vec{L}}{4\pi \cdot m_e r^3} \tag{2.40}$$

where $\vec{L}$ is the orbital momentum of the electron in our referential. The spin of the electron relates with a good approximation to its magnetic moment by:

$$\hat{\mu}_s = -\frac{q}{m_e}\hat{S} \tag{2.41}$$

We therefore have a magnetic potential energy of the spin in the magnetic field created by the proton, which can be expressed in the lab referential:

$$U = -\vec{\mu}_s \bullet \vec{B} = \frac{\mu_0 q^2}{8\pi \cdot m_e^2 r^3} \vec{S} \bullet \vec{L} \qquad (2.42)$$

where a ½ factor has been introduced due to the change of referential [6]

The spin orbit coupling just explained here in the case of hydrogen is responsible for many effects such as magnetocrystalline anisotropy, magnetostriction, magneto-optic effects (Kerr, Faraday), anisotropic magnetoresistance, ferromagnetic Hall effect and magnetic resonance damping.

The crystal structure shapes the orbital envelope of the outer shell electrons of each atom due to the field created by the neighboring atoms (**crystalline field**) which has the symmetry of the crystal. That **lattice-orbital coupling** is very strong and it is very difficult to change the orbital of the undisturbed crystal. Thus if spin and orbit are slightly coupled, spin and lattice will be too, generating thus preferable directions along which the spin aligns.

This coupling is usually **weak**. In the bulk crystal, since the wave functions of the electron are no longer rotation invariant due to the crystalline electric field, and as a result the angular momentum is very small compared to the spin moment. L is said to be quenched.

2.1.5.2 Polycrystalline crystals.

If the grains of the polycrystal are randomly oriented, then its magnetocrystalline anisotropy will be on average zero. If they have a favored orientation, the polycrystal is said to have a texture, and, to some extent, the magnetocrystalline anisotropy will set the easy axis.

2.1.6 Surface anisotropy.

Néel [7] first introduced the concept and a theory of surface magnetic anisotropy often referred to as the Néel surface anisotropy. At the surface of the crystal, the symmetry of the bulk crystal is **broken** and the **symmetry** is lowered. The band structure of the 3d electrons at the surface changes, and the modified spin-orbit interaction (the orbital momentum is no longer quenched) causes that surface magnetic anisotropy and gives rise to a preferred surface magnetization direction with respect to the surface plane [8,9]. It must be stated here that it is a different effect from the shape anisotropy.

In thin films, Gradmann et al. [10] confirmed the existence of that surface anisotropy in $Fe_{52}Ni_{48}$ films of varied thicknesses d. The total uniaxial magnetic anisotropy energy was

$$E = K_{tot}(d)\cos^2(\theta) \qquad (2.43)$$

where θ is the angle between the magnetization and the normal to the film plane, and $K_{tot}(d) = K_{bulk} + \frac{2K_s}{d}$, where K_{bulk} accounts for both the magnetocrystalline bulk anisotropy

and the shape anisotropy. This first suggested that one could grow a thin film with an out of plane easy axis or perpendicular anisotropy, provided that K_s is negative and the thickness small enough. (Au/Co/Au, Pt/Co/Pt and Pd/Co/Pd multilayers are examples). However, magnetoelastic and Néel-type anisotropy are closely intertwined in thin films and cannot be clearly separated and one can only consider an effective K_s [11].

2.1.7 Magnetoelastic anisotropy.

Also called stress anisotropy, it is another consequence of the spin-orbit coupling. When magnetized, a formerly demagnetized crystal will display a strain. This effect is called magnetostriction, and is due to spin-orbit coupling. Reciprocally, applying a uniaxial stress on the crystal will create a uniaxial anisotropy, called stress or magnetoelastic anisotropy, whose energy has the form $E = K\sin^2(\theta)$. (e.g. strained Cu/Ni/Cu can have a perpendicular anisotropy)

That energy and all the energies for the anisotropies aforementioned need to be considered together in order to determine the resulting easy axis.

2.1.8 Exchange anisotropy.

This is a very specific type of anisotropy that arises when an antiferromagnetic material is coupled with a ferromagnetic one as shown in Fig. (2.2)

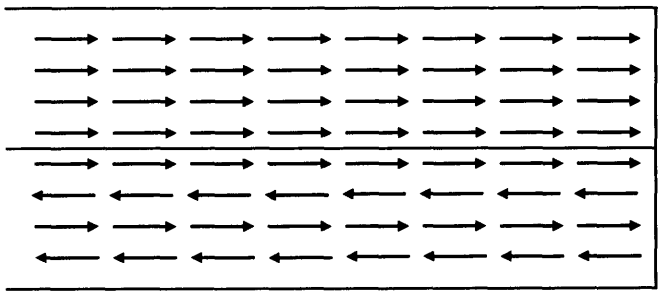

Figure 2.2 Ferromagnetic film on top of an antiferromagnetic film.

At the interface, the exchange coupling described in 2.1.2 will set a preferred orientation of the ferromagnetic magnetization. Supposing the antiferromagnetic film in Fig (2.2) has a very strong anisotropy, to reverse the ferromagnetic layer will require a larger field than when the aniferromagnetic layer is removed, hence shifting the M-H curve.

2.1.9 Energetics of a ferromagnet and its domain structure.

A ferromagnetic sample placed in an external field $\vec{H}_{applied}$ has a total energy:

$$E_{tot} = E_{exchange} + E_{anisotrpy} + E_{Zeeman} + E_{magnetostatic} \tag{2.44}$$

where $E_{exchange}$ is given by (2.4), $E_{anisotropy}$ by the sum of all anisotropy energy term (but the shape anisotropy) that apply (e.g. in a polycrystalline ultra-thin film, (2.43) would be of importance) and $E_{magnetostatic}$ by (2.36).

$$E_{Zeeman} = -\mu_0 \int \vec{H}_{applied} \bullet \vec{M}(\vec{r}) dV \tag{2.45}$$

The Zeeman energy is the energy that results from the external applied field with the magnetization of the sample. It favors a magnetization aligned with the applied field.

In order to minimize its total energy, a ferromagnetic sample can organize its magnetic structure into domains which are space regions in which the magnetization direction is constant. The mathematical surface that separates two domains is called a domain wall.

To minimize its total energy, the material needs to reduce its magnetostatic energy while increasing the sum of the other terms by a smaller amount. (2.39) indicates that to reduce the magnetostatic energy, one only needs to reduce the demagnetizing field over the whole space. That can be done by creating domains as seen in Fig(2.3) in which the anisotropy is assumed to be along the long axis. (2.39) will be reduced from Fig(2.3.a) to Fig(2.3.b): This phenomenon, usually referred to as **flux closure**, enables the sample to reduce its magnetostatic energy.

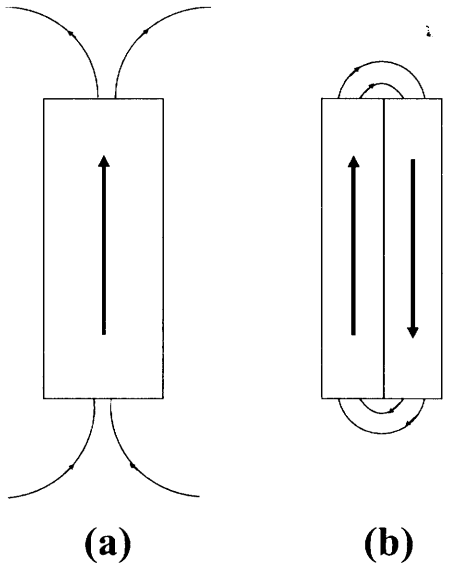

Figure 2.3 Domains and flux closure.

It is theoretically possible to completely eliminate that stray field, leading to a zero magnetostatic energy. In all the domains, the magnetization is constant and the first term of (2.25) is 0. To cancel the second term, one must consider the surface that surrounds a domain, that is the domain wall (to some extent, the surface of the sample itself is an unmoving domain wall). For each domain wall,

$$\vec{M}_{DW} = \vec{M}_1 - \vec{M}_2 \tag{2.46}$$

where the subscript 1 and 2 refer to the domains 1 and 2 separated by the domain wall (DW).

Therefore, a domain structure will generate a zero magnetostatic energy if all the domain walls have a normal orthogonal to their magnetization, i.e. if any **domain wall bisects the directions of the magnetizations of the two adjacent domains**. This can happen in a ferromagnetic sample having very low anisotropy and magnetostriction. Fig (2.4) shows the AFM (2.4.a) and MFM (2.4.b) picture of a thin polycrystalline permalloy (10 nm) 5 microns square pad. The domain structure is quite apparent and follows the trend seen in Fig. 2.4.c with almost zero magnetostatic energy (complete flux closure within the sample).

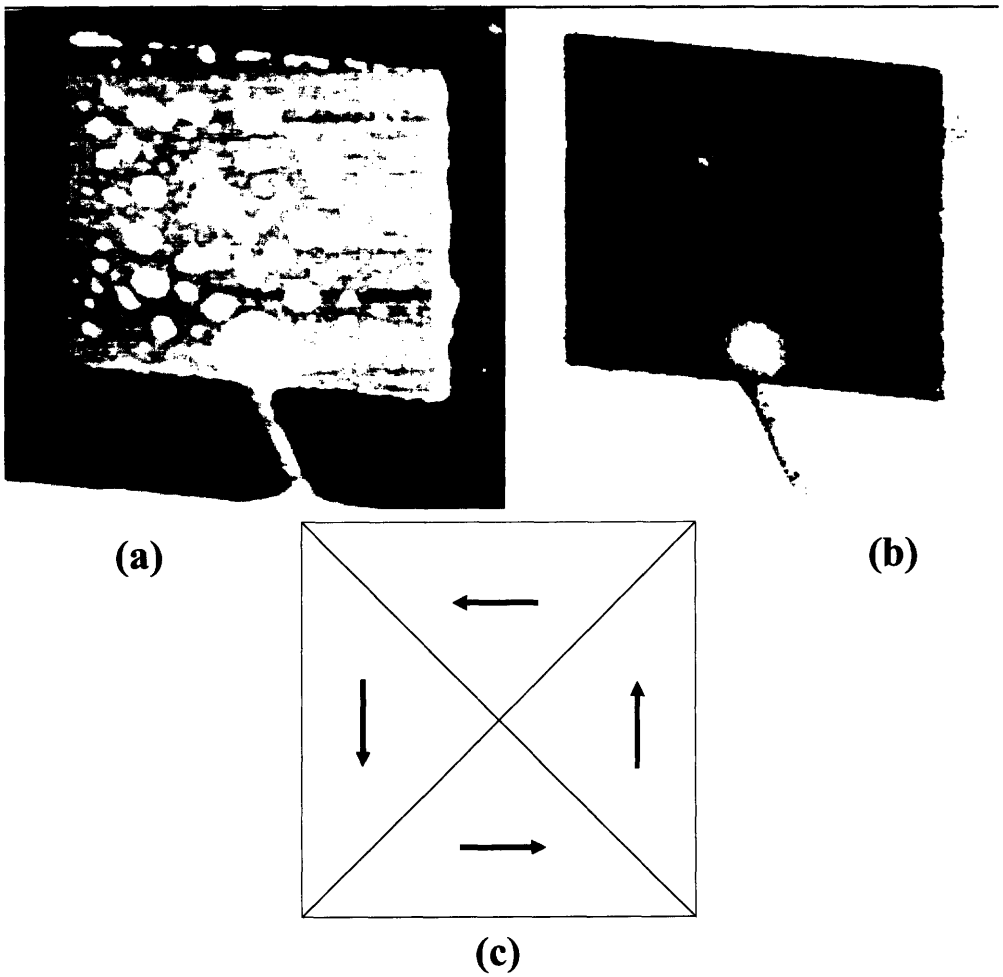

Figure 2.4 Flux closure in a square pad. [Work done by the author at CNRS-Orsay with J. Miltat and A. Thiaville]

But creating a domain structure requires energy. The anisotropy energy and the exchange energy are always increasing when a domain structure is formed. Inside the domains, the anisotropy energy can increase if the magnetization is away from the easy-axis. At the transition between two domains, ie at the domain wall, both the anisotropy energy term and the exchange energy term will locally give a positive contribution. If the magnetization switches within one interatomic distance from one easy direction to another one, the anisotropy energy is zero, but the exchange coupling term is maximum. Since the exchange coupling is typically a much stronger effect than anisotropy, this type of abrupt domain wall does not arise. The magnetization will continuously reverse from one domain to the next, generating a so called **domain wall width and structure** so as to minimize the sum of exchange and anisotropy contributions and, in the case of thin films, the magnetostatic energy contribution. Two types of domain walls as seen in Fig(2.5) arise in thin films (with in-plane magnetization) depending on the film thickness.

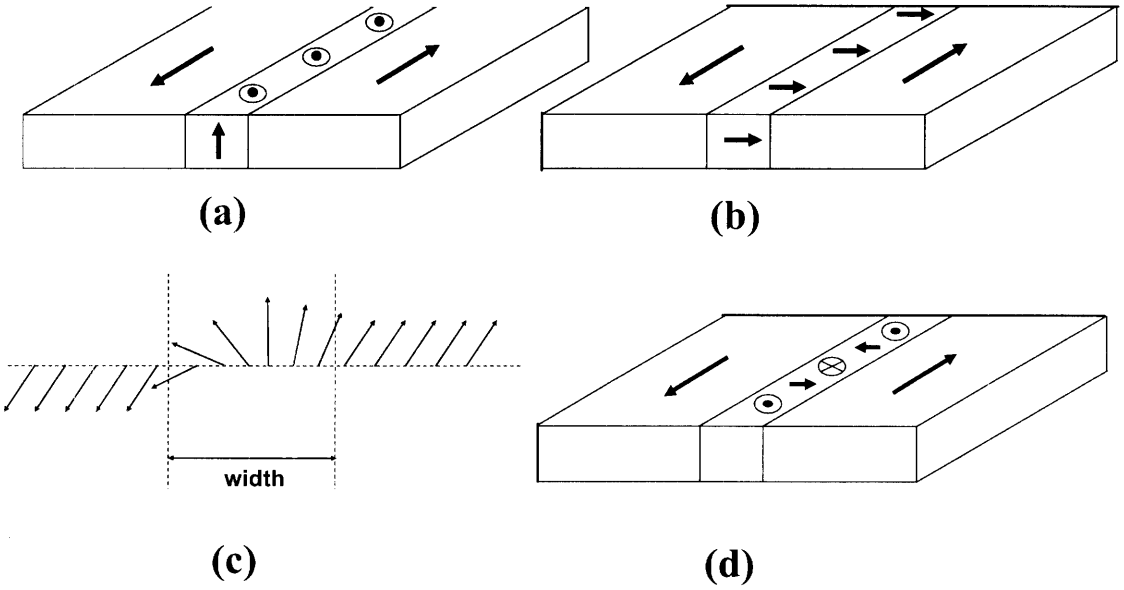

Figure 2.5 (a) 180° Bloch domain wall versus (b) 180° Néel domain wall. (c) Continuous magnetization transition in a 180° Bloch domain wall. (d) describes the cross-tie domain wall structure.

The Néel wall is the stable structure below a certain critical thickness. The transition is due to the magnetostatic energy. If the film is very thin, the spins in Fig (2.5.a) in the domain wall region will have a larger magnetostatic energy than those in Fig (2.5.b). Therefore in thin films the domain wall structure and width will be determined by the minimization of the three energy terms: exchange, anisotropy and magnetostatic. Another type of domain wall structure called the cross-tie wall Fig(2.5.d) [12] can arise for some thicknesses between the thick film Bloch domain wall and the very thin film Néel wall.

The exchange coupling intensity introduces a very common way to classify ferromagnetic materials. A ferromagnet with weak exchange coupling is called a **soft** ferromagnetic material whereas one with strong exchange coupling is called a **hard**

ferromagnetic material. Creating a domain wall will therefore be a much less costly process in soft ferromagnets. A thick sample of soft ferromagnetic material will therefore show no macroscopic magnetization in the absence of an applied field. Refrigerator permanent magnets are made of hard ferromagnetic material (actually usually hard ferrimagnetic material), but the only way another material can be attracted by this magnet is if that material is itself magnetic. The door of the fridge contains a thick sheet of soft magnetic steel, whose domains will align under the influence of the stray field from the hard magnet, thus allowing for the attraction, but will relax to a flux closure configuration when the hard magnet is removed.

However, if the dimensions of the ferromagnetic (soft or hard) sample are decreased enough, the exchange energy dominates over the other terms and shape anisotropy will impose the easy axis, leading to a **single domain state**. It is defined [11] by a state displaying no domain wall nor vortex and whose magnetization is on average uniform as seen in Fig(2.6).

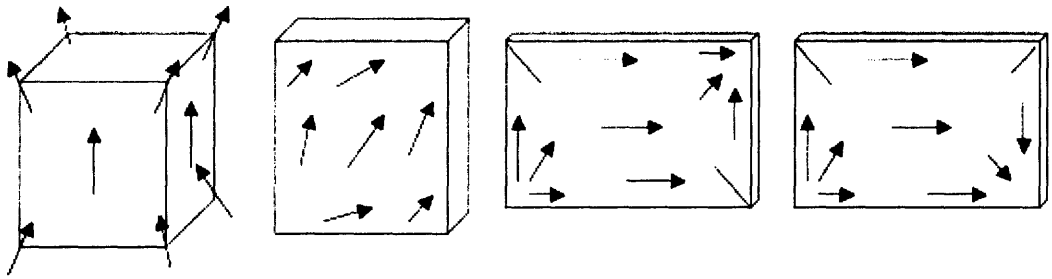

Figure 2.6 The most common single domain states. From left to right: flower, leaf, S and C states. After Ref. [11].

These structures display a non uniform magnetization, which may result in higher switching fields than in the macrospin states described next, and non-coherent reversal processes [13].

In particles of extremely small size of ellipsoid shape, the magnetization can be uniform throughout the sample without any applied field. Such particles are called **macrospins** and reverse by **coherent rotations** of all the magnetic moments.

In thin stripes, the shape anisotropy is predominant. The magnetization will therefore lie along the length of the stripe, thus leading to only two possible domain configurations. The 180° Néel domain wall structure will depend on the cross-section [14]: so-called **transverse** domain walls Fig(2.7.a-b) will be more stable in small cross-section magnetic stripes, whereas **vortex** domain walls Fig(2.7.c-d) will be more stable in larger cross-section magnetic stripes. It should be noted however that those two configurations can be observed in a same magnetic stripe. One of them is metastable, but still in a local energy minimum.

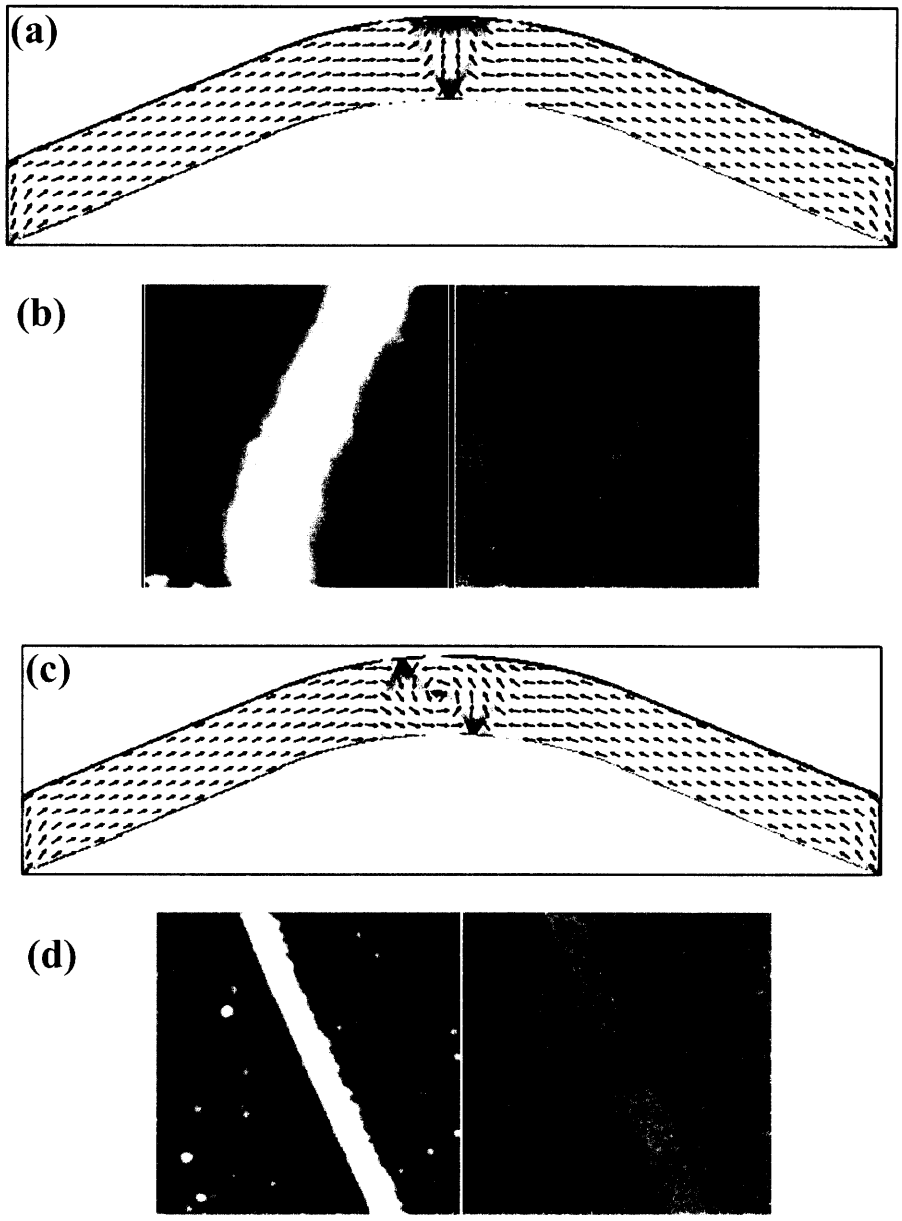

Figure 2.7 (a) OOMMF simulation of a transverse wall in a permalloy wire of 300 nm width and 10 nm thickness. (b) AFM and MFM imaging of a wire of same dimensions displaying a transverse wall. (c) OOMMF simulation of a vortex wall in a permalloy wire of 300 nm width and 20 nm thickness. (d) AFM and MFM imaging of a wire of same dimensions displaying a vortex wall. [Work done by the author at CNRS-Orsay with J. Miltat and A. Thiaville]

2.2 Interactions between current and local magnetization.

2.2.1 Band structure of transition metals.

First, it is well known that when atoms are brought together to form a solid, due to atomic orbital overlapping, the atomic states split and eventually broaden into bands whose energies can overlap with neighboring bands as seen in Fig (2.8).

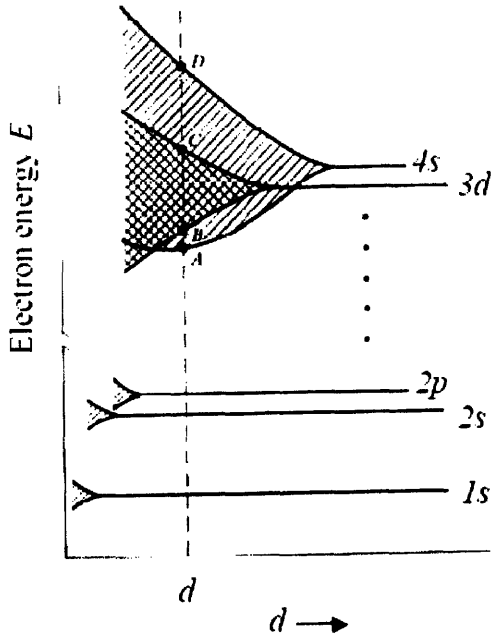

Figure 2.8 Band structure formation in a transition metal crystal as a function of the interatomic distance d. After Ref. [15].

The electrons that belong to the highest energy levels in the atomic orbitals are the first to overlap when the atoms are brought together since they belong to the outer shells. The **4s electron band** has wave functions with high presence probability between the atoms, acting there very much like plane waves, and the electrons in this band have very **low effective mass** and act as free electrons, with a very high electrical conductivity and responsible for the main part of the crystal cohesion. The **3d electron band** is **narrower in energy** because the 3d electrons are closer to the nucleus and overlap less, but with a much **higher density** since the atomic 3d level can contain 10 electrons compared to only two at the 4s level. These 3d electrons are the ones responsible for ferromagnetic properties of some transition metals. The positive exchange integral due to the Pauli

exclusion principle will generate a shift between the spin up and spin down parts of the 3d band relative to each other as seen in Fig(2.9) [16,17].

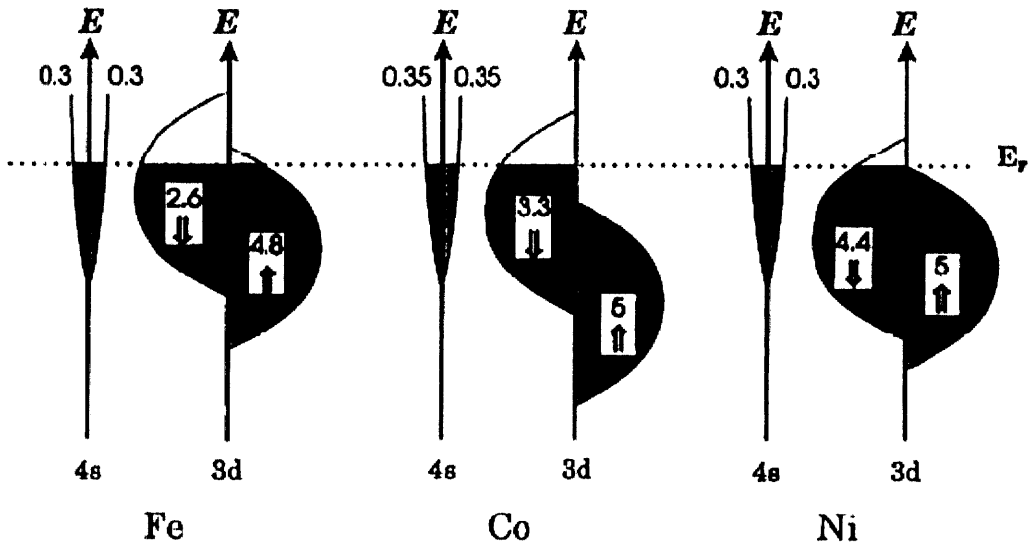

Figure 2.9 Simplified density of states of 4s and 3d bands of Fe, Co and Ni. The numbers of spin-up (right) and spin-down (left) are shown in each band. After Ref. [18].

When adding a pair of electrons to an unfilled band, the parallel spin configuration is favored if the exchange coupling gain overcomes the surplus energy required to place the second electron in a higher energy state since the Pauli exclusion principle forbids two same spin electrons to occupy an identical energy level. In the 3d band of some transition metals such as Fe, Co or Ni, this condition is fulfilled because first the exchange integral is positive and second the band is very narrow, hence the energy density is high and the levels very close in energy. In the 4s band, the band is very broad and the density low, thus the levels inside are more widely spaced, making it energetically unfavorable for the spins to align. The 3d band that displays this shifting must of course be only partly filled, otherwise the population of spin-up equals that of spin-down, generating no net magnetic moment. Fe Co and Ni meet all the requirements, namely **unfilled 3d band, very narrow 3d band and positive exchange integral for the 3d electrons**. Their magnetic moment per atom can be inferred from Fig(2.9) as the difference between the numbers of spin-up to the numbers of spin-down times the Bohr magneton: $2.2\mu_B$ for Fe, $1.7\mu_B$ for Co and $0.6\mu_B$ for Ni with $\mu_B = \frac{e\hbar}{2m} = 0.927 A.m^2$.

2.2.2 Introduction to electronic transport in magnetic materials.

2.2.2.1 Resistivity of ferromagnets.

The electrical transport in transition metals is mainly operated by the 4s band 'free' electrons and the magnetic moment is carried by the 3d band electrons. However, the overlapping the 4s and 3d states at the Fermi energy level leads to **hybridization** of these states which is responsible for many different effects of magnetism on electrical transport in such metals. For instance it reduces the mobility of the electrical conduction 4s states through increasing their effective mass and allowing their scattering into more localized but very dense 3d states, thus leading to higher resistivities than noble metals (Fermi energy above the 3d band, only in the 4s band, no hybridization phenomenon e.g. Cu).

At low temperatures, the charge carriers retain their spin orientation during most scattering events. The spin-up and spin-down charge carriers can thus be seen as conducting along two parallel paths of resistivities respectively $\rho^{\uparrow}$ and $\rho^{\downarrow}$. Each of these resistivities is the sum of different scattering processes (phonon, impurities, s-d). As seen in Fig(2.9), the state density is different between the spin-up and spin-down states at the Fermi level: in the three metals, the spin-up state density is lower than the spin-down one, and therefore the s-d scattering will be higher in the spin-down channel. Therefore the resistivity of the spin-up channel will be the lowest one. The total resistivity is:

$$\rho = \frac{\rho^{\uparrow}\rho^{\downarrow}}{\rho^{\uparrow} + \rho^{\downarrow}} \tag{2.47}$$

The total resistivity described by that **two current model** [19] is going to be lower than the lowest of the resistivities, namely $\rho^{\uparrow}$. This simple model explains why the ferromagnetic transition metals have lower resistivities than non-ferromagnetic transition metals.

2.2.2.2 Anisotropic Magnetoresistance (AMR).

In the presence of a magnetic field, in any material, because the Lorentz force deflects charge carriers from the current direction, the resistivity increases. This effect is called magnetoresistance and follows Kohler's rule:

$$\frac{\Delta\rho}{\rho} \propto \left(\frac{H}{\rho}\right)^2 \tag{2.48}$$

In a ferromagnet, the magnetization adds a spontaneous contribution that depends on its direction. It is referred to as the anisotropic magnetoresistance (AMR). Kohler's rule can be generalized for a ferromagnet:

$$\frac{\Delta\rho}{\rho} \propto a\left(\frac{H}{\rho}\right)^2 + b\left(\frac{M}{\rho}\right)^2 \tag{2.49}$$

where the first term describes the ordinary magnetoresistance and the second the spontaneous or anisotropic magnetoresistance.

However, the simple Lorentz force cannot account for a lower resistivity when the magnetization and the current density are orthogonal rather than parallel, i.e. for the negative sign of b in (2.49). The origin of AMR lies in fact in the **spin-orbit** coupling: the direction of the magnetization changes the shape of the orbitals, thus leading to a magnetization direction dependence of the scattering.

The operator in the spin orbit coupling is

$$\hat{\vec{L}} \bullet \hat{\vec{S}} = \hat{L}_x\hat{S}_x + \hat{L}_y\hat{S}_y + \hat{L}_z\hat{S}_z = \hat{L}_z\hat{S}_z + \frac{1}{2}\left(\hat{L}^+\hat{S}^- + \hat{L}^-\hat{S}^+\right) \tag{2.50}$$

where $\hat{A}^{\pm} = A_x \pm iA_y$. The effect of such an operator is to raise by one or decrease by one the associated quantum number of the eigenfunctions. More specifically,

$$\left(\hat{L}^+\hat{S}^- + \hat{L}^-\hat{S}^+\right)\left|\Psi(n,l,m,s=+\frac{1}{2}\right\rangle = \left|\Psi(n,l,m+1,s=-\frac{1}{2}\right\rangle \text{ with } m+1 \le l$$

$$\left(\hat{L}^+\hat{S}^- + \hat{L}^-\hat{S}^+\right)\left|\Psi(n,l,m,s=-\frac{1}{2}\right\rangle = \left|\Psi(n,l,m-1,s=+\frac{1}{2}\right\rangle \text{ with } m-1 \ge -l$$

Therefore $\hat{\vec{L}} \bullet \hat{\vec{S}}$ allows for the **mixing up the spin-up and spin-down channels**. But when the current is perpendicular to the magnetization, the conduction electron momentum is not likely to be in the plane of the classical orbit of the empty 3d states (ie J is most likely parallel to L) whereas when the current is parallel to the magnetization, it is. In the latter case, the spin orbit coupling will generate more **s-d scattering**, whereas in the former, it will not. The total resistivity will therefore depend on the orientation of the magnetization with respect to the current.

An approximate expression of the resistivity is:

$$\rho = \rho_0 + \rho_{AMR}\cos^2(\theta) \tag{2.51}$$

where θ is the angle between the magnetization and the current density.

Fig.(2.10) shows the relative resistance changes of several ferromagnetic materials when an external field is applied parallel or perpendicular to the current direction. The resistivity of parallel magnetization and current is in all six films higher than the perpendicular one (saturation values). The jumps correspond to the magnetization reversal effect of the film on the resistance: when the reversal process occurs, domains appear as well as domain walls, and the consequence is that the magnetization is no more completely parallel or completely perpendicular to the current, thus leading respectively to a decrease or an increase in the film resistance. The loops are even functions of the field, as inferred by Kohler's rule.

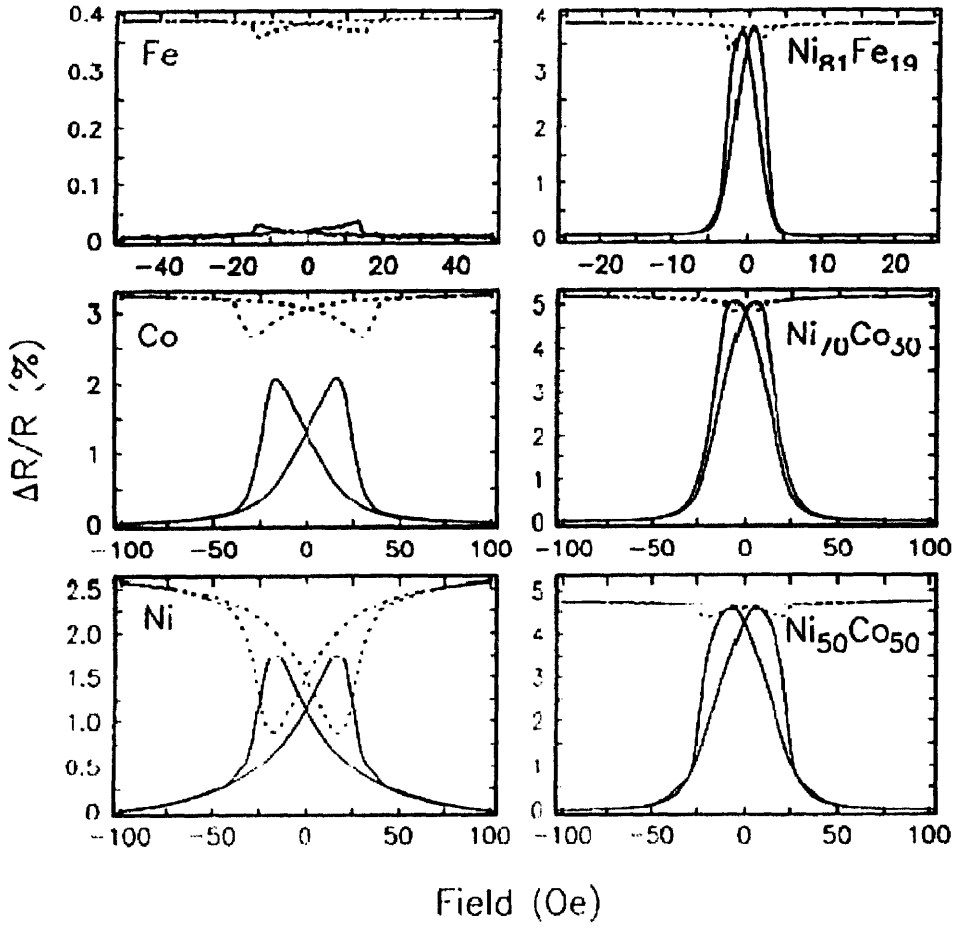

Figure 2.10 Anisotropic magnetoresistance effects in 1μm thick sputtered films of Fe, Co, Ni, $Ni_{81}Fe_{19}$, $Ni_{70}Co_{30}$, $Ni_{50}Co_{50}$. The magnetic field is applied either parallel to the current (dotted lines) or perpendicular to it (full lines). After Ref. [20].

The AMR effect had been used in magnetic recording read heads for hard disk drives since the early 1990s, but they have been replaced by GMR devices which have higher sensing signals.

2.2.2.3 Giant Magnetoresistance (GMR).

GMR was discovered in 1988 by Baibich et al. who reported a 50% magnetoresistance (MR) ratio at 4.2K in Fe/Cr multilayers [21]. The effect has been observed since then on a variety of multilayered structures always involving magnetic layers separated by non magnetic layers (spacer layers). The resistance of these multilayer structures varies with the angle of magnetization between one magnetic layer and the next as a cosine:

$$R(\theta) = R_{\uparrow\uparrow} + \left(R_{\uparrow\downarrow} - R_{\uparrow\uparrow}\right)\left(\frac{1-\cos(\theta)}{2}\right) \tag{2.52}$$

The mechanism of GMR can be understood thanks to the two current model of Mott introduced in 2.2.2.1. at low temperatures. The thicknesses of the layers are less than the

mean free path of the electron in each layer, allowing for this model to be valid. Let us consider the stack of a so called **Pseudo Spin Valve** (PSV), namely two ferromagnetic layers separated by a non magnetic layer (spacer) as described in Fig(2.11).

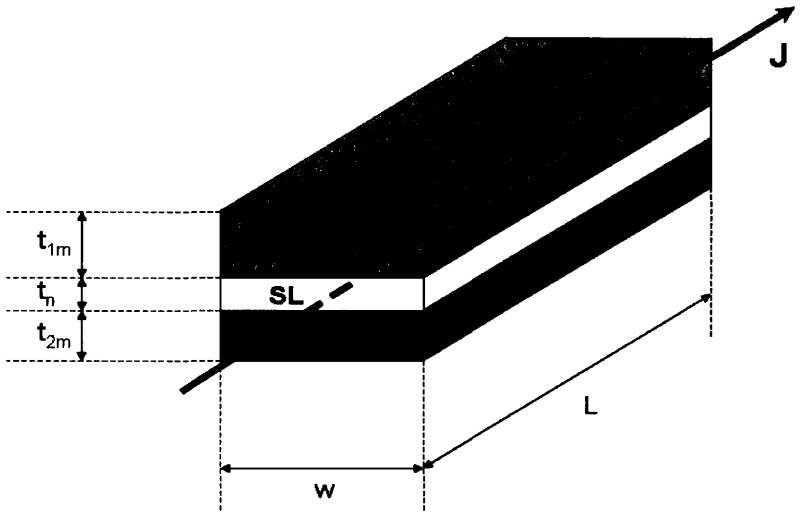

Figure 2.11 Pseudo Spin Valve (PSV) multilayer structure. Two ferromagnetic layers FL1 and FL2 are separated by a non magnetic spacer layer (SL).

In the configuration described in Fig (2.11), the magnetization of the ferromagnetic layers have directions along the long axis of the bar L due to shape anisotropy. We assume each forms a single domain as described in 2.1.9.

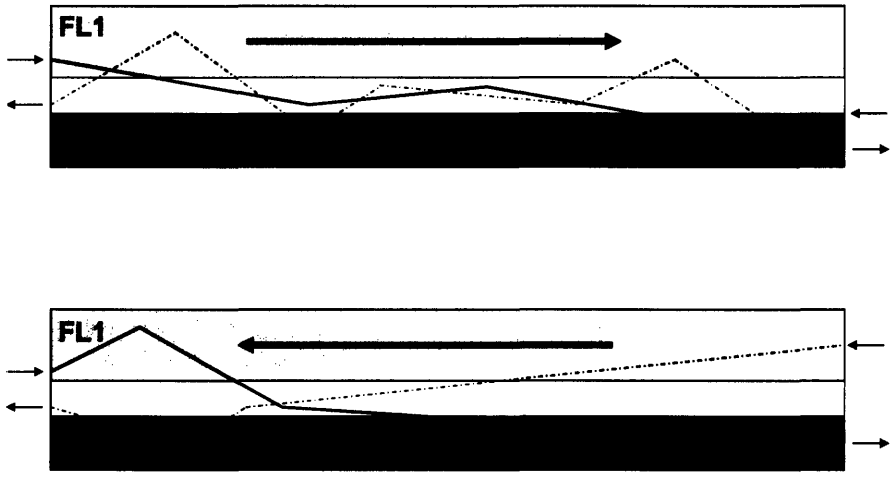

Figure 2.12 Pseudo Spin Valve (PSV) multilayer structure in the parallel configuration (top) and antiparralel (bottom). Spin-up and spin-down scattering are schematically pictured.

As seen in Fig(2.12), the spin-up channel electron will scatter much less in the parallel configuration than in the antiparallel, whereas it is just the opposite for the spin-down electrons. The total resistance in the parallel and antiparallel configurations are:

$$R_{\uparrow\uparrow} = \left(\frac{1}{\frac{\rho_n L}{wt_n} + \frac{\rho_{m1}^{\uparrow} L}{wt_{m1}} + \frac{\rho_{m2}^{\uparrow} L}{wt_{m2}}} + \frac{1}{\frac{\rho_n L}{wt_n} + \frac{\rho_{m1}^{\downarrow} L}{wt_{m1}} + \frac{\rho_{m2}^{\downarrow} L}{wt_{m2}}} \right)^{-1} \tag{2.53}$$

$$R_{\uparrow\downarrow} = \left(\frac{1}{\frac{\rho_n L}{wt_n} + \frac{\rho_{m1}^{\downarrow} L}{wt_{m1}} + \frac{\rho_{m2}^{\uparrow} L}{wt_{m2}}} + \frac{1}{\frac{\rho_n L}{wt_n} + \frac{\rho_{m1}^{\uparrow} L}{wt_{m1}} + \frac{\rho_{m2}^{\downarrow} L}{wt_{m2}}} \right)^{-1} \tag{2.54}$$

If we take the respective spin-up and spin-down resistivities to be identical in both ferromagnetic layers ($\rho_{m1}^{\uparrow} = \rho_{m2}^{\uparrow}$ and $\rho_{m1}^{\downarrow} = \rho_{m2}^{\downarrow}$, we can simplify (2.53) and (2.54):

$$R_{\uparrow\uparrow} = \frac{\rho_n L}{wt_n} \frac{1 + (\alpha + \beta)(r_1 + r_2) + \alpha\beta(r_1 + r_2)^2}{2 + (\alpha + \beta)(r_1 + r_2)} \tag{2.55}$$

$$R_{\uparrow\downarrow} = \frac{\rho_n L}{wt_n} \frac{1 + (\alpha + \beta)(r_1 + r_2) + \alpha\beta(r_1^2 + r_2^2) + (\alpha^2 + \beta^2) r_1 r_2}{2 + (\alpha + \beta)(r_1 + r_2)} \tag{2.56}$$

where $\alpha = \frac{\rho^{\uparrow}}{\rho_n}$ and $\beta = \frac{\rho^{\downarrow}}{\rho_n}$, $r_1 = \frac{t_{m1}}{t_n}$ and $r_2 = \frac{t_{m2}}{t_n}$

and therefore,

$$\boxed{R_{\uparrow\downarrow} - R_{\uparrow\uparrow} = \frac{\rho_n L}{wt_n} \frac{(\alpha - \beta)^2 r_1 r_2}{2 + (\alpha + \beta)(r_1 + r_2)}} \tag{2.57}$$

(2.57) shows very clearly that without a different resistivity in each channel, there can be no GMR effect. It shows also that as the spacer thickness increases, the GMR effect diminishes.

GMR will therefore arise if the relative orientation of the magnetizations of the adjacent magnetic layers can be modified and if the thicknesses of each layer are less than the mean free path of the electron.

2.2.3 Effect of the current on the local magnetization in a ferromagnet.

2.2.3.1 Introduction on micromagnetics in the Dynamic Regime.

In quantum mechanics, for a free electron spin, the Ehrenfest theorem reads:

$$i\hbar\frac{d}{dt}\left\langle\hat{\vec{S}}\right\rangle(t)=\left\langle\left[\hat{\vec{S}},\hat{H}(t)\right]\right\rangle \tag{2.58}$$

With only an time-dependent external field acting on the electron,

$$\hat{H}(t)=\frac{g\mu_B}{\hbar}\hat{\vec{S}}\bullet\vec{B} \tag{2.59}$$

where g is the gyromagnetic splitting factor and $\mu_B=\frac{e\hbar}{2m_e}$

This is easily simplified to [22]

$$\frac{d}{dt}\left\langle\hat{\vec{S}}\right\rangle(t)=-\frac{g\mu_B}{\hbar}\left(\left\langle\hat{\vec{S}}\right\rangle(t)\times\vec{B}(t)\right) \tag{2.60}$$

(2.63) describes the **Larmor precession** for a free electron spin.
The exact expression for 2.41 is:

$$\hat{\vec{\mu}}_s=-\frac{g\mu_B}{\hbar}\hat{\vec{S}}=\gamma\hat{\vec{S}} \tag{2.61}$$

γ is called the gyromagnetic ratio.
Implementing (2.61), (2.1), and (2.10) into (2.60),

$$\boxed{\frac{d}{dt}\vec{M}(t)=\mu_0\gamma\left(\vec{M}(t)\times\vec{H}(t)\right)} \tag{2.62}$$

(2.62) is the Larmor precession term for the magnetization.
If the field is time independent, (2.62) implies that the amplitude of the magnetization is a time constant, as well as its projection onto the field. This describes very well a precessional movement as described in Fig. (2.13): the magnetization precesses around the field with a frequency of

$$\omega_0=-\mu_0\gamma H=\gamma_0 H \tag{2.63}$$

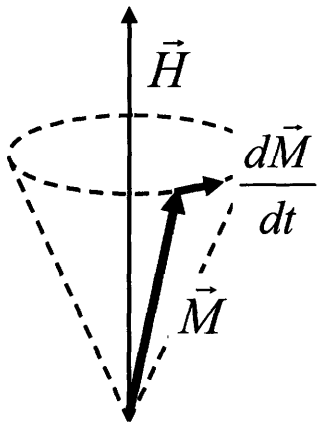

Figure 2.13 Larmor precession in a time independent field.

To account for saturation of magnetization at high fields, a damping term is introduced in (2.62). We then obtain the **Landau-Lifshitz-Gilbert** (LLG) equation:

$$\boxed{\frac{d}{dt}\vec{M}(t) = -\gamma_0\left(\vec{M}(t)\times\vec{H}(t)\right) + \frac{\alpha}{M_S}\left(\vec{M}(t)\times\frac{d\vec{M}(t)}{dt}\right)} \tag{2.64}$$

where α is the **phenomenological damping parameter** and M_S the saturation magnetization. The damping precession is illustrated in Fig. (2.14)

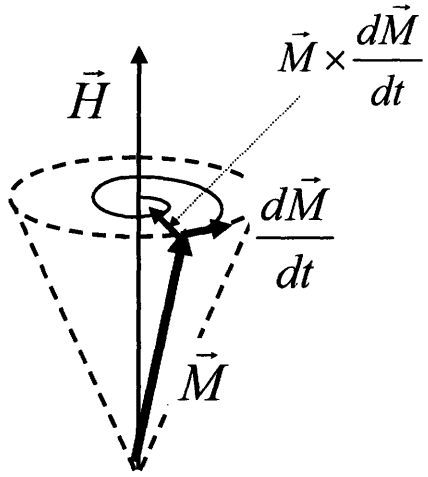

Figure 2.14 Magnetization precession with damping phenomenon.

In 2.64 the applied field is usually replaced by the effective field acting on the magnetization and that accounts for anisotropy, applied field and exchange energy. It is defined as:

$$\vec{H}_{eff} = -\frac{1}{\mu_0}\frac{\delta E_{total}}{\delta \vec{M}} \tag{2.65}$$

where E_{total} is defined in 2.44.

The LLG equation describes the dynamics of the magnetization inside a ferromagnet with or without an external applied field.
In section 2.2.2, we have described the influence of the magnetization on the electrical transport properties. We now describe the action of the current on the local magnetization.

2.2.3.2 Oersted field

The first effect of the current on the local magnetization that comes to mind is the Oersted field that any current generates around itself following the Biot and Savart Law:

$$\vec{B}_{Oersted}(\vec{r}) = \frac{\mu_0}{4\pi} \int_{volume} \frac{\vec{j}(\vec{r}\,') \times (\vec{r} - \vec{r}\,')}{|\vec{r} - \vec{r}\,'|^3} \cdot dV \qquad (2.66)$$

where $\vec{j}$ is the current density.

This equation is strictly speaking only valid in the magnetostatic approximation.
It is equivalent to Ampere's law, even in the specific case of discontinuous currents like the square pulses used in this work (see section 3.2) [23]. This effect proves to have a lot of importance in the devices studied because of their multilayer structure.

In Figure 2.15, the current going through a parallelepiped 1.47 μm long, 270 nm wide and 6 nm thick is modeled as an array of finite wires distributed every 1nm over the cross section. The Oersted field created by each wire is calculated at any point of the plane Z=3 nm (with an increment of 4 nm in Y and X direction). That plane is extended in the X direction of 335 nm on each side (in order to simulate parts where there is no electron flow as seen in the devices studied in chapter 4). That plane constitutes a plane of symmetry for the current distribution and therefore the field is expected to be orthogonal to the plane, which is a hard axis anisotropy direction (shape anisotropy, polycrystalline patterned thin film with no texture).

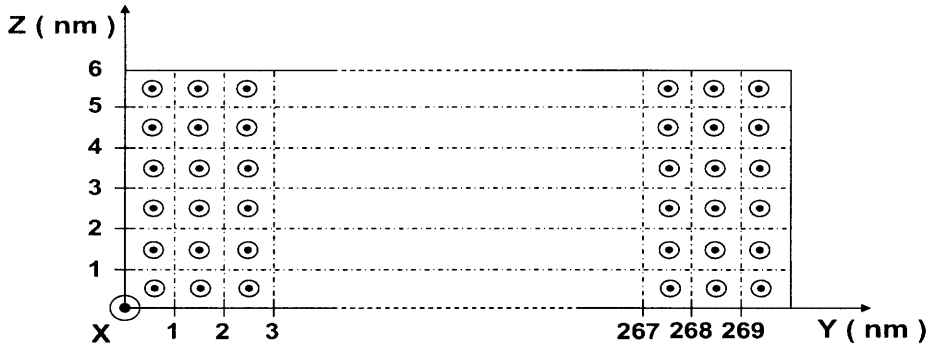

Figure 2.15 Model used for the calculation of the Oersted field in a single layer thin film 2.14 μm long, 6 nm thick and 270 nm wide. The current is modeled as an array of finite 1.47 μm wires distributed every 1 nm in Y and Z direction, starting at Y=Z=0.5 nm. The field is calculated at any point of the longitudinal cross section defined by Z=3 nm and with an increment of 4 nm in the X and Y direction, starting at X=Y=Z=0.

As expected, Fig. 2.16 shows a field with only a Z component, and localized mainly at the edges [24], with an amplitude much lower than a typical perpendicular anisotropy, i.e. it will have negligible effects on magnetization.

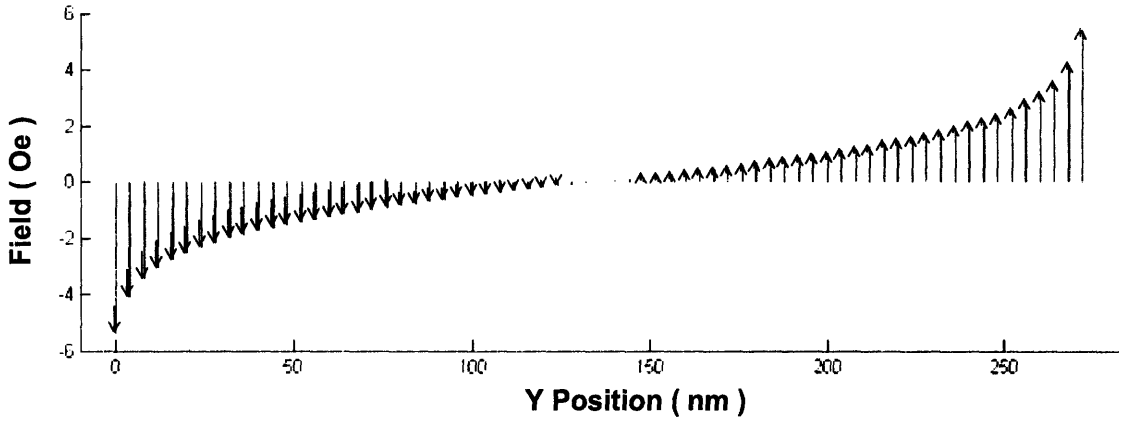

Figure 2.16 Oersted field in a single layer described in Fig. 2.15, evaluated at X=1 μm.

But, if in a thin conductive single layer, the Oersted field created by the current going through is essentially out of plane, which is a very high anisotropy direction, and localized mainly at the edges as seen in Fig(2.16). However, in a multilayer thin film, the current going through each layer generates in the other layers a non trivial field in the plane of the film as seen in Fig. 2.17.right. The multilayer is composed of the single layer defined in Fig. 2.15, with three additional layers on top with same length and width, but with different thicknesses (namely from bottom to top, 4 nm, 5 nm and 4 nm) and materials, i.e., resistivities. The current distribution is modeled in the same way as in the single layer, using the parallel resistor model to attribute to each layer its share of the current density, and the field is calculated in the very same plane of the bottom layer defined in Fig. 2.15.

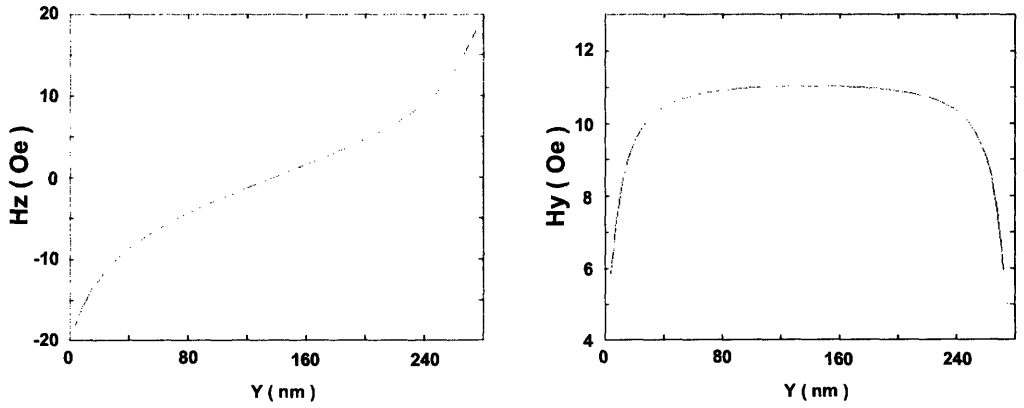

Figure 2.17 Oersted field distribution created by a multilayer stack evaluated at X=1 μm.

If the Oersted field is a straightforward effect of a current on a ferromagnet, more subtle effects arise when passing a current through a ferromagnetic material. The hydromagnetic drag and the spin transfer torque are two important such effects.

2.2.3.3 Hydromagnetic drag.

The Hall effect around a domain wall creates a force on the wall known as the hydromagnetic drag [25-27]. In each single domain, the Lorentz force on the charge carriers is compensated by the electrical field it induces, allowing the charge carrier to move in the external applied electric field direction. When going through a 180° domain wall, the induced electric field reverses, and this induces a non uniform current distribution (Fig. 2.18.left), which is the superposition of the undisturbed current flow (Fig. 2.18.center) and eddy current loops (Fig 2.18.right) that generate a magnetic field (Ampere or Biot and Savart) that exerts a force on the domain wall (rigorously a torque on the local magnetization) so that the wall is displaced in the direction of the charge carriers' drift.

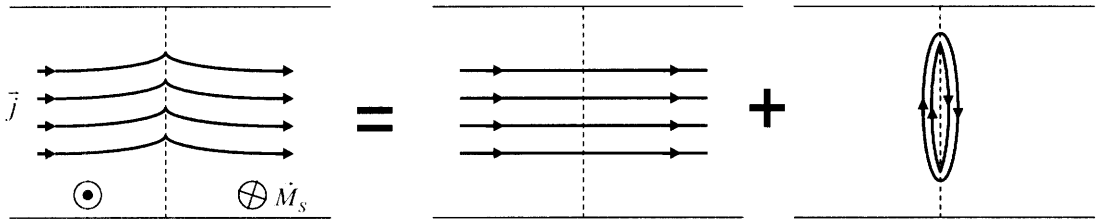

Figure 2.18 The non uniform current distribution in a 180° Bloch or Néel wall (left) can be decomposed into a uniform current distribution (center) and eddy current loops (right) around the wall. After Ref [28].

The force is proportional to the cross section of the wall and therefore, in thin films, to the film thickness. The hydromagnetic drag will be negligible for thicknesses below ~100 nm [29]. Besides, the model developed by Berger [25] was developed for Bloch or Néel walls, in thick films or bulk material. For the devices studied in this thesis, the walls have a very different structure: 180° head to head or tail to tail domain walls (transverse or vortex), which implies that in each domain there is no Hall effect, and the total thicknesses are of the order of 20 nm and therefore hydromagnetic drag is negligible.

The last effect of the current on the magnetization is the so called spin-transfer torque effect.

2.2.3.4 Spin-transfert torque

The theoretical origin of that effect is the **conservation of angular momentum** and its description was also pioneered by Luc Berger [30] who termed the phenomenon s-d exchange force (between the localized 3d electrons responsible for ferromagnetism and the delocalized 4s electrons carrying the current). As described in section 2.2.2.1, in a single domain, the electrons of the current are predominantly spin-up, since those are less scattered, i.e. with spins antiparallel to the local magnetization (the gyromagnetic ratio of

electrons being negative equation 2.61). The current is said to be **polarized**. The polarization factor is classically defined as:

$$P = \frac{n_\uparrow - n_\downarrow}{n_\uparrow + n_\downarrow} \tag{2.67}$$

where $n_\uparrow$ and $n_\downarrow$ indicate the population of current electrons with spin-up and spin-down respectively. When going through a domain wall or through an interface where there is a change of magnetization, and the spin polarized current must change, e.g. in a 180° domain wall, the spin-up become spin-down and vice versa. That change occurs with the loss of a part of the magnetic moment of the electrons of the current. But since the total magnetic moment of the system must be conserved, that component is passed on to the local magnetization through s-d exchange interaction.

If we denote as $\vec{p}$ the direction of the magnetic moment of the predominant electron channel, and $\vec{m}$ the unit vector of the local magnetization, the component of the magnetic moment of the electron that is transmitted to the local magnetization is proportional to $\vec{m} \wedge (\vec{m} \wedge \vec{p})$: it is proportional to the projection of the magnetic moment onto the plane perpendicular to the magnetization, and it acts on $\vec{m}$ so as to align it with $\vec{p}$. In a domain wall, if the magnetization evolves slowly enough so that the magnetic moment of the electrons is almost aligned with it, the domain wall is said to be **adiabatic**. If we denote as y the direction of the electron flux, in an adiabatic wall, the electron in y arrives with a magnetic moment aligned with the local magnetization of the abscissa y-dy:

$$\vec{p}(y) = \vec{m}(y - dy) \tag{2.68}$$

and therefore,

$$\vec{m} \wedge (\vec{m} \wedge \vec{p}) = dy.(\vec{u}_y \bullet \vec{\nabla}).\vec{m} \tag{2.69}$$

with $\vec{u}_y$ being the unit vector of the current (opposite to the electron flux).

The number of electrons going through the mathematical layer between y and y+dy during a time dt is $|J|.S.dt/e$. The total magnetic moment of that number of electrons is therefore $P \cdot \frac{|J|.S.dt}{e} \cdot \frac{\hbar}{2} \cdot \gamma$

The change of magnetization induced by spin transfer torque is:

$$d\vec{M} = S \cdot dy \cdot M_S \cdot d\vec{m} = P \cdot \frac{|J|.S.dt}{e} \cdot \frac{\hbar}{2} \cdot \gamma \cdot dy \cdot (\vec{u}_y \bullet \vec{\nabla})\vec{m}$$

which leads to

$$\boxed{\left.\frac{d\vec{m}}{dt}\right|_{transfer\ \ spin} = -\frac{g.\mu_B.P.J}{2.e.M_S}(\vec{u}_y \bullet \vec{\nabla}).\vec{m}} \tag{2.70}$$

If we define

$$\boxed{\vec{u} = \frac{g.\mu_B.P}{2.e.M_S}\vec{J}} \tag{2.71}$$

as the generalized velocity, this torque transforms the LLG equation 2.64:

$$\boxed{\frac{d\vec{m}}{dt} = -\gamma_0 \vec{H} \wedge \vec{m} + \alpha.\vec{m} \wedge \frac{d\vec{m}}{dt} - \left(\vec{u} \bullet \vec{\nabla}\right).\vec{m}} \qquad (2.72)$$

This adiabatic spin transfer torque term can account for domain wall motion induced by current. **The domain wall will move in the direction of the electron flux when the current density is higher than a critical value**. This term can be regarded as the continuous limit of the spin transfer term introduced by Slonczewski [31] where he considered electrons going through only two layers of different magnetization in a CPP geometry. Equation 2.72 suggested by Thiaville et al. [32], when considering edge roughness, gives wall velocities two orders of magnitude higher than experimentally observed [33], as well as higher critical currents than observed. Refinements to the theory in order to account for these discrepancies have been proposed. One was to include a non-adiabatic contribution [34,35]. In an non-adiabatic process, the electron spin cannot locally follow the magnetization. Be it phenomenologically [34] or after a physical derivation [35], a similar extended LLG equation is obtained:

$$\boxed{\frac{d\vec{m}}{dt} = -\gamma_0 \vec{H} \wedge \vec{m} + \alpha.\vec{m} \wedge \frac{d\vec{m}}{dt} - \left(\vec{u} \bullet \vec{\nabla}\right).\vec{m} + \beta \cdot \vec{m} \times \left[\left(\vec{u} \bullet \vec{\nabla}\right).\vec{m}\right]} \qquad (2.75)$$

where β is the phenomenologically introduced non-adiabatic parameter, and can be identified with:

$$\beta = \left(\frac{\lambda_{ex}}{\lambda_{sf}}\right)^2 \qquad (2.76)$$

where λ_{ex} is the exchange length and λ_{sf} the spin flip length [34].

Furthermore, the domain wall spin structure itself was predicted to change as the current flows through the domain wall [36]. Micromagnetic simulations of a wall under a spin polarized current in NiFe wires showed the change of a DW from a transverse structure to a vortex structure [34]. This theoretical prediction was confirmed by a few experiments, the most complete and definitive of which was conducted by S. Parkin and his team at IBM, in which the DW transformed from transverse to vortex and back. [37].

The critical current density was proved to be temperature dependent [38], and the domain wall velocity was found to increase with increasing temperature in a ferromagnetic semiconductor [39], which drove an interest on how the different LLG terms would depend on temperature. Finally, the Joule effect heating can have important consequences: a local heating of the ferromagnet above the Curie temperature can cause the nucleation of domain walls [33]. The fact that experimental domain wall velocities did not reach the theoretical predictions was attributed to spinwaves which dissipate the angular momentum [40].

The spin transfer torque effect proves to be an extremely complicated phenomenon whose theoretical complete explanation is yet to be accomplished.

The theoretical background introduced in this chapter allows to precisely determine which effects are predominant in the devices characterized in this work. The devices, whose structure and fabrication will be further detailed in next chapter, are patterned Pseudo Spin Valve (PSV) thin films with shapes of bars or rings, with a few microns in the long dimension, widths of ~ 300 nm or less and thicknesses below 20 nm. The magnetization state will be dictated mostly by the shape anisotropy, since each layer of the PSV stack is composed of a polycrystalline thin film with weak texture. Besides, the stray field of each ferromagnetic layer will interact with the magnetization of the other, an effect called magnetostatic coupling which will be extensively studied for each device. The reduced dimensions of the devices will favor a reduced number of domains separated by transverse or vortex domain wall structures. The devices will display GMR. The current will act on the magnetization via its Oersted field and the spin transfer torque, but the hydromagnetic drag effect will be negligible.

The next chapter describes how these devices were fabricated and which methods were used for their characterization.

[1] M Beleggia, and M. De Graef, J. Magn. Magn. Mater. **263**, L1-L9 (2003).
[2] J. C. Maxwell, Electricity and Magnetism, third edition, Vol. **2**, pp. 66-70 (1904).
[3] J.A. Osborn, Phys. Rev. **67**, 351 (1945).
[4] R. C. O'Handley, Modern Magnetic Materials, pg 47, Wiley-Interscience Publication (2000).
[5] A. H. Morris, The physical Principles of Magnetism, p11-12, IEEE Press (2001).
[6] L.H. Thomas, Phil. Mag. **3**, 1 (1927)
[7] L. Néel, J. Phys. Rad. **15**, 225-239 (1954).
[8] H. Takayama, K-P Bohnen, and P. Fulde, Phys. Rev. B **14**, 2287 (1976).
[9] J. Bennet, and B. R. Cooper, Phys. Rev. B **3**, 1642 (1971).
[10] U. Gradmann, and J. Müller, Phys. Status Solidi **27**, 313 (1968).
[11] O. Fruchart, and A. Thiaville, C. R. Physique **6**, 921-933 (2005).
[12] E.E. Huber, D.O. Smith, J.B. Goodenough, J. Appl. Phys. **29**, 294 (1958).
[13] K. Kirk, M. Scheinfein, J. Chapman, S. McVitie, M. Gillies, B. Ward, and J. Tennant, J. Phys. D: Appl. Phys. **34**, 160-166 (2001).
[14] Y. Nakatani, A. Thiaville, and J. Miltat, J. Magn. Magn. Mater. **290-291**, 750 (2005).
[15] B. D. Cullity, Introduction to Magnetic Materials, pg 138, Addison-Wesley Publishing Company (1972).
[16] J. C. Slater, Phys. Rev. **49**, 537 (1936).
[17] E. C. Stoner, Phil. Mag. **15**, 1080 (1933).
[18] S.S.P. Parkin, Ultrathin Magnetic Structures II, Springer-Verlag Berlin Heidelberg, Chapter 2.4, 157 (1994).
[19] N. Mott, Proc. Roy. Soc. **156**, 368 (1936).
[20] S.S.P. Parkin, Ultrathin Magnetic Structures II, Springer-Verlag Berlin Heidelberg, Chapter 2.4, 156 (1994).
[21] M.N. Baibich, J.M. Broto, A. Fert, F. Nguyen-Van-Dau, F. Petroff, P. Etienne, G. Creuzet, A. Friedrich, and J. Chazelas, Phys. Rev. Lett. **61**, 2472 (1988).
[22] J. Miltat, G. Albuquerque, and A. Thiaville, Topics Appl. Phys. **83**, 1-33 (2002).
[23] Z. Qihou, Eur. J. Phys. **8**, 128 (1987).
[24] A. Thiaville, Y. Nakatani, J. Miltat, and Y. Suzuki, Europhys. Lett. **69**, 990 (2005).
[25] L. Berger, J. Phys. Chem. Solids **35** (1974).
[26] W.J. Carr, J. Appl. Phys. **45**, 394 (1974).
[27] S.H. Charap, J. Appl. Phys. **45**, 397 (1974).
[28] L. Berger, J. Appl. Phys. **49**, 2156.2161 (1978).
[29] C. H. Marrows, Adv. Phys. **54**, 585.713 (2005).
[30] L. Berger, J. Appl. Phys. **55**, 1954.1956 (1984).
[31] J. C. Slonczewski, J. Magn. Magn. Mater. **159**, L1.L7 (1996).
[32] A. Thiaville, Y. Nakatani, J. Miltat, and N. Vernier, J. Appl. Phys. **95**, 7049.7051 (2004).
[33] A. Yamaguchi, T. Ono, S. Nasu, K. Miyake, K. Mibu, T. Shinjo, Phys. Rev. Lett. **92**, 077205 (2004).
[34] A. Thiaville, Y. Nakatani, J. Miltat, and Y. Suzuki, Europhys. Lett. **69**, 990.996 (2005).
[35] S. Zhang and Z. Li, Phys. Rev. Lett. **93**, 127204 (2004).
[36] X. Waintal and M. Viret, Europhys. Lett. **65**, 427.433, (2004).

[37] www.physics.hku.hk/~spintron/presentations/**parkin**_magnetic.pdf.
[38] M. Laufenberg, W. Bührer, D. Bedau, P.-E. Melchy, M. Kläui, L. Vila, G. Faini, C. A. F. Vaz, J. A. C. Bland, and U. Rüdiger, Phys. Rev. Lett. **97**, 046602 (2006).
[39] M. Yamanouchi, D. Chiba, F. Matsukura, T. Dietl, and H. Ohno, Phys. Rev. Lett. **96**, 096601 (2006).
[40] G. Tatara and H. Kohno, Phys. Rev. Lett. **92**, 086601 (2004).

Chapter 3

Fabrication and experimental methods

3.1 Fabrication description.

3.1.1 General description.
3.1.2 Some delicate aspects of fabrication.

3.2 Device characterization.

3.2.1 Field induced measurement settings.
3.2.2 Current induced measurement settings.
3.2.3 Micromagnetic simulations.

3.1 Fabrication Description.

3.1.1 General description.

The devices fabricated and characterized in this work are NiFe/Cu/Co/Au Pseudo Spin Valve (PSV) patterned thin films with dimensions of a few microns and below. Electrical contacts were deposited on top to enable GMR measurements and current induced switching. We use three main steps to obtain connected working devices: defining first the external electrical contacts using optical lithography and then, using two successive aligned e-beam lithography steps, defining the PSV devices themselves and finally the electrical leads contacting the devices to the external electrical contacts. The external electrical contacts are the only ones that the bare eye can see (Fig. 3.1.a and 3.1.b), most of the final contacts can be seen with an optical microscope (Fig. 3.1.c). To picture the devices themselves, Scanning Electron Micrography is used (Fig. 3.1.d).

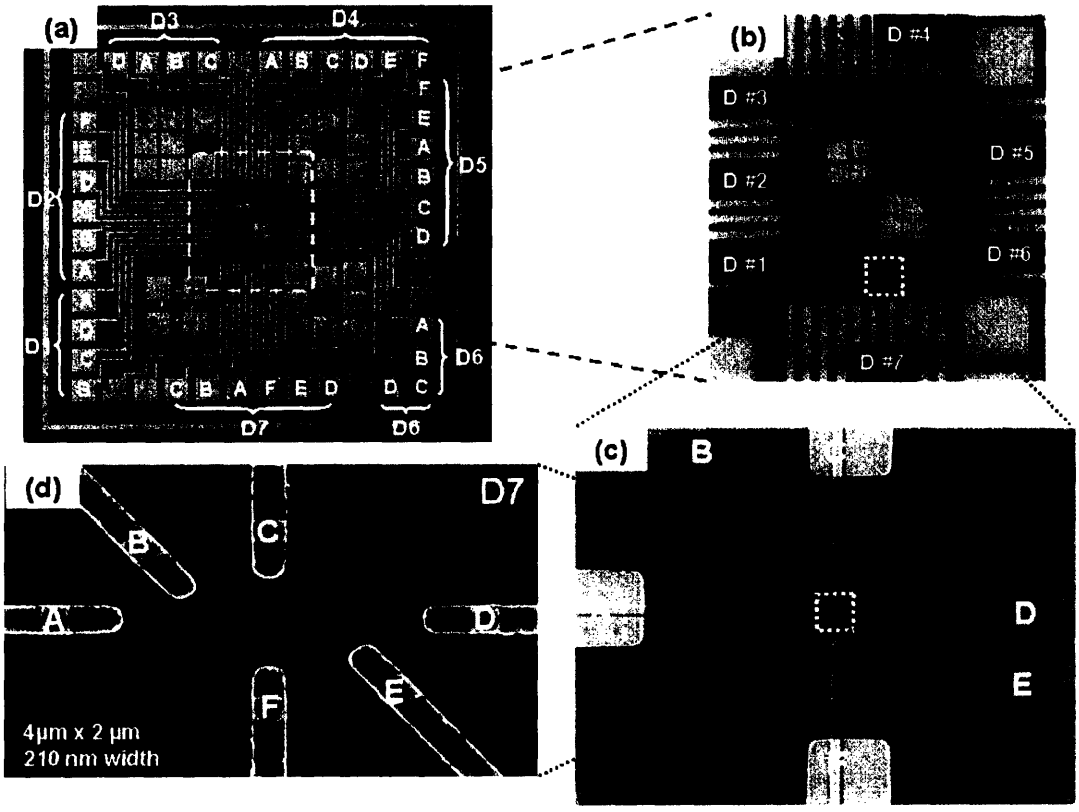

Figure 3.1: (a) Picture of the entire chip, whose center part (b) contains seven devices. Final contacts patterned in PMMA are seen going from the external contacts (c) to the devices imaged with SEM in (d).

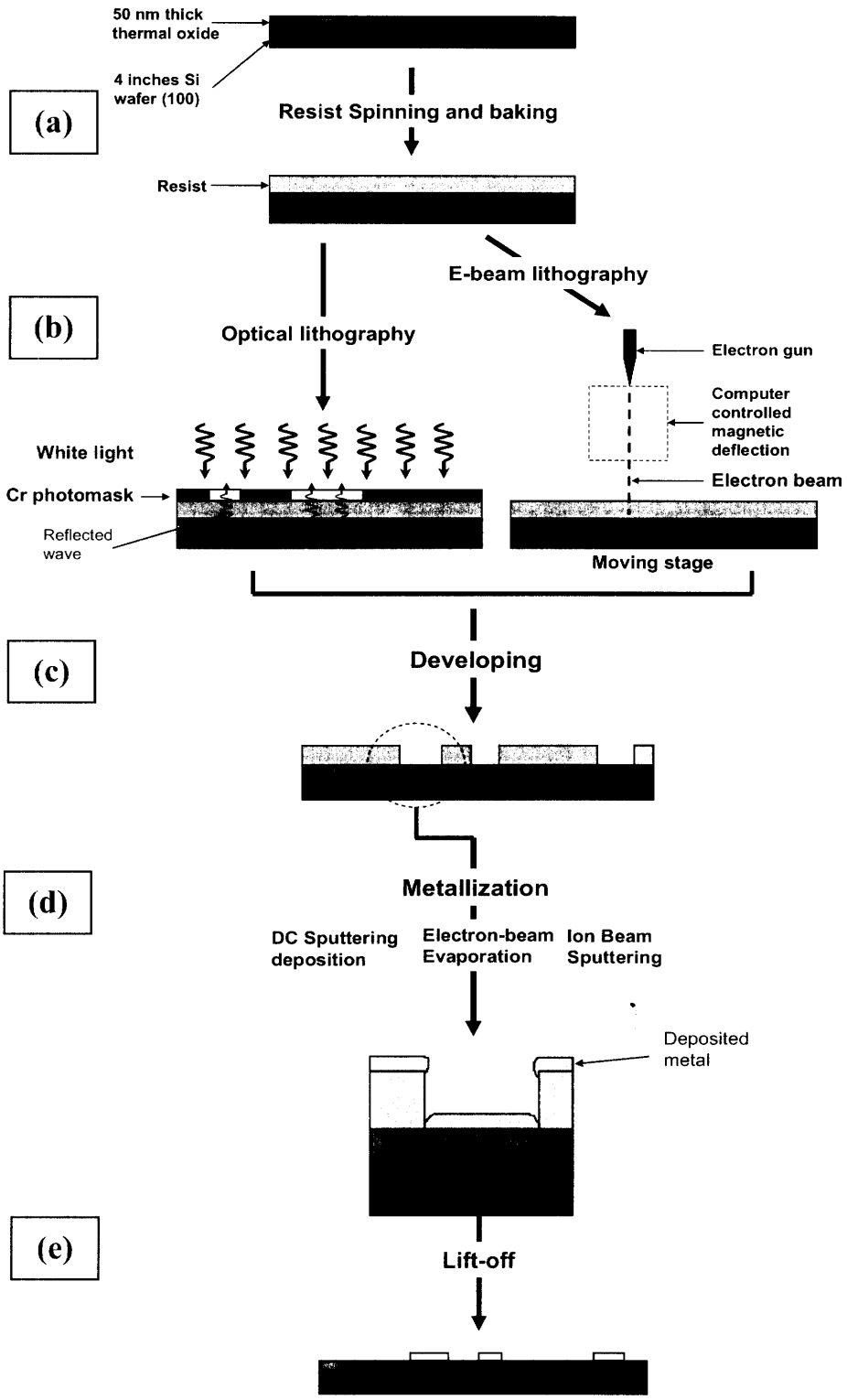

Figure 3.2: Lithography processes.

The **first step** is to define a template on 18-13 positive photoresist (Shipley) using optical lithography and a standard Cr photomask. Si (100) 4' wafers with 50 nm thick thermal oxide were first spun with hexa-methyldisilazane (HMDS) to improve the adhesion of the photoresist on the oxide. The resist was then spun at 6 krpm (~1.2 μm) and baked at 90°C for 90 s (Fig. 3.2.a). The exposure time ranged from 20 to 30 s, the intensity was 4500 μW cm^{-2} (Fig. 3.2.b left). The wafer was then developed using Microposit 352 (Shipley) for 60 s and then rinsed in deionized water and blown dry with N_2 (Fig. 3.2.c) . Ti seed layer (5 nm) and Au (25 nm to 35 nm) were then deposited by e-beam evaporation (Fig. 3.2.d). The lift off was then achieved by immersing the wafer into 1methyl-2pyrrodidinone (NMP) at 120°C during 5 minutes, with a final ultrasonic bath for 60 s (Fig. 3.2.e). The wafer was then rinsed using isopropyl alcohol (IPA) and blown dry with N_2.

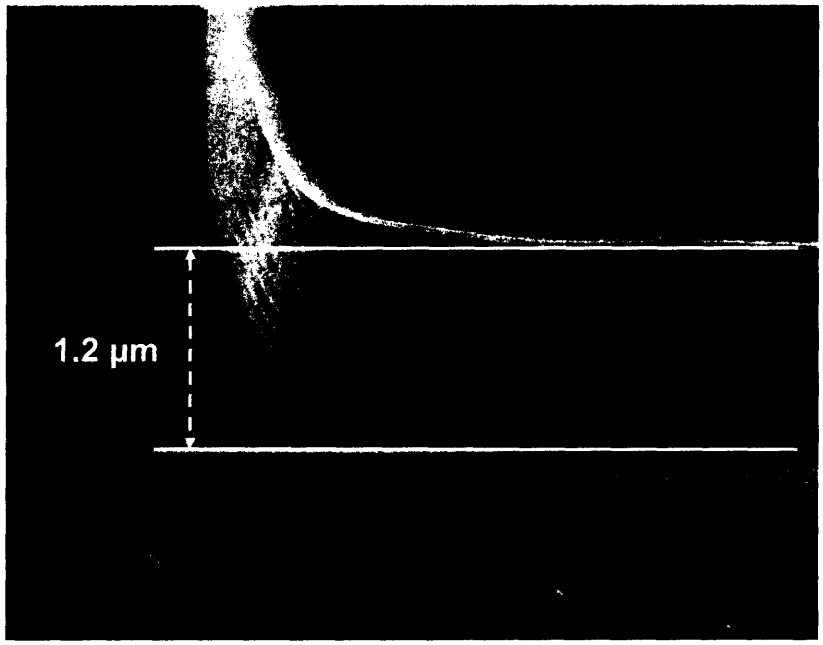

Figure 3.3: Scanning electron micrograph (SEM) of a corner from a pattern defined by optical lithography and deposited by evaporation.

Figure 3.3 shows the SEM of a detail in a pattern defined using the process just described, after deposition of the metallic thin film, before the lift off. The ripples on the section of the coated resist correspond to the interference between the incoming light and the reflected light during the contact printing exposure generating a standing wave interference side wall profile.

The **second step** allowed for the definition of the PSV patterns. The positive resist used to define the patterns of the devices is polymethyl methacrylate 950 (PMMA) diluted in chlorobenzene to 2%. It is spun at 3 krpm (~120nm) and oven baked at 155°C for 60 minutes (Fig. 3.2.a). The pattern predefined on computer software is then written with

electron-beam lithography with an acceleration voltage of 10 kV and a base dose of 100 $\mu C\ cm^{-2}$ (Fig. 3.2.b right). Before writing, a careful alignment is required with the external contacts already in place. As can be seen in Fig. 3.1.a, the external contacts provide a straightforward x-y basis which is used for the alignment. Around the seven devices, alignment marks are also written during this step to allow for the alignment of the final contacts during the last step. The resist is then developed for 90-120 s in 3:1 methyl-isobutyl-ketone (MIBK): IPA (Fig. 3.2.c). The wafer was then rinsed using isopropyl alcohol and blown dry with N_2. The PSV stack was then deposited either by Ion Beam Sputtering (IBS), electron-beam evaporation or DC-triode sputtering (Fig. 3.2.d). The soft layer, Permalloy $Ni_{80}Fe_{20}$ (NiFe), was first deposited. A spacer layer of Cu was then deposited, followed by the hard layer of Co and a capping layer of Au. The lift off was then operated in the same way as in the optical lithography step with a 30 s ultrasonic bath (Fig. 3.2.e).

The **third step** allowed for the definition of the final contacts. The procedure is very similar to the one just described. The PMMA is ~180 nm thick, baked during 60 minutes at 155°C. The pattern is defined using the same software, written with electron-beam lithography with an acceleration voltage of 10 kV and a base dose of 100 $\mu C\ cm^{-2}$, and the alignment is repeated for each device with the alignment marks defined during the previous step. After developing, the final contacts were deposited in the UHV sputter system. A seed layer of Ta of ~3 nm was first deposited to insure that the final contacts would stick to the gold of both the external contacts and of the capping layer of the PSV devices. The conductive Cu layer was then DC sputtered with a thickness that ranged from 100 nm to 130 nm. A Au capping layer of ~10 nm was finally deposited. No ultrasonic bath was used during the lift-off.

3.1.2 Some delicate aspects of fabrication.

The result of those three successive lithographies is extremely dependant on how each step was executed particularly for patterns with < 100 nm minimum-feature-size (MFS). To obtain perfect looking small devices like those seen in Fig 3.4.a and 3.4.c, every parameter has to be optimized and well-controlled. For instance, a change of a few percents in the humidity of the air is enough to drastically reduce the thickness of the spun PMMA, leading eventually to a failed lift-off (since the metal deposited on top for the final contacts becomes almost as thick as the resist). Over exposing the baked resist during the e-beam lithography can lead to very annoying results such as short circuits (Fig 3.4.d). The different methods used to deposit the metal also leads to different results. As seen in Fig 3.4.b, the electrical contact leads show clearly a section shaped like a crown with spikes on the edges. This is due to the fact that the DC sputtering deposition technique used is quite conformal, unlike IBS or electron-beam evaporation as is sketched in Fig 3.5.

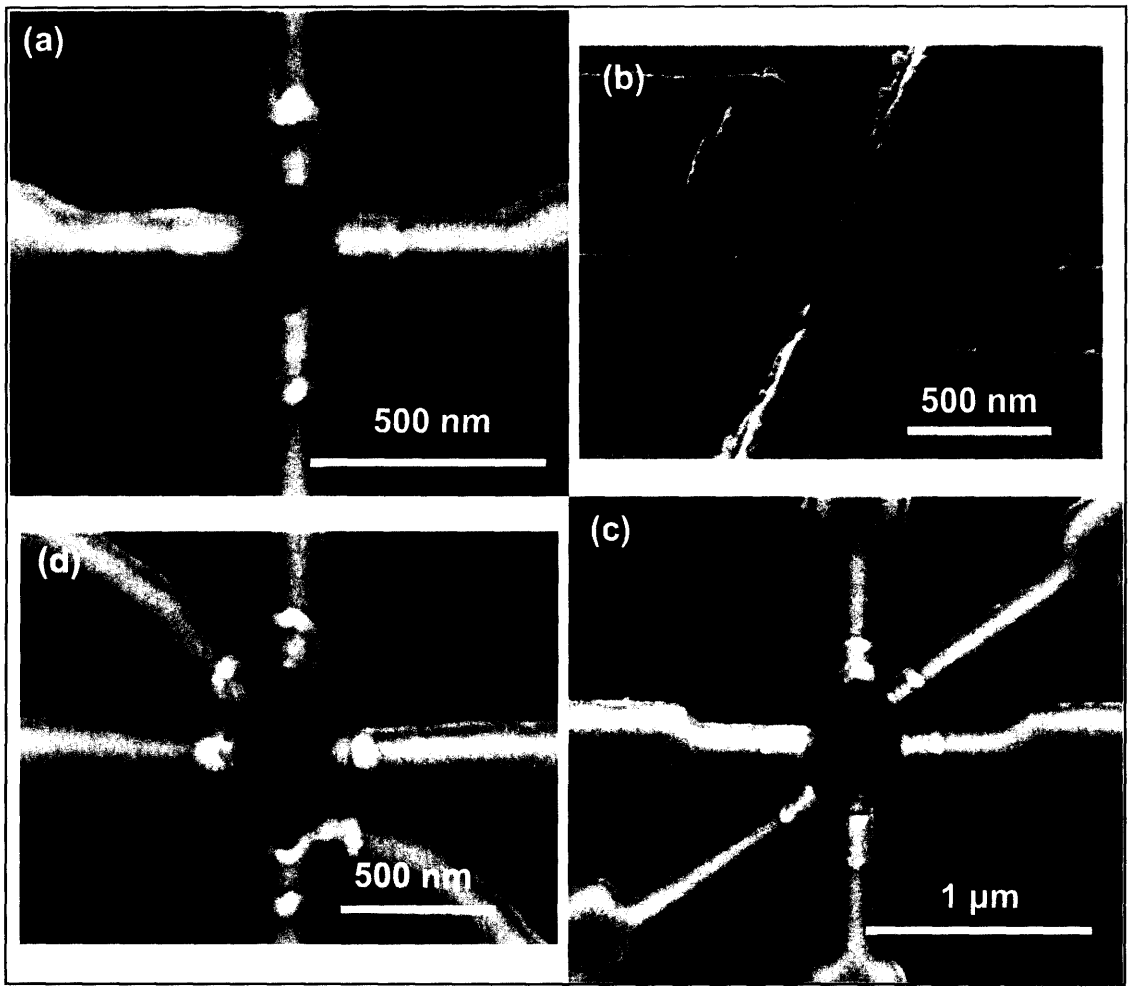

Figure 3.4: Scanning electron micrographs (SEM) of elliptical rings with different dimensions and contact configuration.

A good alignment between the final contacts and the devices is also very important, especially when the dimensions of the devices shrink down into the submicron range. For instance, the contacts along the long axis in Fig 3.4.b are slightly misaligned. It is also the case for the ring in Fig 3.4.a in which the contacts are shifted to the right, but considering the extremely small dimensions of that ring, that very slight misalignment ~50 nm is extremely hard to correct. A good alignment is also important when measuring the ring devices in a Wheatstone bridge configuration, which will be made clearer in Chapter 5.

Furthermore, a very nice looking SEM of a device does not warrant that the final contacts are actually electrically connected to the device. The device in Fig 3.4.c seems absolutely fine, very symmetric, yet the current did not go through. A possible reason may be that, because of the spikes described in Fig 3.5, some resist may remain after the development of the last step, hindering a good ohmic contact.

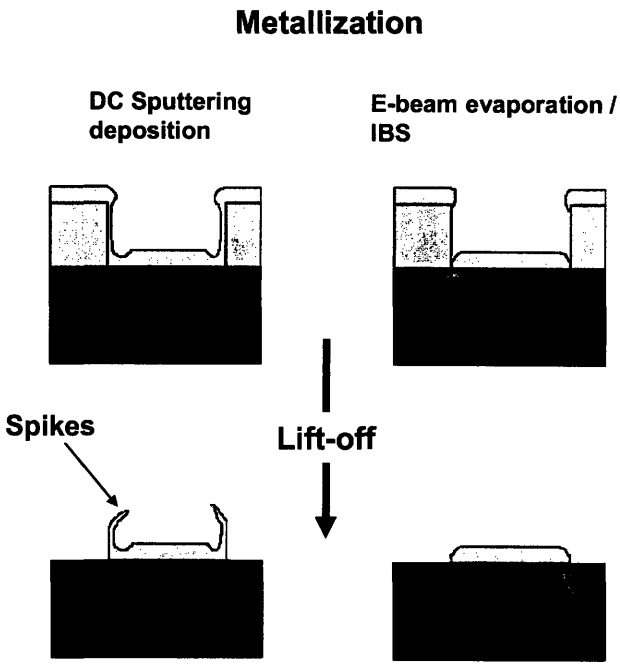

Figure 3.5: Schematics showing the difference between a conformal deposition technique (left) and a more directional one (right).

In Fig 3.4.b, the final contacts show a very clear and interesting pattern: the narrower they get, the thinner they become. Yet the amount of metal sputtered is the same. The reason may be intuited from Fig 3.5 (left). During a conformal deposition, the top of the walls formed by the resist and the walls themselves cast a shadow on the bottom of the trench, and if that trench gets narrower and narrower, the shadow is such that the thickness at the bottom of the trench becomes less than expected, even in its middle. That shadow phenomenon increases with narrower trenches. This is the main limiting factor when trying to reduce the dimensions of the connected devices, since narrower and thinner wires display higher resistances, which causes easier heating.

3.2 Device characterization.

3.2.1 Field induced measurement settings.

The chips were placed on a precision goniometer-rotary-stage located between the poles of an electromagnet which allowed for the accurate alignment of the applied field with the desired direction, usually either the easy axis of the devices or the hard axis. The resistance of the devices was measured at room temperature using a four-point probe technique (see schematics in Fig. 3.6). The current supplied was a sinusoidal wave current with a rms of 10 μA and a frequency of 1 kHz. To avoid melting down the device upon plugging the current, the compliance was set at 100 mV. The voltage drop was measured by an ac lock-in amplifier.

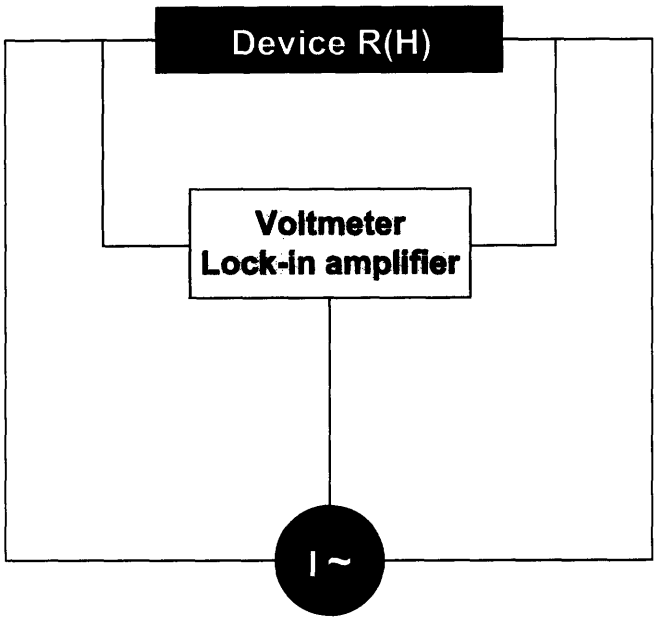

Figure 3.6: Schematics of the AC four-point probe resistance measurement using lock-in detection at 1 kHz. The resistance R measured is a function of the applied field H.

This technique was computer controlled and allowed for precise resistance measurements, non destructive, non heating, using a current well below the critical spin transfer current and generating an Oersted field well below anisotropy fields.

3.2.2 Current induced measurement settings.

The settings used for our current induced measurements are very similar to those for the field induced measurements: using the same current supply, a square pulse of duration 10-100 μs and amplitude ranging from 0.1 mA to 30 mA was sent through the device, and the resistance was then measured using the same method described in section 3.2.1. This computer controlled sequence was repeated after increasing the current pulse amplitude by a predefined increment. An external field could be applied during that process.

The idea behind that whole experimental setting is of course that the resistance gives an indirect insight of the magnetization state of our devices. Micromagnetic simulations were run in parallel to assist in the interpretation of the experimental results.

3.2.3 Micromagnetic simulations.

Micromagnetic simulations were carried out using the 3-dimensional object oriented micromagnetic framework (OOMMF) simulation software [http://math.nist.gov/oommf]. The cell usually used was a cubic box of 4x4x4 nm^3. Standard parameters were used for NiFe (exchange constant $A_{ex}= 1.3\times10^{-6}$ erg/cm, saturation moment $M_s= 860$ emu/cm^3,

$K_1 = 5\times10^3$ erg/cm^3), and Co ($A_{ex} = 3\times10^{-6}$ erg/cm, saturation moment $M_s = 1400$ emu/cm^3, $K_1 = 5.2\times10^6$ erg/cm^3), and the damping coefficient α was set to 0.5. The magnetocrystalline anisotropy direction was set randomly in each cell to model a polycrystalline microstructure. This software uses the LLG equation defined in section 2.2.3.1 with the equations 2.64 and 2.65 which gives the dynamic evolution of the sample magnetization under the constraint of minimizing its total energy. A constant external applied field can be simulated, as well as a more complex distribution such as the Oersted field. No spin torque transfer effect was included in the simulations.

The devices, whose fabrication and characterization methods have been described in this chapter, display GMR as described in the previous chapter. Experimental and simulation results as well as physical interpretations are detailed in the next two chapters.

Chapter 4

Notched Pseudo Spin Valve bars.

4.1 Introduction.

As described in section 2.2.3.3, current induced domain wall motion is a very attractive magnetic switching method for applications. Many successful experiments have been done in thin ferromagnetic single layer wires or bars [1-10]. In these structures, the effect of the Oersted field is negligible as shown in section 2.2.3.2 and the spin transfer torque is responsible for the domain wall motion. Threshold current densities are found to be of the order of $10^{11} - 10^{12}$ A/m^2. In single-layer thin film devices, which are tested with the current applied in plane (CIP), the initial domain wall position has been controlled using nanoconstrictions [1], zigzag lines [2, 3], and a pad and wire junction [4, 5]. Wall motion in a variety of different shapes has also been investigated including U-shaped patterns [6, 7], and ring structures [8, 9]. Yamaguchi et al. [10] have measured a domain wall velocity that ranges from 2 to 6 m/s and is highly dependent on the micromagnetic structure of the wall [2, 3].

Compared to the cases of current-induced switching in CPP multilayer pillars and in CIP single-layer structures, there is relatively little work on current-induced switching in CIP multilayer structures. In the CIP geometry, the motion of a domain wall within a multilayer structure can be detected from GMR, and this has been used to give a direct indication of the position of the wall [11]. Grollier et al. [11-14] investigated current-induced domain wall displacement in 20μm-long CoO/Co/Cu/NiFe/Au spin valve wires with widths down to 300 nm, where domain wall motion was obtained at current densities of the order of $10^{11} - 10^{12}$ A/m^2. In narrow wires, both edge irregularities [12] and notches [11] were effective as domain wall pinning sites. The motion of a domain wall was found to be consistent with spin-transfer effects for zero or small bias fields ($H < 7$ Oe), while at higher bias fields the current is believed to unpin the wall, which then moves under the influence of the applied field.

In this work, we have measured CIMS in 2.14 μm-long NiFe/Cu/Co/Au bars with widths of 270 nm, each containing three different notches width depths up to 80 nm. In these PSV bars the magnetostatic coupling between the layers leads to reversal starting from both ends of the bars, rather than by the movement of a single domain through the structure as occurs for longer bars. This in turn allows for one or two domain walls to be located within the bars, which can be moved using current pulses or applied fields. We will describe both field- and current-induced reversal, and show that the Oersted field from the current can lead to switching of the bars in the presence of a bias field.

4.2 Description.

Scanning electron micrographs (SEMs) of the two notched PSV bars characterized in this work are shown in Fig. 4.1. The bars are 2.14 μm long, 270 nm wide, and the e-beam evaporated PSV stack is NiFe (6 nm)/ Cu (4 nm)/Co (5 nm)/ Au (4 nm). The DC triode sputtered final contacts are Ta (2 nm)/ Cu (120 nm) and the outer contacts Ti (5 nm)/ Au (25 nm). The fabrication procedure for these three different stacks was detailed in section 3.1. As can be seen in Fig. 4.1.a, the bars have rounded ends, and a portion at their ends are covered by the final Ta/Au contacts, and since these are much thicker than the PSV stack, the current will preferably flow through the contacts, and therefore the change in resistance measured by the four point probe measurement setting described in section 3.2.1 can be attributed to the portion of the bar between the contacts, which is 1.47 μm long. Both bars contain three notches of different depths (labeled using letters A, B and C). While the notch design in D1 is symmetric with respect to the center of the bar and contains notches with depths of 30, 60 and 30 nm, respectively, the notch configuration for D2 is asymmetric with respect to the center of the device and contains notches with depths of 30, 60 and 80 nm, respectively. Both devices were passivated using 80nm-thick sputtered SiO2.

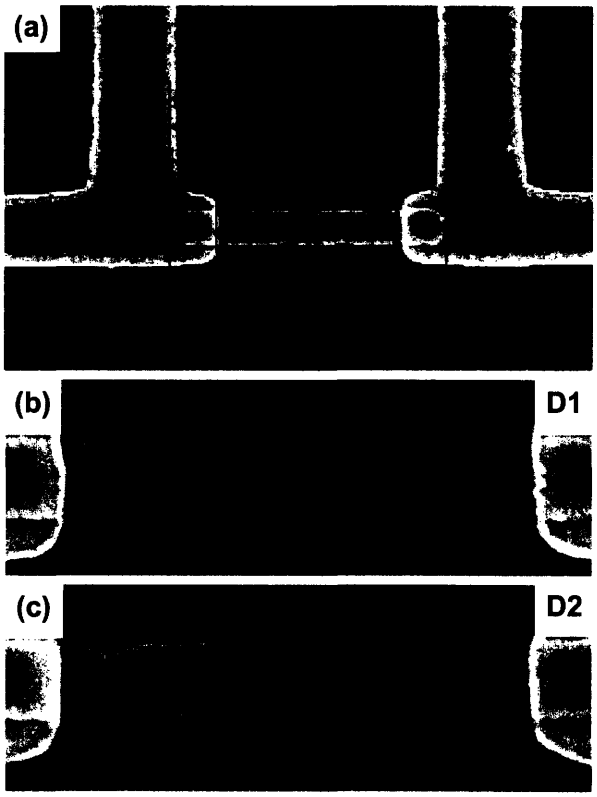

Figure 4.1: Scanning electron micrographs of the notched bars. (a) The four-point electrical contact configuration and the applied field direction. (b) PSV bar with symmetric notch configuration, named D1. (c) PSV bar with an asymmetric notch configuration, named D2. The notches are labeled with letters A, B, and C.

4.3 Field Induced switching.

Figure 4.2 shows the resistance measured for D1 and D2 as a function of the applied magnetic field. As discussed in section 2.2.2.3., a PSV stack displays CIP giant magnetoresistance. The baseline resistance levels (159.2 Ω and 192.0 Ω for D1 and D2, respectively) correspond to parallel alignment of the magnetizations of the Co and NiFe layers, while the highest levels (161.1 Ω and 193.7 Ω for D1 and D2, respectively) correspond to the field ranges over which the NiFe and Co layers are magnetized antiparallel (equation 2.55). The low-to-high resistance transitions, at which the NiFe reverses, occur at low applied fields (+/-50 Oe) through several intermediate resistance values corresponding to intermediate magnetization states which will be further described later. High-to-low resistance transitions, corresponding to the Co reversal, occur at moderate fields (+/-150-200 Oe). Clearly, while the transitions in the loop for D1 are symmetric with respect to zero field, the data for D2 is asymmetric, particularly for the moderate-field transitions.

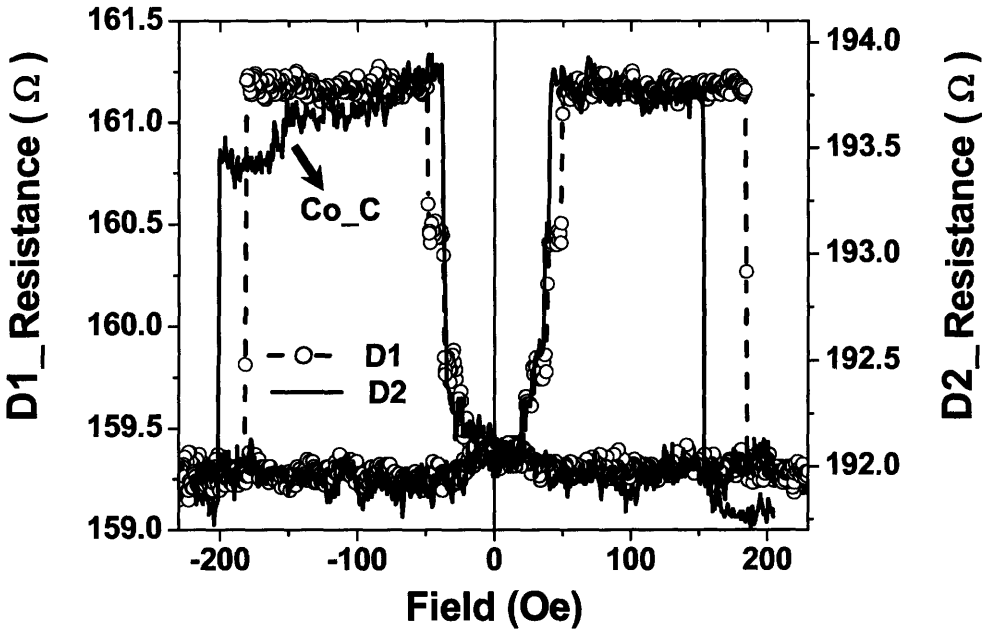

Figure 4.2 Magnetoresistance loops corresponding to the PSV bars with symmetric (D1) and asymmetric (D2) notch configurations with respect to the center of the bar.

The giant magnetoresistance (GMR) ratio defined as

$$r_{GMR}(\vec{H}) = \frac{R(\vec{H}) - R_{//}}{R_{//}} \tag{4.1}$$

was 1.2% and 1.1% for D1 and D2, respectively. These rather low GMR ratios are similar to that of the unpatterned PSV film (1%) and result from current shunting by the Au and Cu layers. While the Cu spacer layer in these PSV bars is thick enough to consider exchange coupling between the NiFe and Co layers negligible [15], this 4nm-

thick layer is sufficiently thin to allow both for GMR effects and for the NiFe and Co layers to be magnetostatically coupled, as found elsewhere in unpatterned spin-valve films, as a result of the stray fields of domain walls [16], as well as in patterned structures as a result of the stray fields from the edges of the layers [17]. The stray field of each ferromagnetic layer, namely the Co layer and the NiFe layers, interacts with the magnetization of the other ferromagnetic layer, NiFe and Co respectively as is clearly seen in Figure 4.3, in which are shown micromagnetic simulations of the two remanent states after positive (Fig 3.4.a) and negative (Fig 3.4.b) saturation.

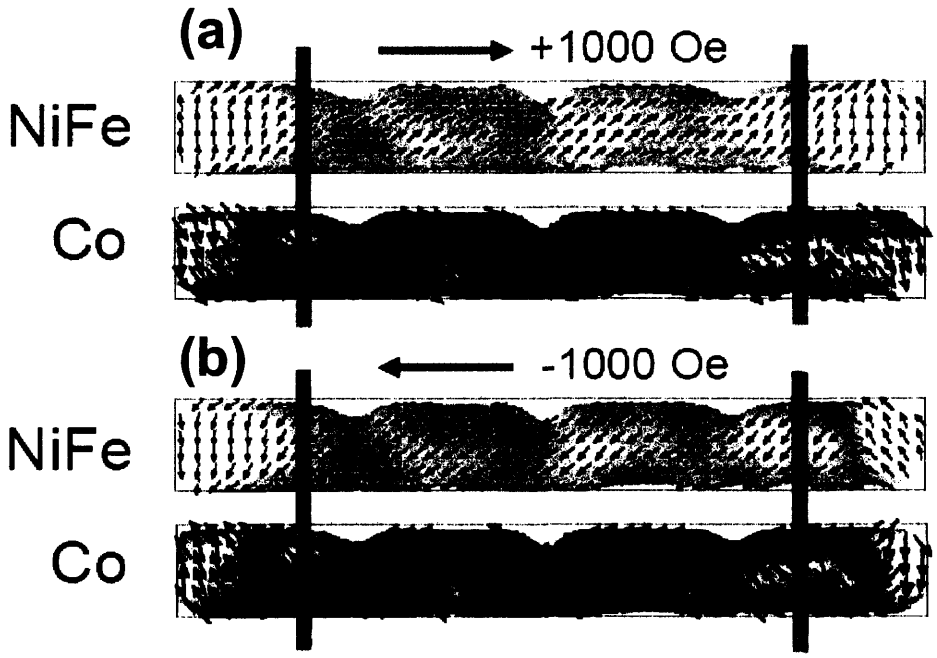

Figure 4.3 (a) and (b) Micromagnetic simulations showing the remanent state in the NiFe and Co layers after applying a +1000 Oe and -1000 Oe saturating field, respectively.

It can be noticed in Fig 4.3 that for both remanent states, the magnetization distributions in each layer are roughly symmetric to one another with respect to the long axis of the bar, and that symmetry finds its origin in the magnetostatic coupling. In Fig. 3.4.a, both soft (NiFe) and hard (Co) layers have a magnetization structure that is very similar to a single domain in the S-state as described in section 2.1.9 Fig. 2.6. But the S-state is different in each layer: the top and bottom of the S points up in the NiFe and down in the Co, thus allowing for the stray field loops to close very locally around the ends of the bar (flux closure of the stray field). The same analysis stands for the remanent state after negative saturation in Fig 4.3.b which displays two different C states.

An experimental evidence of the importance of the magnetostatic coupling lies in the minor loops shown in Figure 4.4.

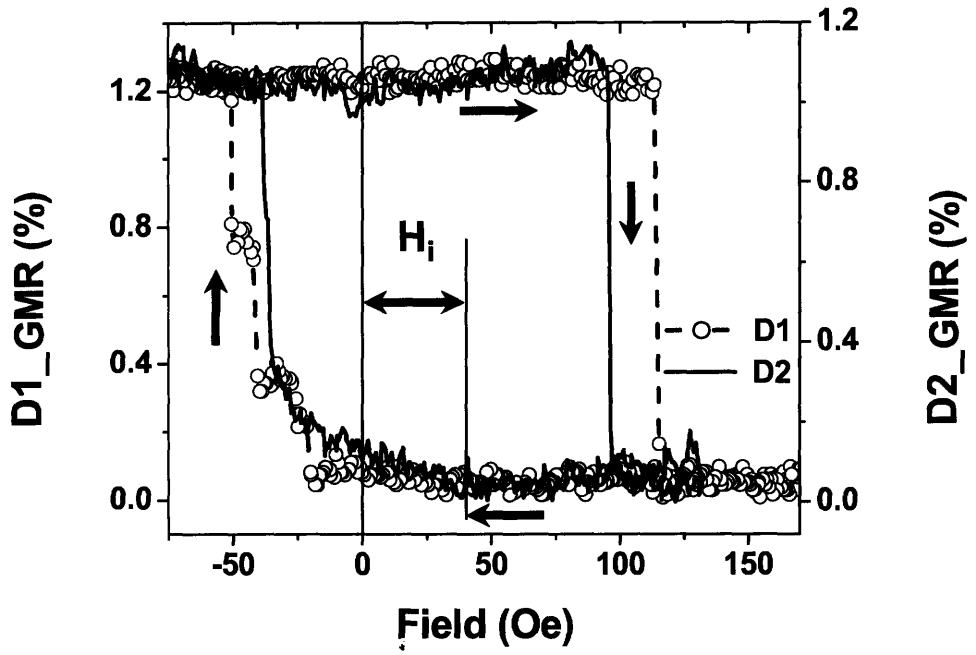

Figure 4.4 Low-field GMR minor loops obtained on cycling the soft (NiFe) layer after saturating both D1 and D2 with a +1000 Oe field. The arrows indicate the cycling direction in the measurements and the average shift of the center of these loops with respect to zero applied field.

After saturating the samples in either positive (as shown in the figure) or negative fields (not shown), cycling in fields up to +/-180 Oe yields minor GMR loops that are asymmetric with respect to zero field and shifted along the positive or negative directions, respectively. The transition from the low resistance to high resistance states occurs below -50 Oe via several intermediate states, as seen on Fig. 4.2. However, the high-to-low resistance transition occurs abruptly at significantly higher fields (114 Oe and 95 Oe for D1 and D2, respectively). These switching fields are higher because the NiFe layer reversal is opposed by magnetostatic coupling from the Co layer which energetically favors the antiparallel state. The shifts, H_i, in these minor loops with respect to zero field (38 Oe and 30 Oe for D1 and D2, respectively) represent the strength of the coupling. These values are comparable to the fields at which the intermediate states form, which emphasizes the importance of magnetostatic coupling in the magnetization reversal of these structures. In comparison, magnetostatic effects are less important in the longer spin-valve bars previously used for CIMS studies, which show symmetric minor GMR loops [12].

The magnetostatic coupling can account, in a more subtle way, for the way the soft layer reverses with the presence of intermediate states.

Figure 4.5 shows dense low-field magnetoresistance loops measured at increments of 0.7 Oe of applied field, corresponding to the reversal of the NiFe soft layers in both PSV bars. By comparing the dimensions of the different sections of the bars defined by the positions of the notches with the relative height of these steps and assuming that the deeper the notch, the higher the pinning potential [18], and therefore the higher the field needed to unpin the wall away form the notch, a detailed picture of the NiFe reversal in both PSV bars may be deduced (see schematics in Fig. 4.5).

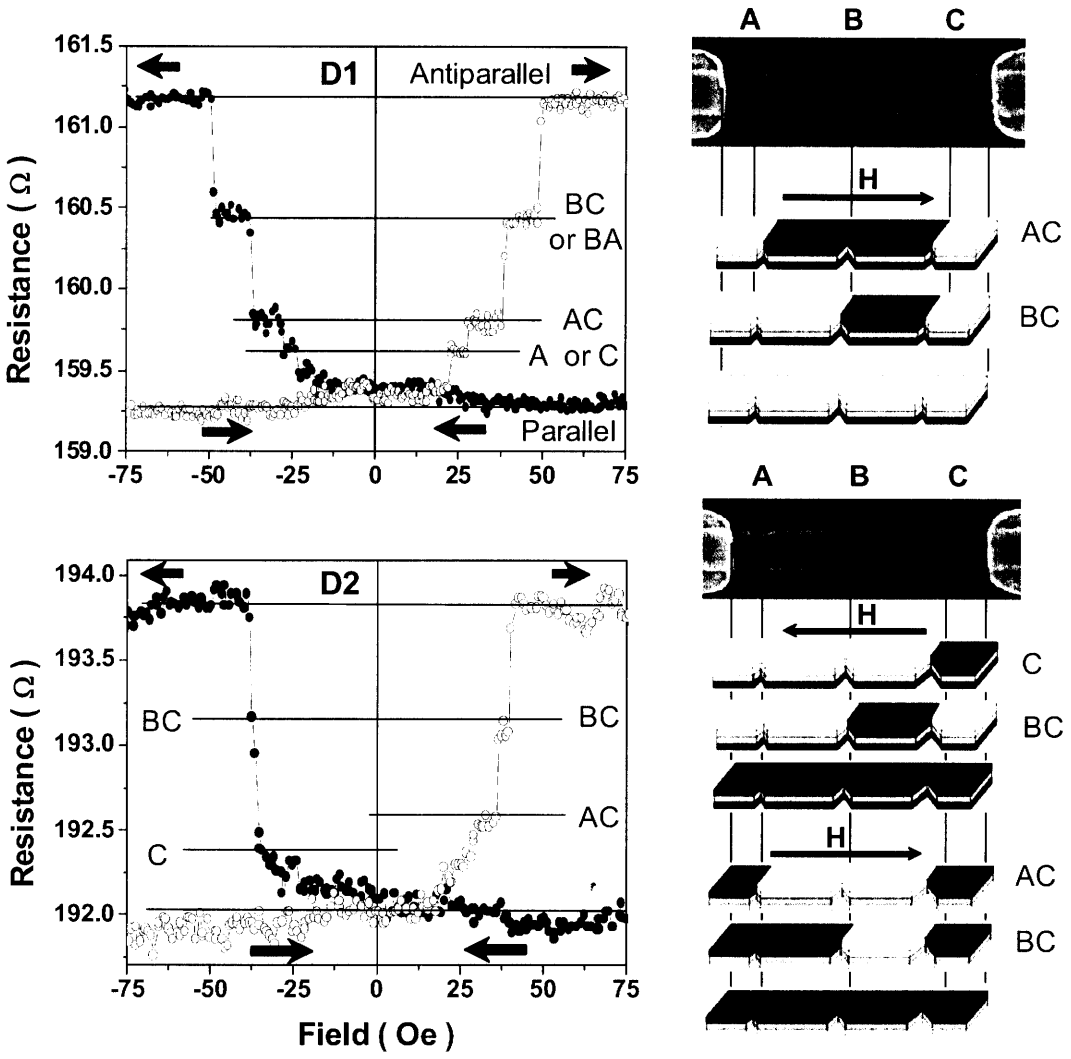

Figure 4.5 Low-field magnetoresistance loops of the symmetric (D1) and asymmetric (D2) PSV bars and the corresponding notches for each intermediate resistance levels. (At right) Corresponding SEMs and schematic representations of the reversal of the soft NiFe layers, depicting the domain configurations as this layer transitions from parallel (lowest resistance) to antiparallel (high resistance) alignment with respect to the magnetization of the hard Co layer.

This analysis unambiguously indicates that the soft layer reversal occurs from both ends of the bars, so that some of the stable intermediate resistance levels correspond to states in which two domain walls are present at different notches of the structures.

For D1, starting from the saturated state where the NiFe and Co layers are magnetized parallel, the first irreversible process at ~ -25 Oe involves the movement of a domain wall to notch A or C, reversing a small section of the bar at the right hand side (state C). At slightly larger fields a second wall forms at notch A, reversing part of the bar at the left (state AC). At -40 Oe one of these two walls moves into the center notch, giving state AB or BC, and finally the NiFe layer reverses completely at -50 Oe to give the antiparallel

state. The reversal sequence is symmetric for both field directions. The intermediate states are stable at remanence, though this is not shown in the figure for clarity. For D2, a less symmetric reversal is found: for negative fields (right-to-left) there is little stability of intermediate states containing domain walls, though states C and BC can be discerned, while for positive fields AC and BC can be identified. We attribute the small plateau at ~ +/-40 Oe to state BC rather than AB, because it is most likely that the wall in notch A will move before the wall in notch C moves.

Reversal of the Co layer shows (Fig. 4.2) few intermediate states. D1 has no stable intermediate states, with abrupt reversal from the antiparallel to the parallel configuration at ~180 Oe. D2 shows a similar abrupt reversal at 150 Oe for positive fields, but for negative fields the Co reverses from the right hand side only up to notch C (the deepest notch) at -150 Oe. Complete reversal only occurs at -200 Oe.

The magnetostatic coupling effect on the reversal of the soft layer is two-fold: first the stray field of the Co on the NiFe adds to the external bias field during the reversal, thus lowering the switching field compared to the single layer uncoupled value, and second, the soft layer would rather reverse from both ends because it is energetically favorable to have two walls close to the extremities of the bar where the stray field lines can be delimited in a flux closure configuration instead of having a single wall in the middle, generating stray field lines distributed all over the length of the bar.

Overall, the results of field-induced reversal deduced from both magnetoresistance measurements and micromagnetic simulations indicate that these notched PSV bars can support a range of non-uniform magnetic configurations containing up to two domain walls and that magnetostatic coupling is omnipresent. The locations of the walls in the notches at remanence or at low bias fields can be controlled by field cycling.

4.4 Current induced switching.

Fig. 4.6 (a) shows the resistance of D1 as a function of the pulse current amplitude and direction (with right-to-left and left-to-right electron flow in the bars being positive and negative, respectively), using bias fields corresponding to an AC domain wall configuration (see Fig. 4.5). The sample was initially saturated at +1000 Oe (or -1000 Oe) and then a bias field of 29.6 Oe was applied in the opposite direction to the saturating field. For each data point, a single current pulse was supplied to the bar followed by a resistance measurement to determine whether any reversal had occurred. This two-step procedure (pulse, resistance measurement) described in section 3.2 was repeated with increasing pulse amplitude for both possible current pulse directions.

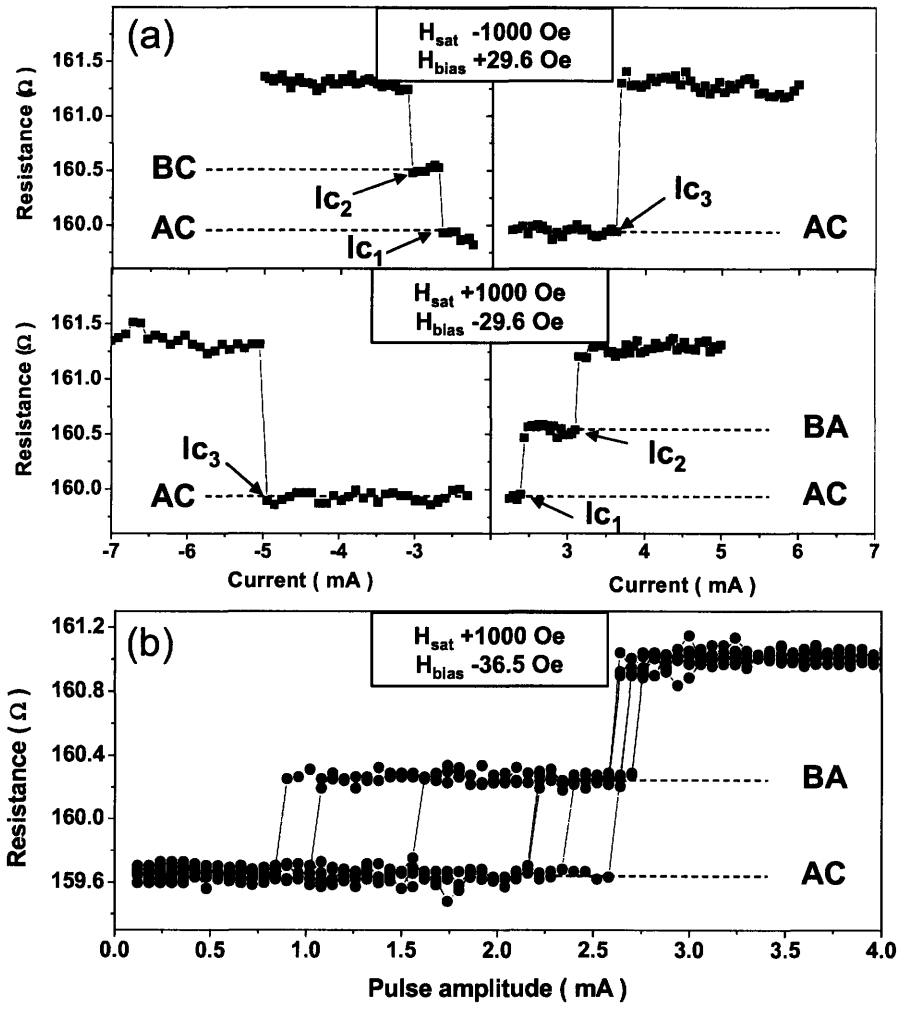

Figure 4.6 (a) Resistance versus pulsed current measurements for D1 for both positive and negative field saturation, $\pm H_{sat}$, and bias fields of ± 29.6 Oe. I_{C1}, I_{C2} and I_{C3} indicate the critical currents for domain wall movement. (b) Consecutive resistance versus pulse-amplitude measurements after positive saturation and applying -36.5 Oe bias.

For a positive bias field and negative current or negative bias field and positive current, two critical currents are observed, labeled I_{C1} and I_{C2}. Based on the resistance values, these represent respectively the partial reversal of the NiFe layer to form the BC or AB configuration (i.e. the movement of one wall into the center notch B), and the complete reversal of the NiFe (i.e. the unpinning of one of the walls and its annihilation with the other). The critical current densities range from 2×10^{11} to 5×10^{11} A/m^2, which are of the same order of magnitude as those previously reported to move a domain wall in the soft layer of a spin-valve wire [11-14]. On the other hand, for a positive bias field and positive current, or negative bias field and negative current, the sample shows a single reversal step (I_{C3}) corresponding to the complete reversal of the NiFe. Even though current induced magnetic switching (CIMS) occurred for both directions of the current flow, the response is asymmetric, for example the two I_{C3} values in Fig. 4.6(a) are 3.5 and 5 mA. This asymmetry contrasts with the symmetric field-induced switching shown by D1.

Successive measurements on the same sample show a switching current distribution. As an example, Fig. 4.6(b) shows ten consecutive measurements for a bias of -36.5 Oe (starting from the AC state). The current I_{C1} required to propagate one of the walls from notch A or C to notch B varied between 0.8 and 2.6 mA, while the current I_{C2} required to depin one of the domain walls to complete the reversal is quite consistent between measurements, varying only between 2.6 and 2.7 mA. A CIMS phase diagram for D1 is shown in Fig. 4.7, for a range of bias fields between 10 – 30 Oe. Error bars indicate the reproducibility of each critical current. This figure shows that as the bias field increases, the critical current required for reversal decreases. In both samples, CIMS could only be obtained in the presence of a bias field.

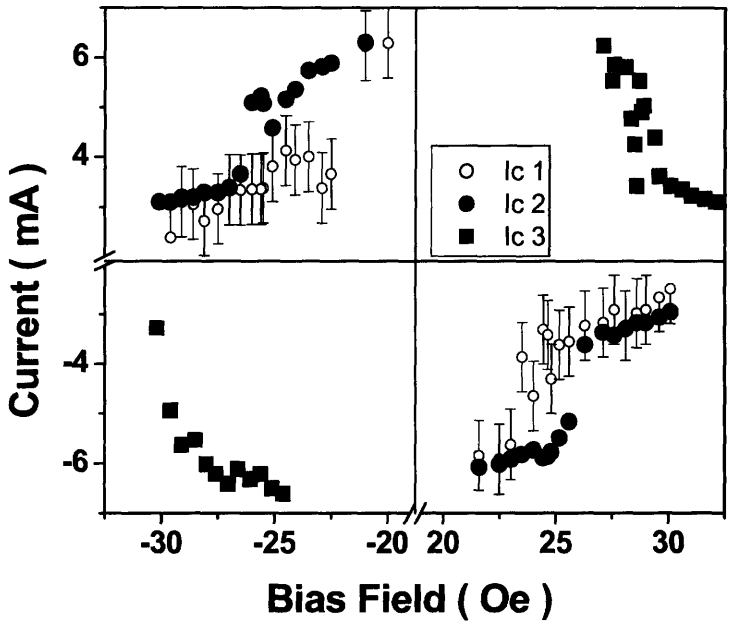

Figure 4.7 CIMS phase diagram showing pulsed current amplitude versus bias field for D1. Open circles, full circles and full squares correspond to critical switching currents I_{C1}, I_{C2} and I_{C3}, respectively. For I_{C2} and I_{C3} the error is within the size of the symbols.

In contrast, CIMS experiments in D2 show a two-step switching response for all current and bias-field quadrants. Figure 4.8a shows the reversal at a bias field of +/- 37.5 Oe, which corresponds to an C or AC domain configuration. Reversing the soft layer from state C or AC into BC required current densities around 1.2×10^{11} A m^{-2}, while complete reversal from a BC configuration to the antiparallel state required higher current densities (up to 2×10^{12} A/m^2). Unlike D1, the variability in critical current was lower for I_{C1} than for I_{C2}. Figure 4.8.b shows a series of ten consecutive CIMS measurements starting from state A, after saturating in +1000 Oe and applying a bias field of -35.2 Oe.

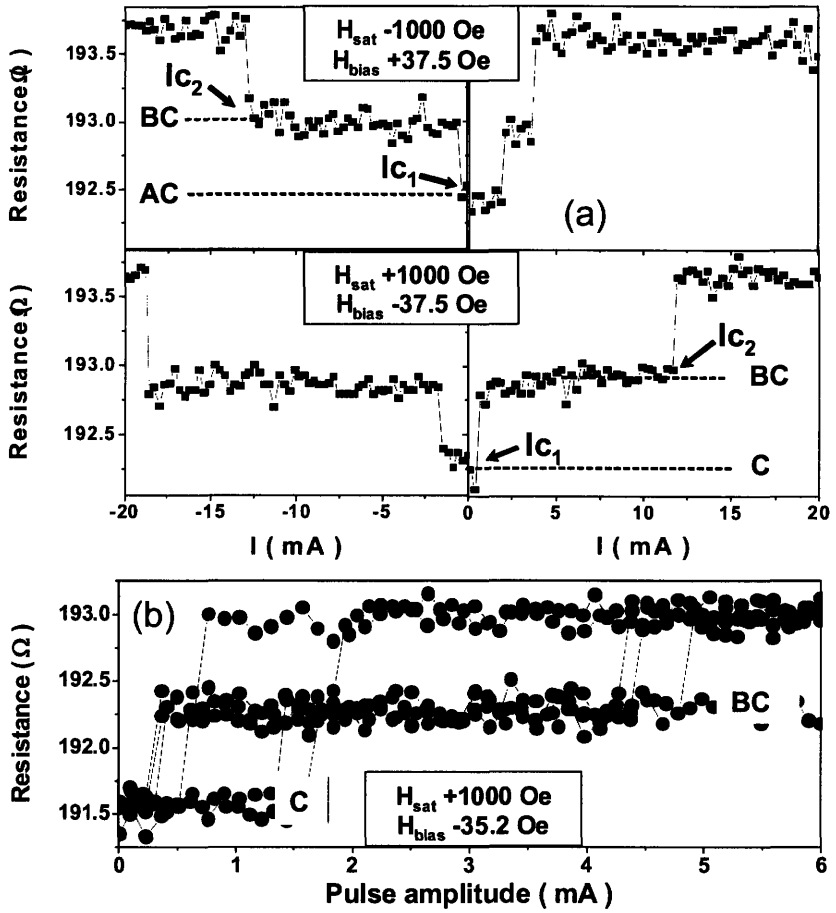

Figure 4.8 Resistance versus pulsed current amplitude measurements for D2 for both positive and negative field saturation, $\pm H_{sat}$ and field bias ±37.5 Oe (AC or A configurations). I_{C1} and I_{C2} indicate the critical currents for domain wall movement in the NiFe layer. Consecutive resistance versus pulsed current measurements shows the reproducibility of the critical currents I_{C1} and I_{C2} for a bias field of -35.2 Oe.

At higher bias fields, ~150 Oe, it was also possible to reverse the magnetization of the Co layers in a single step for both D1 and D2 (Fig. 4.9) using current densities around 1.2 $\times 10^{11}$ A/m^2. For both devices the maximum pulse current amplitude and maximum pulse length used were 30 mA and 100μs, respectively. Higher values for these parameters were not explored because they resulted in a slight increase in the resistance of the PSV bars, even though the switching fields for each transition in the GMR data remained unchanged.

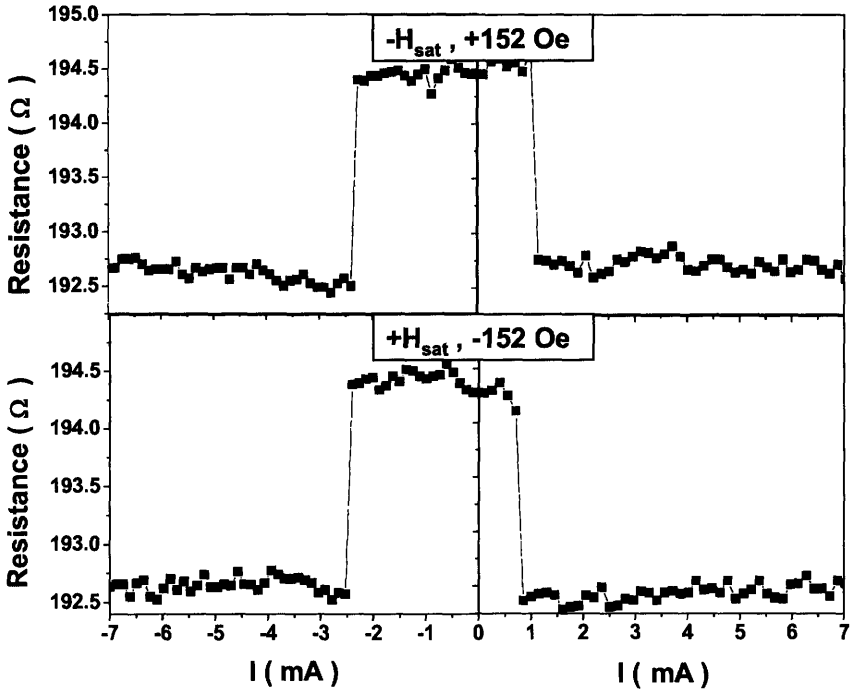

Figure 4.9 Resistance versus pulsed current measurements for D2 for both positive and negative field saturation, ±Hs (1000 Oe), and field bias ±152 Oe directions, showing the reversal of the Co layer.

Figure 4.10 shows how the angle between the axis of the bar and the external applied field can affect both the field-induced GMR data and the variability of the CIMS response. In this experiment the saturation and bias fields are applied at +25° (Fig. 4.10.a) or -25° (Fig. 4.10.b) from the axis of D2. At +25°, the GMR indicates a single step reversal with a variation in the critical current from 0.2 to 1.7 mA (a range of 1.5 mA) for a bias field of 44.9 Oe (corresponding to a domain wall at notch C). However at -25° the GMR data shows that the soft layer at a bias of 38.7 contains an AC configuration which only reverses to a BC configuration within the same current-amplitude range. These results suggest that the response of the soft layer to the transverse component of the field plays an important role in the reversal process.

The CIMS results show that the soft layer in each PSV bar can be reversed for all combinations of pulse current and bias field direction to form the high resistance, antiparallel state. However the lowest bias field for which CIMS was observed after saturation was 5 Oe for both devices. CIMS could not be observed at remanence for any of the possible domain wall configurations in either device. This contrasts with the results on longer bars with a single notch [13] where current-induced reversal could be obtained at zero bias. In our experiment the notches provide relatively strong pinning sites, and the current acting alone is insufficient to unpin the walls. The observations are consistent with reversal dominated by the bias field, in which the current pulse lowers the effective switching field.

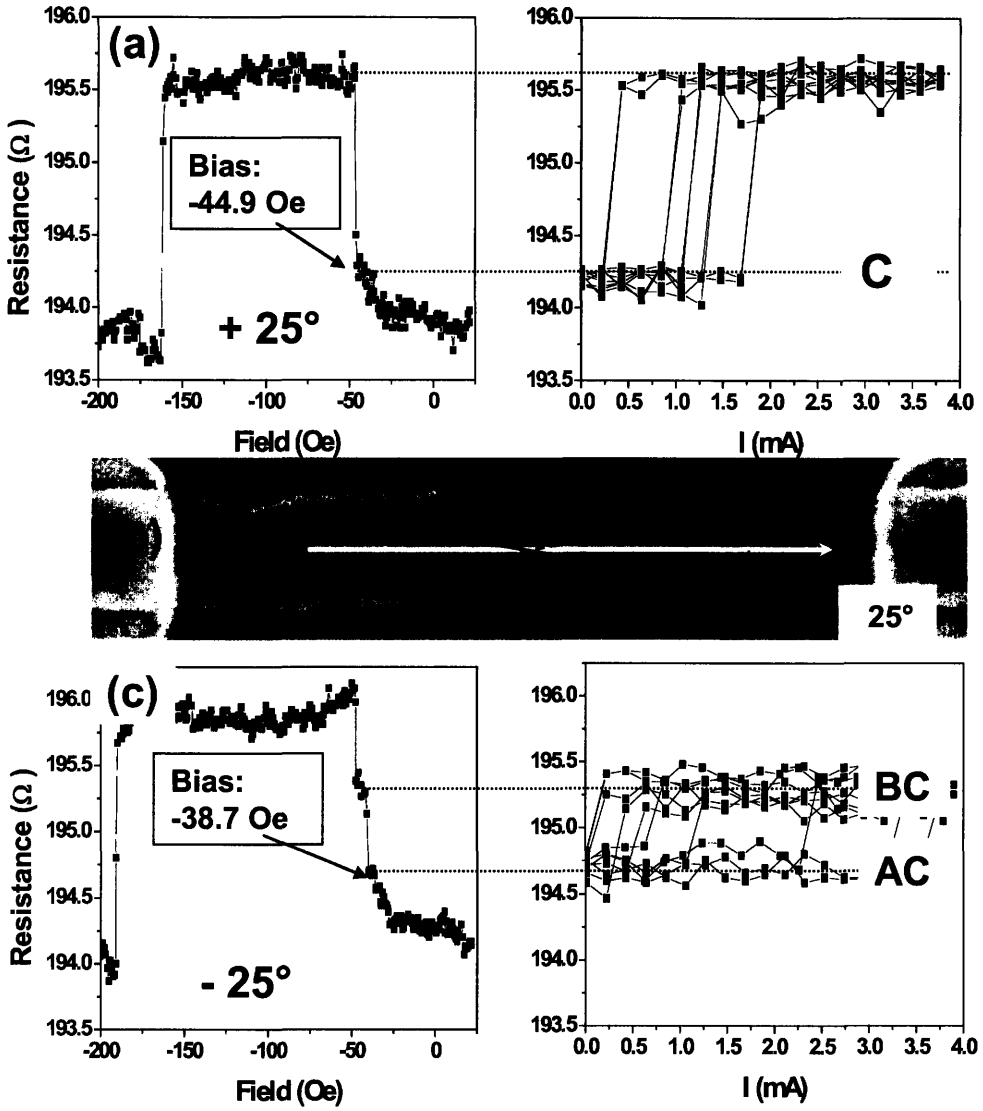

Figure 4.10 (a) GMR measurement at +25 deg (top left) and CIMS measurements in that configuration (top right) with an applied bias of –44.9 Oe. (b) Scanning electron microscopy image of D2 with the field and current highlighted to define the angle used. (c) GMR measurement at – 25 deg with an applied bias of -38.7 Oe.

4.5 Simulations results.

In order to investigate the importance of the Oersted field in the current-induced reversal of these structures, micromagnetic simulations were carried out in which the Oersted field term (see section 2.2.3.2) was included. As thoroughly detailed in section 2.2.3.2, the Oersted field distribution in the NiFe layer was calculated based on the resistivities of the four layers. The resistivity of each metallic layer was measured from single layer films of 6 nm NiFe (87 μΩ cm), 4 nm Cu (90 μΩ cm), 5 nm Co (30.5 μΩ

cm), and 4 nm Au (49 μΩ cm) sputter deposited onto Si (100) wafers with 50 nm-thick thermal oxide. A parallel resistor model predicts a net resistance of the PSV structure of 6 Ω, while the measured resistance was 3.7 Ω, indicating that the mean free path of the electrons exceeds the layer thicknesses. The parallel resistor model predicts a current distribution within each layer of 19.25% in the NiFe, 12.32% in the Cu, 45.62% in the Co, and 22.81% in the Au. (A longer mean free path will make the current distribution more homogeneous.)

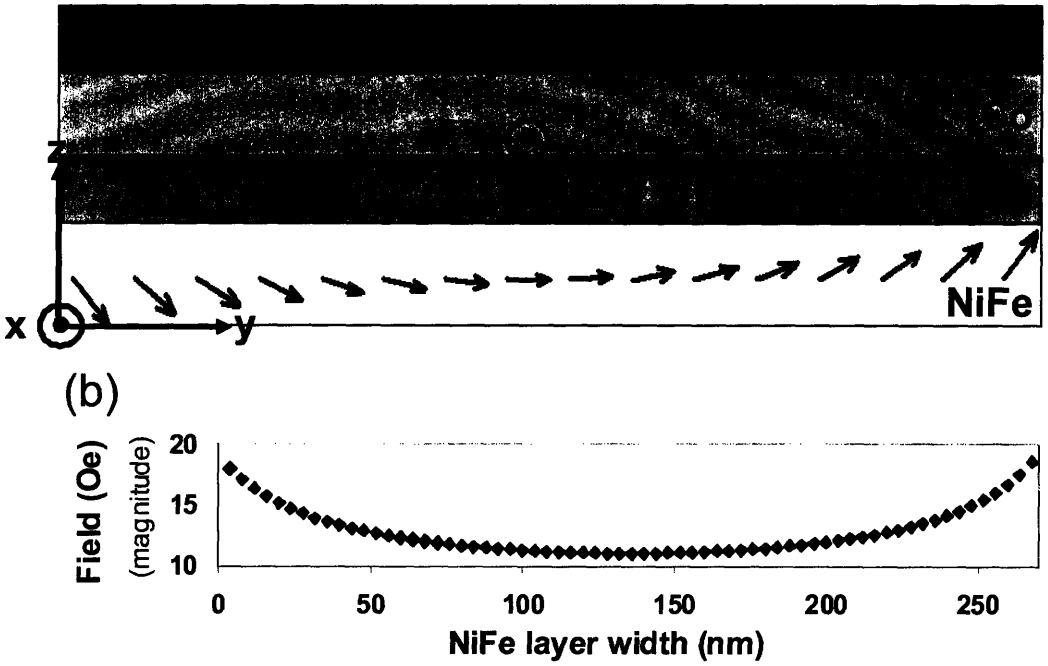

Figure 4.11 (a) Oersted Field distribution in a section at the center of the bar for a positive current density of $5x10^{11}$ A/m^2. The magnitude of the Oersted field along the width of the bar is shown in (b).

Each layer in the bar was then modeled as an array of 1.4 μm long finite wires placed every 1nm in the y and z directions, as depicted in Fig. 4.11. As seen in section 2.2.3.2, the Biot-Savart Law was used to derive the Oersted field distribution in the NiFe layer from the current. The results of the calculation for a cross section at the center of the bar are shown in Fig 4.11 for a current density of 5×10^{11} A/m^2. The field has a non-trivial in-plane component in the y direction, perpendicular to the bar, and its magnitude varies between 10 and 20 Oe (Fig. 4.11.b). This model neglects the effect of the notches, but it is expected that notches will also produce a local component of the Oersted field along the x-direction. The Oersted field in the hard layer was not taken into account since its magnitude added to the bias field remains much smaller than the switching values found in the GMR data.

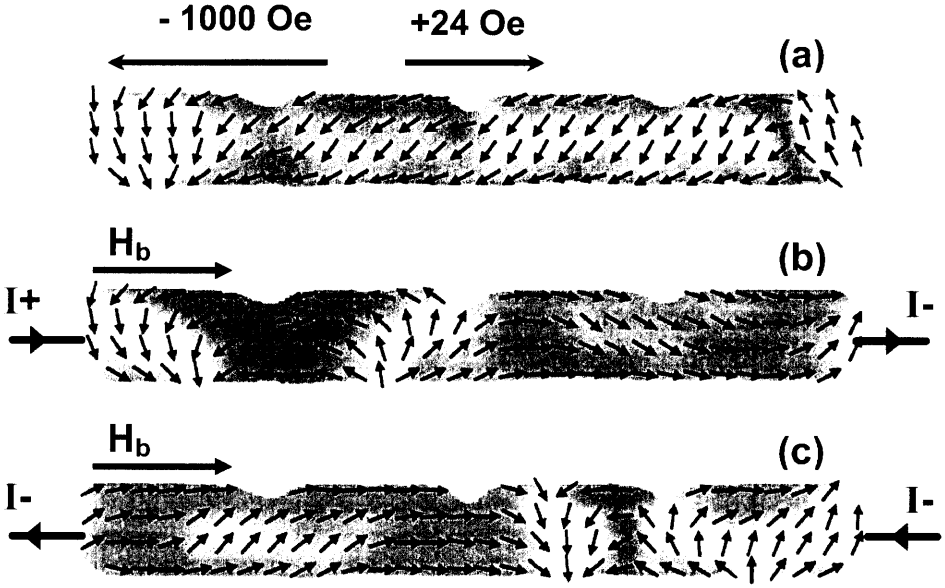

Figure 4.12 Simulation results showing the effect of the Oersted field from the pulsed current on the magnetization state in the soft magnetic layer. (a) The remanent magnetization state after applying a negative saturation field (H_s) and a small positive bias field (H_b). (b) and (c) Minimized energy states after pulsing a current in the positive and negative directions in the presence of a bias field.

The calculated Oersted field distribution was included in the micromagnetic simulations of sample D1. Fig. 4.12.a shows the magnetization state in the NiFe layer after applying a negative saturation field of -1000 Oe followed by a small positive bias field of +24 Oe. For D1, experimentally this bias corresponds to a domain wall at notch A or C, in agreement with the small plateau evident at this field in Fig.3. In the model we see partial reversal near the left end of the bar. Figs. 4.12.b and 4.12.c show the magnetization state after applying a current pulse of density 5×10^{11} A/m^2 for 5 ns [19], and minimizing the energy in the presence of the bias plus Oersted field for positive and negative current directions, respectively. The results show an asymmetric reversal in the soft layer with respect to the direction of the current pulse. Notably, the reversal in each case starts from opposite ends of the bar, and different volumes of the bar have reversed for each current direction. For positive current, domain walls remain near notches A and B, whilst for the negative current direction the NiFe layer is almost completely reversed, with one wall past notch B and another near notch C. For both current directions the NiFe is partly reversed and the resistance would increase, but the details of the reversal differ. These characteristics agree qualitatively with the experimental observations. The simulations indicate that the Oersted field term alone is capable of promoting reversal in the soft magnetic layer in a bias field to achieve a change in GMR, even in the absence of a spin torque effect.

4.6 Summary.

The field- and current-induced reversal of 2.14 μm long, 270 nm wide Co/Cu/NiFe notched bars have been investigated using measurements of giant magnetoresistance combined with 3D micromagnetic modeling. In the major hysteresis loops the soft NiFe layer reversal is initiated from the ends of the bar under the influence of the magnetostatic field from the Co. Several intermediate resistance states may be identified corresponding to the presence of domain walls located at the notches. Domain wall movement can be accomplished in both the soft and hard layers of the PSV using current densities of order 10^{11} A/m^2, in the presence of a biasing magnetic field. The critical current for domain wall movement decreases as the bias field is increased, but in these samples current-induced reversal was not obtained in bias fields below 5 Oe. Reversal of the NiFe layer occurs in either a single step, or in a two-step process depending on the notch configuration and the direction of bias field and current. Current induced magnetization reversal of the Co layer occurs as a single step, for both current and bias field directions.

These small structures show significant magnetostatic interactions between the NiFe and Co layers, and effective pinning of domain walls at the notches. The reversal of the NiFe is driven primarily by the bias field, whilst the Oersted field from the current pulse promotes reversal at bias fields below the switching field. In these small current-in-plane multilayer structures, modeling indicates that the Oersted field from the current pulse is sufficient to promote domain wall depinning in the soft layer, even in the absence of spin torque effects.

The notched bars were first designed to be a first step into understanding CIMS in multilayered structures, the ultimate purpose being to study and try to understand CIMS in multilayered rings, which display interesting magnetic configurations with multiple remanent states and low switching fields, as is detailed in next chapter.

[1] M. Tsoi, R. E. Fontana, S. S. P. Parkin, Appl. Phys. Lett. **83**, 2617 (2003).

[2] M. Kläui, P. –O. Jubert, R. Allenspach, A. Bischof, J. A. C. Bland, G. Faini, U. Rüdiger, C. A. F. Vaz, L. Vila, C. Vouille, Phys. Rev. Lett. **95**, 026601 (2005).

[3] M. Kläui, M. Laufenberg, L. Heyne, D. Backes, U. Rüdiger, C. A. F. Vaz, J. A. C. Bland, L. J. Heyderman, S. Cherifi, A. Locatelli, T. O. Mentes, L. Aballe, Appl. Phys. Lett. **88**, 232507 (2006).

[4] K. Kimura, Y. Otani, K. Tsukagoshi, Y. Aoyagi, J. Appl. Phys. **94**, 7947 (2003).

[5] K. Kimura, Y. Otani, I. Yagi, K. Tsukagoshi, Y. Aoyagi, J. Appl. Phys. **94**, 7266 (2003).

[6] N. Vernier, D. A. Allwood, D. Atkinson, M. D. Cooke, R. P. Cowburn, Europhys. Lett. **65**, 526 (2004).

[7] J. L. Tsai, S. F. Lee, Y. Liou, Y. D. Yao, T. Y. Chen, K. W. Cheng, J. Appl. Phys. **97**, 10C710 (2005).

[8] M. Kläui, C. A. F. Vaz, J. A. C. Bland, W. Wernsdorfer, G. Faini, E. Cambril, L. J. Heyderman, Appl. Phys. Lett. **83**, 105 (2003).

[9] M. Kläui, C. A. F. Vaz, J. A. C. Bland, W. Wernsdorfer, G. Faini, E. Cambril, L. J. Heyderman, F. Nolting, U. Rüdiger, Phys. Rev. Lett. **94**, 106601 (2005).

[10] A Yamaguchi, T. Ono, S. Nasu, K. Miyake, K. Mibu, T. Shinjo, Phys. Rev. Lett. **92**, 077205 (2004).

[11] J. Grollier, D. Lacour, V. Cros, A. Hamzić, A. Vaurès, A. Fert, D. Adam, G. Faini, J. Appl. Phys. **92**, 4825 (2002).

[12] J. Grollier, P. Boulenc, V. Cros, A. Hamzić, A. Vaurès, A. Fert, G. Faini, Appl. Phys. Lett. **83**, 509 (2003).

[13] J. Grollier, P. Boulenc, V. Cros, A. Hamzić, A. Vaurès, A. Fert, G. Faini, J. Appl. Phys. **95**, 6777 (2004).

[14] C. K. Lim, T. Devolder, C. Chappert, J. Grollier, V. Cros, A. Vaurès, A. Fert, G. Faini, Appl. Phys. Lett. **84**, 2820 (2004).

[15] H. W. Fuller and D. L. Sullivan, J. Appl. Phys. **33**, 1063 (1962).

[16] H. D. Chopra, D. X. Yang, P. J. Chen, D. C. Parks and W. F. Egelhoff, Phys. Rev. B **61** (14), 9642 (2000).

[17] F. J. Castaño, D. Morecroft and C.A. Ross, Phys. Rev. B, **74**, 224401 (2006).

[18] G. Tatara and H. Kohno, Phys. Rev. Lett. **92**, 086601 (2004).

[19] K-J. Lee, B. Dieny, Appl. Phys. Lett. **88**, 132506 (2006).

Chapter 5

Comparative study of the field and current induced switching behaviors of Pseudo Spin Valve rings of elliptical and rhomboidal shapes.

5.1 Review on field induced magnetization reversal in rings.

5.2 Devices studied.

5.3 Field Induced reversal. Classical configuration versus Wheatstone bridge.

5.4 Current induced measurements.

5.5 Summary

5.1 Review on field induced magnetization reversal in rings.

Since 2001, extensive work has been conducted on single ferromagnetic layer [1-8] rings, but it is only recently (2005) that interest has been focused on the behavior of multilayered PSV [9-13] rings. The first studies on single layer rings have allowed the authors to identify new magnetization states different from the vortex states (either clockwise or anti-clockwise) obtained classically in macroscopic magnetic rings: besides the already known vortex flux-closure states (Fig 5.1.e), a state containing two 180° domain walls and known as the onion state has been identified (Fig 5.1.b and Fig 5.1.f). A metastable state has also been identified: the twisted state which is a vortex state containing a metastable 360° domain wall as seen in Fig. 5.1.c and Fig 5.1.d.

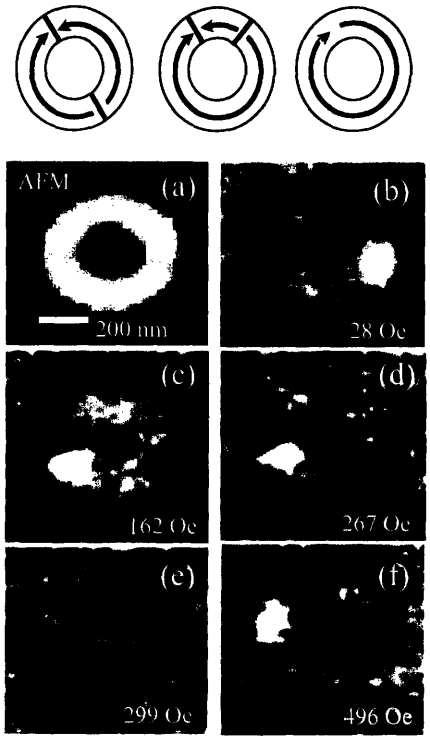

Figure 5.1 At the top, a schematic of the onion, twisted and vortex states in a ring. Below data for a 520 nm diameter ring: (a) an atomic force micrograph. (b)-(f) a sequence of magnetic force microscopy (MFM) images measured at remanence after first saturating the sample at 10 000 Oe then applying a reverse field of (b) 28 Oe, (c) 162 Oe, (d) 267 Oe, (e) 299 Oe and (f) 496 Oe. After Ref [5].

In elliptical single layer rings, shape anisotropy defines the long axis as the easy axis, which shows different stabilities of onion, vortex and twisted states compared to when the field is applied along the short (hard) axis [6].

Electrical transport properties have been investigated in single layer NiFe rings with diameters in the micron range and widths of 100 nm or above [14-18]. The AMR (see

section 2.2.2.2) is at its high level when the ring is in a vortex state, since everywhere the magnetization is parallel to the current, and transitions between vortex and onion states generate relative AMR changes around 0.1% at room temperature [15].

A more complex picture arises in multilayered magnetic rings in which direct observation through such techniques as MFM remains a challenge. But GMR response can, along with micromagnetic simulations in a similar fashion as used in the previous chapter, give precise insights on the field induced reversal of such structures. Magnetostatic coupling between the two ferromagnetic layers is shown to have a very important role [13].

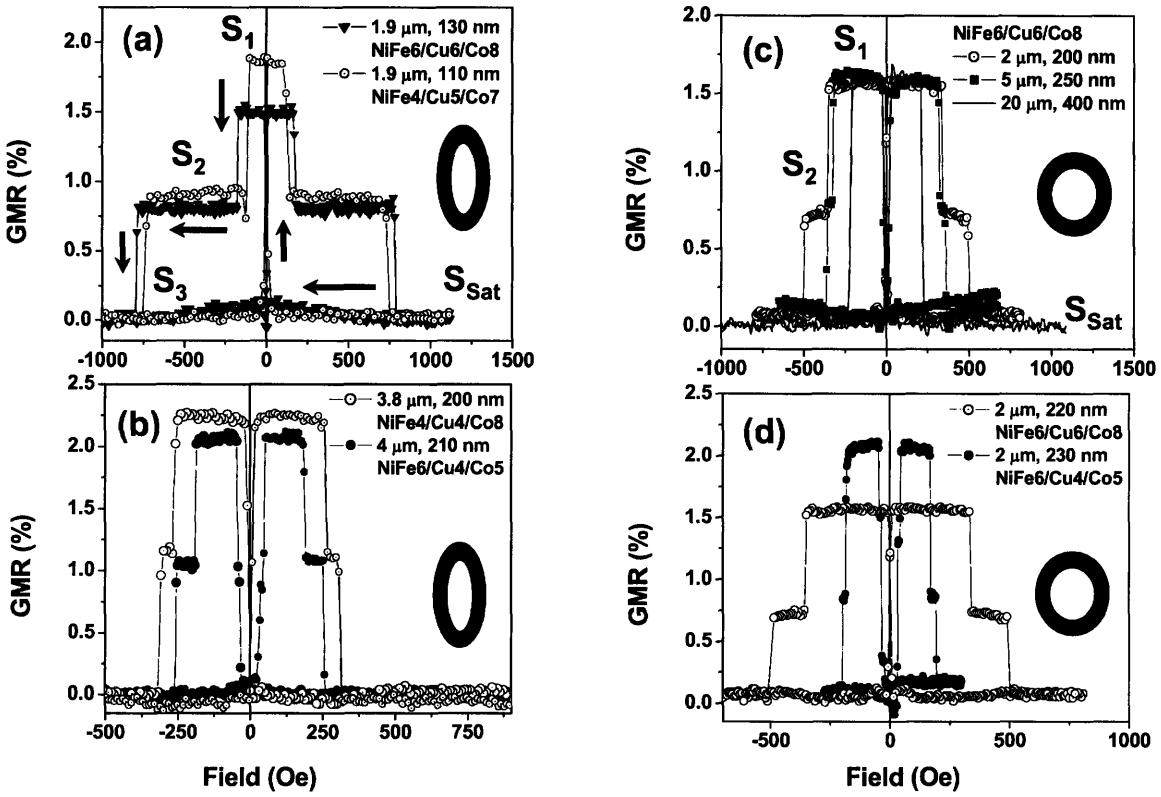

Figure 5.2 Major magnetoresistance loops corresponding to elliptical (a) (b) and circular (c) (d) pseudo-spin-valve rings with different dimensions and NiFe/Cu/Co/Au stacks. The legends give the ring diameter, width and layer thicknesses. After Ref [13].

In this work, F.J. Castaño et al. investigated the GMR response of rings both circular and elliptical made of patterned PSV stacks of NiFe/Cu/Co/Au defined using fabrication steps identical to those described in chapter 3. These rings were defined using 18 nm spaced single pixel lines. A range of thicknesses for each layer as well as a range of length of long and short axes and a range of widths were investigated. The authors demonstrated profoundly different magnetization reversals of the soft NiFe layer depending on whether the hard Co layer was in a vortex state or in an onion state. For every device investigated, the complete reversal from a state where both layers are in a forward onion state at high positive field (S_{sat} in Fig. 5.2.a) to the state where both layers are in reverse onion state at high negative field (S_3 in Fig 5.2.a) comprised two distinctive

intermediate states stable over field ranges that depended on the dimensions of the device.

The first one was the antiparallel state (S_1 in Fig 5.2.a) in which the NiFe layer is in a reverse onion state whereas the Co remains in a forward onion state, thus leading to the highest resistance level. The second was labeled S_2 (Fig 5.2.a) and corresponds to a state in which the Co was in a vortex state and the NiFe in a reverse onion state, thus leading to a resistance level halfway between the low resistance states S_{sat} or S_3 and the high resistance state S_1 (in the contact geometry used there). It was found (Fig. 5.2.c) that decreasing the diameter and the width resulted in an increase in the switching fields. In previous work [9], the switching fields of the hard Co layer from S_1 to S_2 and S_2 to S_3 were shown to depend on the spacer Cu thickness as well as on the soft layer NiFe thickness unlike single layer Co rings whose switching fields depended solely on the geometry of the ring and its thickness [19]. Moreover, the Co vortex state, which disappears in Co single layer rings with thicknesses under 8nm [19], was proved to be stable even for rings with the thinnest Co layer (5 nm) (Fig 5.2.b and 5.2.d). The vortex state was also stable over a larger field range in elliptical rings with the field applied along their easy axis compared to circular rings. Micromagnetic simulations as described in section 3.2.3 corroborate the above description of the magnetization reversal.

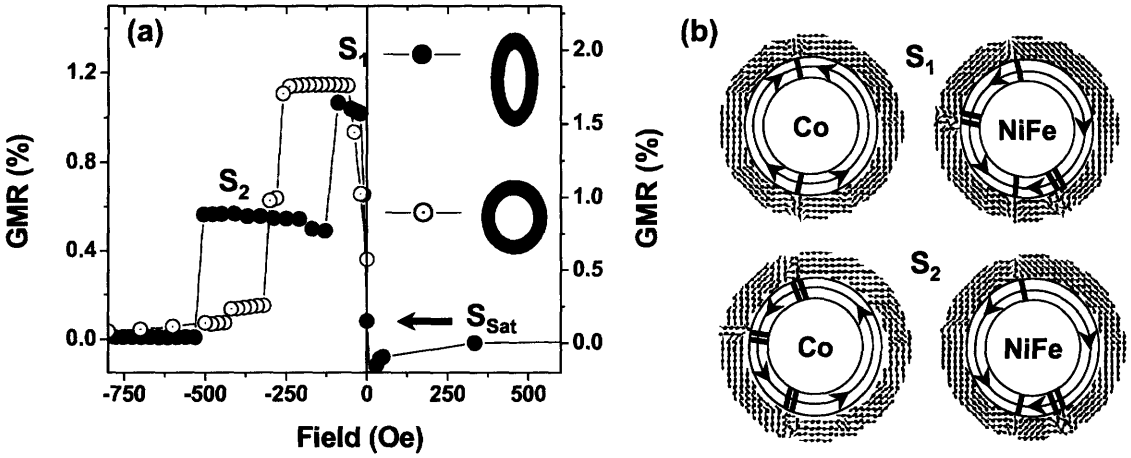

Figure 5.3 (a) Computed GMR curves for elliptical and circular rings. (b) Micromagnetic snapshots of both Co and NiFe layer in S_1 and S_2 states for the circular ring. The small arrows give the precise magnetization distribution and the schematics the overall domain structure. After Ref [13].

The modeling results (Fig 5.3) were in good agreement with the experimental data and suggested that the soft layer reverses through the nucleation at both ends of the ring, along the easy axis, of reverse domains and their propagation along each branch to form a reverse onion state which can have 360° domain walls on both sides (Fig 5.3.b top right). As the field increases further, these 360° domain walls collapse (as seen in Fig. 5.3.b bottom right where only one 360° wall remains). The Co ring transition into a vortex state is also influenced by the magnetostatic coupling between Co and NiFe, more precisely by the stray field from the domain walls present in the NiFe layer. The Co vortex state could also contain several 360° domain walls (Fig 5.3.b bottom left).

To further explore the effects of the magnetostatic coupling between the NiFe and Co ferromagnetic layers, two types of minor loops were both measured and simulated. In the first type, the Co remains in a forward onion state throughout the measurement and the soft layer is cycled back and forth. In the second type of minor loops, the Co is set in its vortex state, and the soft layer is also cycled from forward to reverse onion state and back.

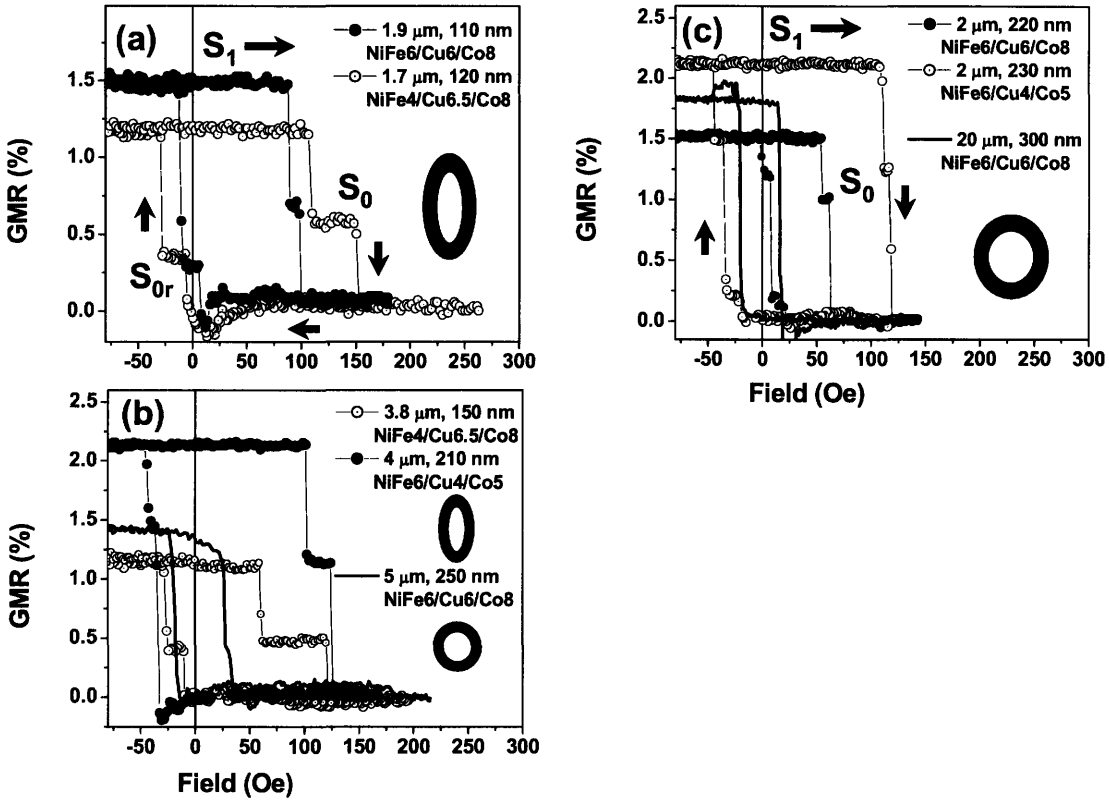

Figure 5.4 Minor GMR loops with the Co in a forward onion state for different geometries and stacks.

For the minor loops with the Co in a forward onion state (Fig. 5.4), additional resistance plateaus were observed and named S_0 and S_{0R}. Interestingly, the minor loops were offset with respect to zero field (Fig. 5.4). This offset may be ascribed to "the escape field needed, for example, for a head to head domain wall in the NiFe layer to unpin or dissociate from the stray field of a tail to tail wall in the Co" (S_1 to S_0 transition). Micromagnetic simulations were again in excellent agreement (Fig 5.5.a) with the measurements, suggesting that S_0 corresponds to the NiFe layer in a vortex state with two 360° domain walls as depicted in Fig 5.5.b and that S_{0R} is an intermediate state in which the reverse domains have already nucleated. Furthermore the transition from S_{0R} to S_1 is made clear: due to the presence of domain walls in the cobalt layer, reverse domains nucleate at both ends, propagate (state S_{0R}) and meet in each branch, thus forming the two 360° domain walls observed (state S_1). These results show the importance of the magnetostatic coupling between each layer through the stray fields around their domain walls.

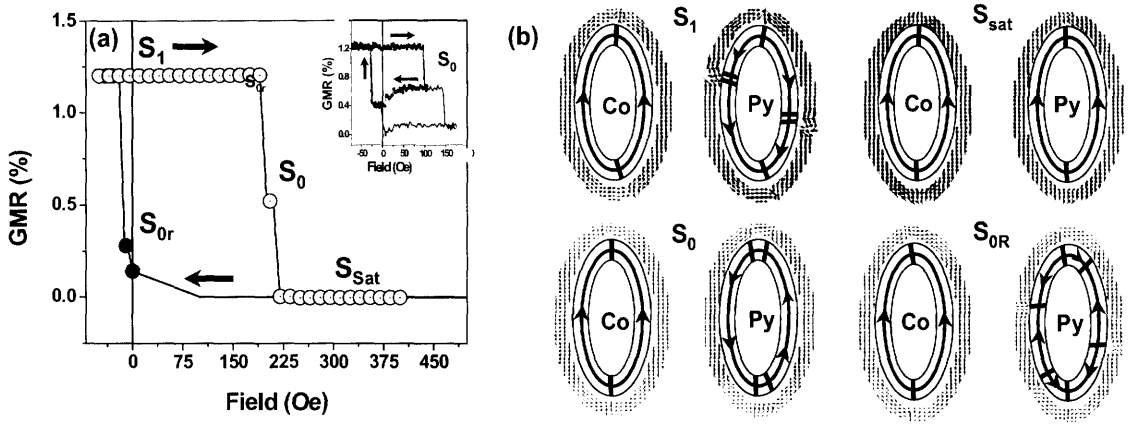

Figure 5.5 (a) Computed minor loop for an elliptical ring. The inset shows experimental minor loop for a 1.7 μm long 120 nm wide NiFe4/Cu6.5/Co8 elliptical ring showing the reversibility of the S_0 and S_{0R} configurations. (b) Micromagnetic snapshots of both Co and NiFe layer in the S_1 S_0 S_{sat} and S_0 states. After Ref [13].

When the hard layer is in a vortex state S_2, if no 360° wall is present, then its stray field should be zero, and the NiFe reversal should be more like a single layer reversal, and no offset should be seen when the soft layer is switching from forward onion to reverse onion and back. Experimental data (Fig 5.6.a) first show that the state S_2 is stable at remanence (same resistance level) which is a first confirmation that the Co layer has very little stray field, thus not influencing the reversal of NiFe. Furthermore, as seen in Fig 5.6.b, the minor loops are very symmetric with respect to zero field, which is, as aforementioned, an indication that no stray field from the Co is influencing the reversal of the NiFe. On cycling the NiFe, while the Co remains in a vortex state, resistance levels of the same level as S_{sat} and S_1 are reached (Fig 5.6.b), which means that the layers are at those fields completely parallel or antiparallel respectively. This can only occur if the NiFe is in a vortex state of same or opposite chirality respectively. The NiFe is stable in the vortex states over a considerable field range, which is different from the major loops where no vortex state in the NiFe was observed with the field step used (~ 1 Oe). Starting from state S_2 and reversing the field, the NiFe switched from its reverse onion state into a vortex state whose chirality depended on the ring itself and the saturation fields used [13], leading to either a parallel vortex state (low resistance level) labeled S_{PaV} or an antiparallel vortex state (high resistance level) labeled S_{ApV}. When increasing further the field, the NiFe switches into a forward onion state, thus leading to a resistance level very close to S_2, labeled S_{2R}. The difference in resistance between S_2 and S_{2R} was attributed to a difference in their domain wall configurations such as 360° walls. Micromagnetic simulations (Fig 5.6.c and Fig 5.6.d) again confirmed the experimental measurements.

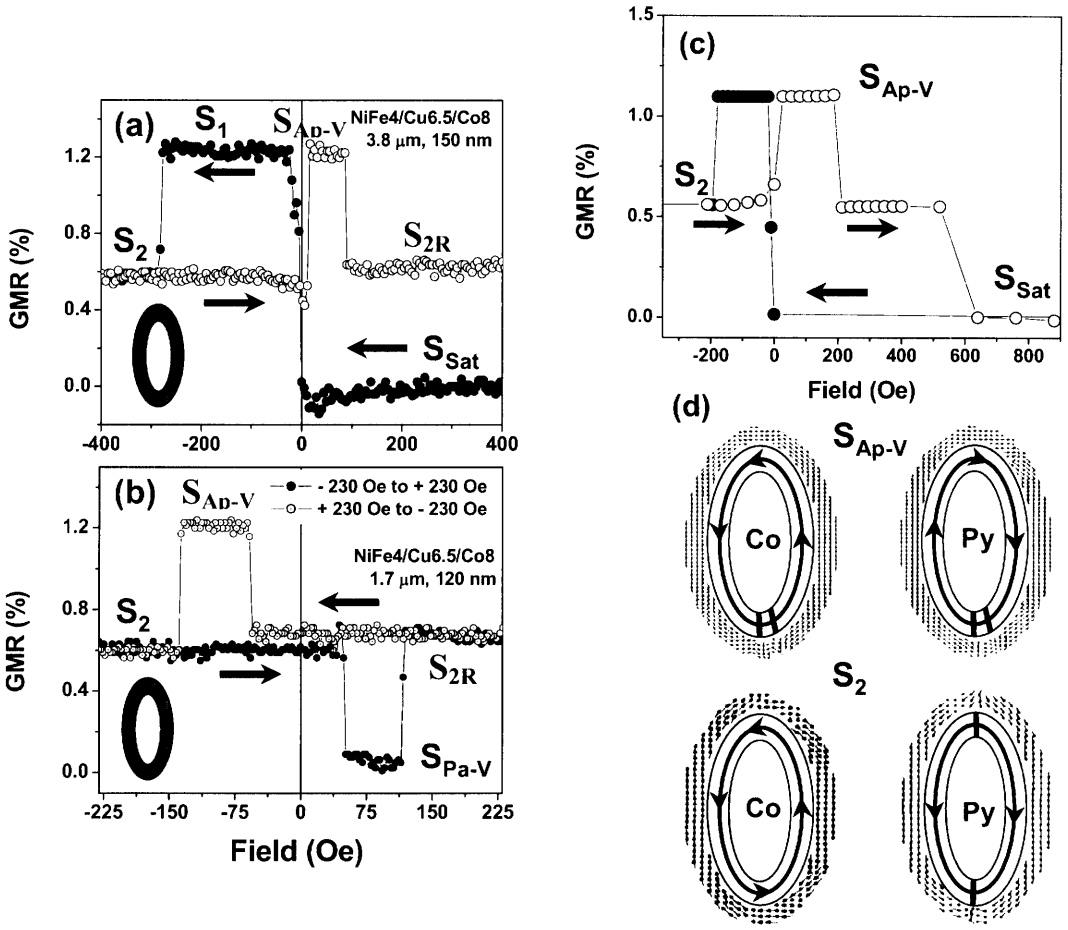

Figure 5.6 (a) Minor loop with the applied field cycled from positive saturation to the S_1 state and then the S_2 state and cycled back from there into the state S_{ApV} and then state S_{2R}. (b) Minor loop for a different elliptical ring after positive saturation with the return branch. (c) Computed minor loop for a 2 μm long 120 nm wide NiFe4/Cu4/Co8 elliptical ring with same field sequence as in (a). (d) Micromagnetic snapshots of both Co and NiFe layer in the S_2 and S_{Ap-V} states. After Ref [13].

This detailed work provides a thorough understanding of the field induced magnetization reversals of PSV patterned elliptical rings and its strong correlation with magnetostatic coupling. Further work has been done on these devices [9-12] to investigate the angular dependence of their giant magnetoresistance response with different contact configurations (in the four point probe measurement technique). The deep understanding of field induced magnetization reversal in elliptical PSV rings is crucial to this work in which the field and current induced behavior of elliptical rings is compared to that of rhomboidal rings and in which a new contact configuration is proposed.

5.2 Devices studied.

Scanning electron micrographs (SEMs) of the two types of device characterized in this work are shown in Fig. 5.7. The elliptical ring (Fig. 5.7.a) had a 4 μm-long easy axis, 2 μm-long hard axis and a 210 nm width, and its evaporated PSV stack was NiFe (6 nm)/ Cu (4 nm)/Co (5 nm)/ Au (4 nm). The DC triode sputtered final contacts were Ta (2 nm)/ Cu (120 nm) and the outer contacts Ti (5 nm)/ Au (25 nm). The rhomboidal ring (Fig. 5.7.b) had a 1.6 μm-long easy axis, a 900 nm-long hard axis and a width of 140 nm, while its triode-DC-sputtered PSV stack was NiFe (6 nm)/ Cu (4 nm)/Co (4 nm)/ Au (4 nm). The DC triode sputtered final contacts are Ta (2 nm)/ Cu (110 nm)/Au (10 nm) and the outer contacts Ti (5 nm)/ Au (30 nm). For both devices, the fabrication procedure for the three different stacks was discribed in section 3.1. As can be inferred from Fig. 5.7, there is a number of different ways to set the four point probe resistance measurement described in section 3.2.1.

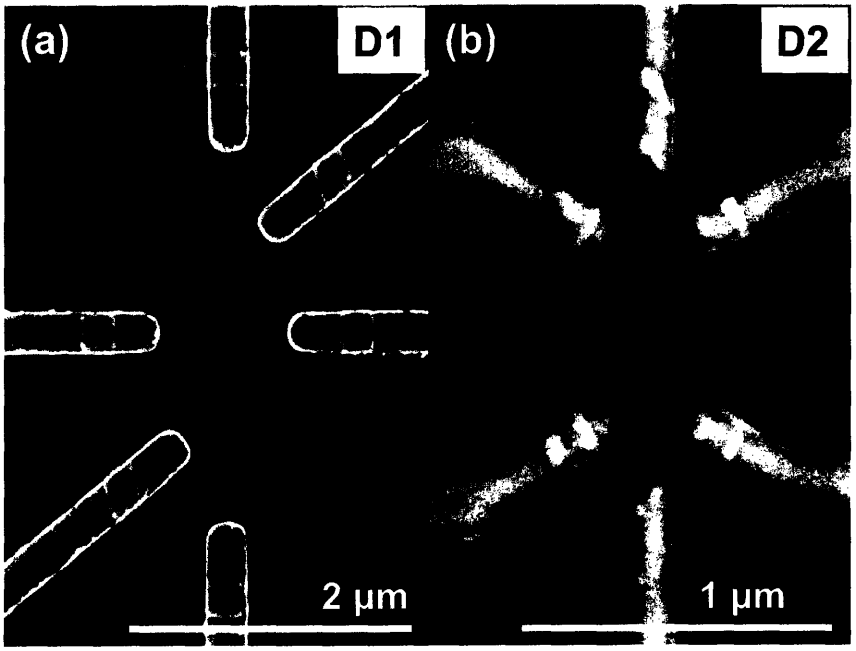

Figure 5.7 Scanning electron micrographs of (a) the elliptical ring (D1) and (b) the rhomboidal ring (D2).

5.3 Field induced reversal. Classical versus Wheatstone bridge contact configurations.

In previous work on rings [9-13], the four point probe measurement were always set in a similar fashion: the voltage drop was measured between two contacts placed between the two current contacts. However a ring-shaped device possessing at least one axis of symmetry can be connected in a symmetric Wheatstone bridge contact configuration: the current leads are set opposite to one another in such a fashion that they define a virtual axis cutting the ring into two parts of equal length, and the voltage leads are placed at equal distances from each current lead. An example of such a contact configuration is shown in Fig. 5.8.a. The two types of leads are therefore crossed. If the resistance of the rings depended solely on its dimensions and material parameters and not on the magnetic field, a perfectly symmetric Wheatstone bridge configuration should yield a zero resistance, as can be deduced from Fig. 5.8: **R1** and **R2** would be equal, as well as **R3**+**R5** and **R4**+**R6**. Therefore the current **I** would split into two equal parts $\mathbf{i}_1=\mathbf{i}_2=\mathbf{I}/2$, and the voltage would then read $\mathbf{R1}.\mathbf{i}_1-\mathbf{R1}.\mathbf{i}_2=0$.

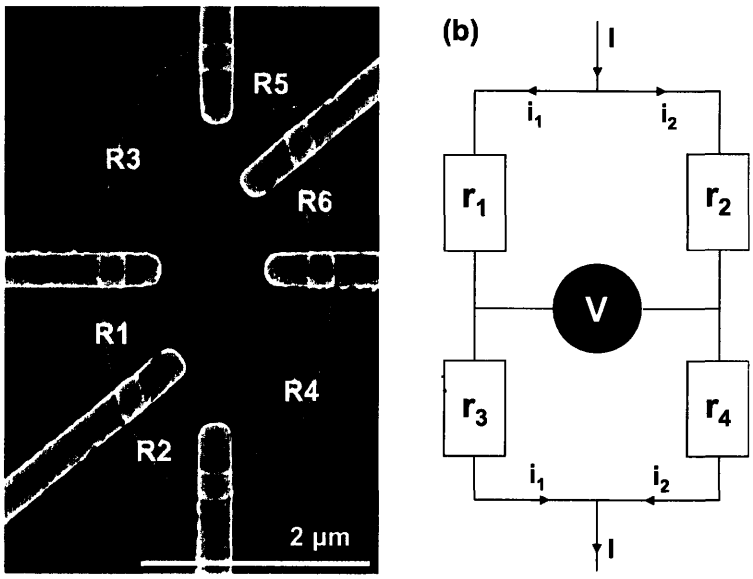

Figure 5.8 (a) Scanning electron micrograph of D1 in a specific symmetric Wheatstone bridge configuration with the corresponding electrical circuit schematics (b), where r_1=R1, r_2=R2, r_3=R3+R5 and r_4=R4+R6. The dashed line in (a) represents the virtual axis created by the two current leads.

However, since the resistance does depend on the relative magnetization state of each layer, the resistance read (defined by V=RI) will be changing with the external applied field. The resistance will read,

$$R_{WB} = \frac{\left|r_1 r_4 - r_2 r_3\right|}{r_1 + r_3 + r_2 + r_4} \tag{5.1}$$

where each resistance is a function of the magnetization state of the ring and the absolute value is due to the lock-in detection which is set to cancel the phase shift between the current input and the voltage output. The measurement is therefore the difference of the resistances cross-products. The general idea prompting the use of such contact configurations is that the measured resistance being a difference of resistances (eqn. 5.1), it can reach a minimum close to zero Ohm, thus leading to potentially very large effective GMR ratios, which are defined for simplicity as:

$$r_{GMR}(\vec{H}) = \frac{R(\vec{H}) - R_{\min}}{R_{\min}} \tag{5.2}$$

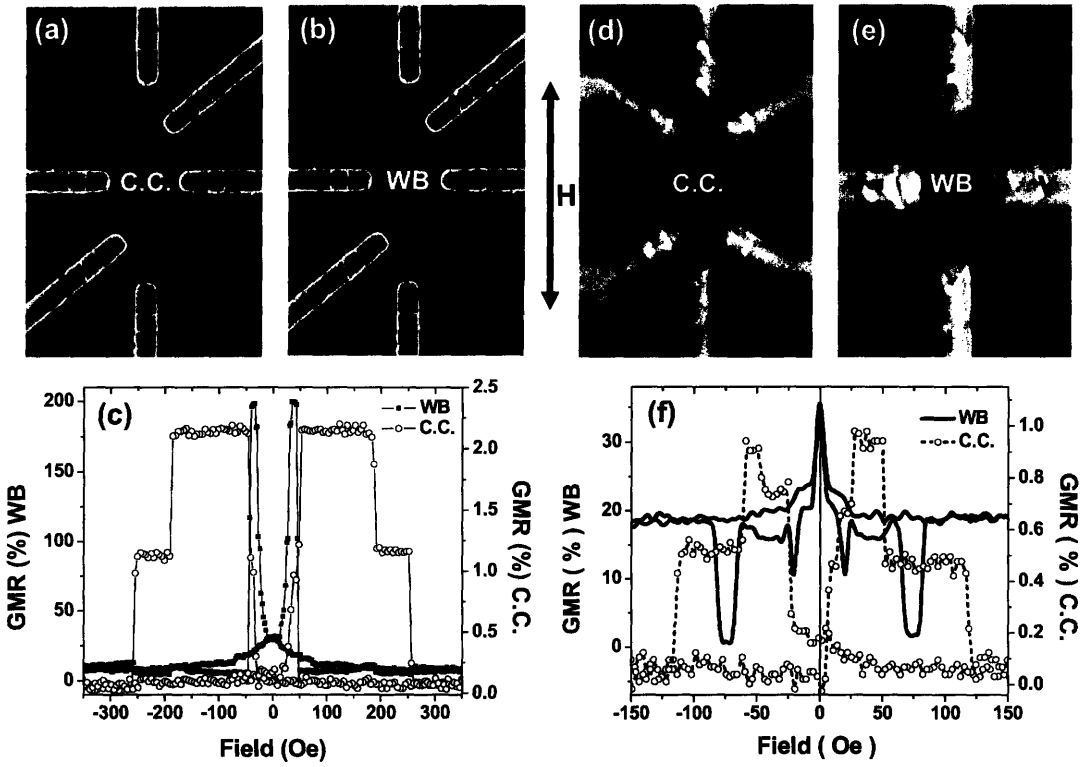

Figure 5.9 Scanning electron micrographs of D1 and D2 in a classical configuration (C.C.) (respectively (a) and (d)) or in a Wheatstone bridge (WB) configuration (respectively (b) and (e)) with the corresponding GMR responses (respectively (c) and (f)). The field is applied along the easy axis.

This expectation is confirmed in both devices studied, where effective GMR ratios reach values as high as 200% (Fig 5.9.c). Figure 5.9 shows the GMR response curves of D1 and D2 when applying the field along their easy axis, and both classical and Wheatstone bridge contact configurations are plotted. For clarity, no distinctions are made between the two different devices shown in Fig 5.9.d and Fig 5.9.e since they differ only by their contact configurations. It should first be noted that the major loop of D1 in the classical configuration (Fig 5.9.c) is consistent with previous work discussed earlier (Fig. 5.2). Furthermore, the GMR response of D1 in the Wheatstone bridge (WB) configuration shows one very high narrow peak that corresponds to the reversing of the soft NiFe layer, while for the remainder of the field range, the GMR is very low. This provides

experimental evidence for the soft layer reversal mechanism being profoundly different to that of the hard layer, as suggested by previous micromagnetic modeling [13]. Since equation 5.1 implies that any change in resistance can only be attributed to an asymmetric magnetization configuration, the peak corresponds to the asymmetric propagation of the reverse domains in the NiFe, in agreement with the previous micromagnetic simulations (state S_{0R} Fig 5.5.b). Additionally, the absolute noise is decreased when going from the classical configuration (C.C.) to the WB: ~0.01 Ω for WB and ~0.03 Ω for C.C.. But since the base resistance is ~0.56 Ω for WB and ~37.76 Ω for C.C., and since for both configurations, the maximum resistance change is ~1 Ω, the relative noise (the inverse of the signal to noise ratio) in resistance is 1% for WB and 3% for C.C., the relative noise in GMR is 0.5% for WB and 2.4% for C.C. The signal to noise ratio is therefore lower for the WB configuration, which is an important parameter for application in devices.

Fig 5.9.f shows the GMR response of the rhomboidal ring D2 to an easy axis field. Interestingly, the classical configuration yields a response very similar to that of the elliptical ring: upon saturation (high negative field), both layers are parallel and the resistance is at its lowest, the state is labeled S_{sat} (Fig 5.10.a). When reversing the field, a first increase in GMR is observed, leading eventually (~25 Oe) to the highest resistance level corresponding to a state S_1 where both layers are antiparallel. Increasing further the field (~50 Oe) leads to an intermediate resistance plateau (state S_2) halfway between S_1 and S_{sat} which corresponds to an intermediate reversal of the Co. Finally, at higher fields (~120 Oe), the hard layer switches to give a parallel state S_3 with the lowest resistance level. The main switching fields are lower than those for an elliptical ring of similar dimensions and stack.

Unlike the C.C. curves, the WB response for D2 (Fig. 5.9.f) is very different from D1. First, the resistance is not at its lowest point when the ring is saturated. There are two likely reasons for this. The first is that the ohmic contact between the rings and the final contacts are not as good as they are in D1 because the rings were deposited using a very conformal method (DC-triode sputtering) which left spikes on the edges (see section 3.1.2), and when the final contacts are deposited on top, those spikes prevent a good ohmic contact (Fig. 5.7.b, the spikes are visible underneath the contacts). Second, a WB configuration is extremely sensitive to any unwanted additional impedance (a bad ohmic contact could be thought of as a capacitor). The resistance in equation 5.1 would be offset, and as is the case for D2, the absolute value is no longer necessary if the offset is bigger than the resistance change, thus allowing a resistance lower than the resistance at saturation. Another explanation could come from an asymmetric contact distribution, but it is likely to be extremely marginal in our sample (see Fig 5.9.e). This issue is neglected in the C.C. since the measured resistance is not a difference. An additional difference between the two rings in their WB configuration is that for D2, in the intermediate state S_2, the reversal of the Co does not occur symmetrically (since we have a peak in the WB GMR), and this indicates that in the rhomboidal rings, the Co layer reverses in a different fashion than in an elliptical ring and most likely do not display any vortex state. The micromagnetic simulations results, shown in Fig. 5.10.b confirm that interpretation: if on the one hand the NiFe layer reverses in a similar fashion than in the elliptical rings by the nucleation and propagation of reverse domains from both ends of the easy axis (Fig 5.10.b S_i), however on the other hand, in the Co layer, reverse domains nucleate in an asymmetric fashion along the sides of the rhomboid (Fig 5.10.b S_2). Furthermore, the WB

response (Fig. 5.9.f) also shows that, close to remanence, the rhomboidal ring is already reversing in an asymmetric way, which is confirmed by the simulation Fig 5.10.b, where S_{sat} shows the simulation result after a high negative saturation (-3000 Oe) and then a field lowered to -50 Oe. The simulation shows the strong magnetostatic coupling between both walls in each layer prompting an arrangement more than 45° apart in order to close the flux lines more easily. Finally, the micromagnetic simulations show that 360° walls are very stable in those rhomboidal rings (Fig. 5.10.b S_3), and unlike in the elliptical rings [13], they do not collapse easily, an interesting feature which will be further detailed later.

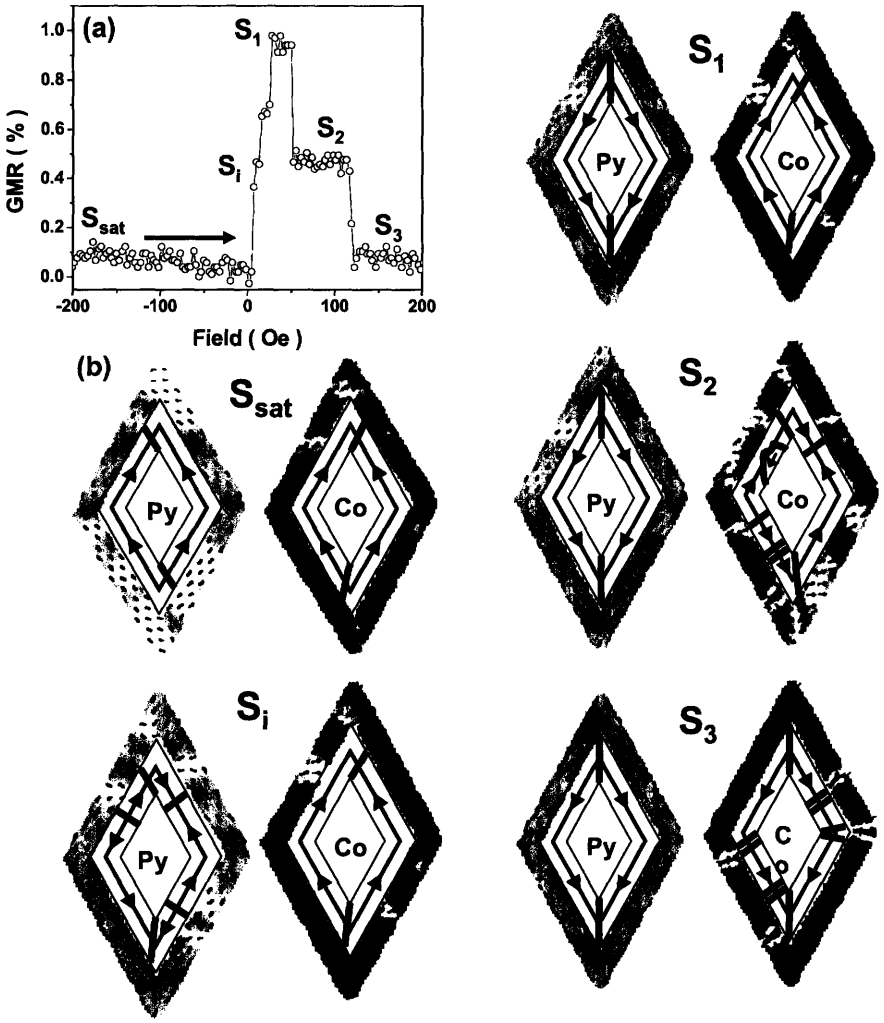

Figure 5.10: (a) A single GMR curve of D2 in C.C. (b) Micromagnetic snapshots of both Co and NiFe layer in the S_{sat}, S_i, S_1, S_2, and S_3 states for the rhomboidal ring. The small arrows give the precise magnetization distribution and the schematics the overall domain structure.

In order to further study the similarities between both structures, minor loops with the cobalt in a forward onion state were measured for both D1 and D2 as seen in Fig 5.11. The similarities are quite obvious, and both display intermediate states (S_0 and S_{0R} after the notations used in [13]) during the NiFe reversals. However, if S_{0R} is usually stable

over a much lower field range than S_0 in elliptical rings, in D2, both display a large stability. A last very interesting feature evident from the data depicted in Fig. 5.11 is the measured escape field, defined in section 4.3. Both display an escape field, which is a indisputable evidence of magnetostatic coupling between both ferromagnetic layers. Eventhough the rhomboidal ring was smaller and narrower than the elliptical ring, the shifts in these minor loops are smaller for the rhomboid (minor loops for D1 and D2 are respectively 160 Oe and 85 Oe wide and escape fields are 43 Oe and 7 Oe respectively, ratios being therefore 0.27 and 0.16 respectively), while for elliptical rings, reducing the dimensions always increases the magnetostatic coupling [13]. This reduced magnetostatic coupling is therefore shape induced which may have been expected since the sharp corners in the rhomboidal geometry favor an easier reverse domain nucleation.

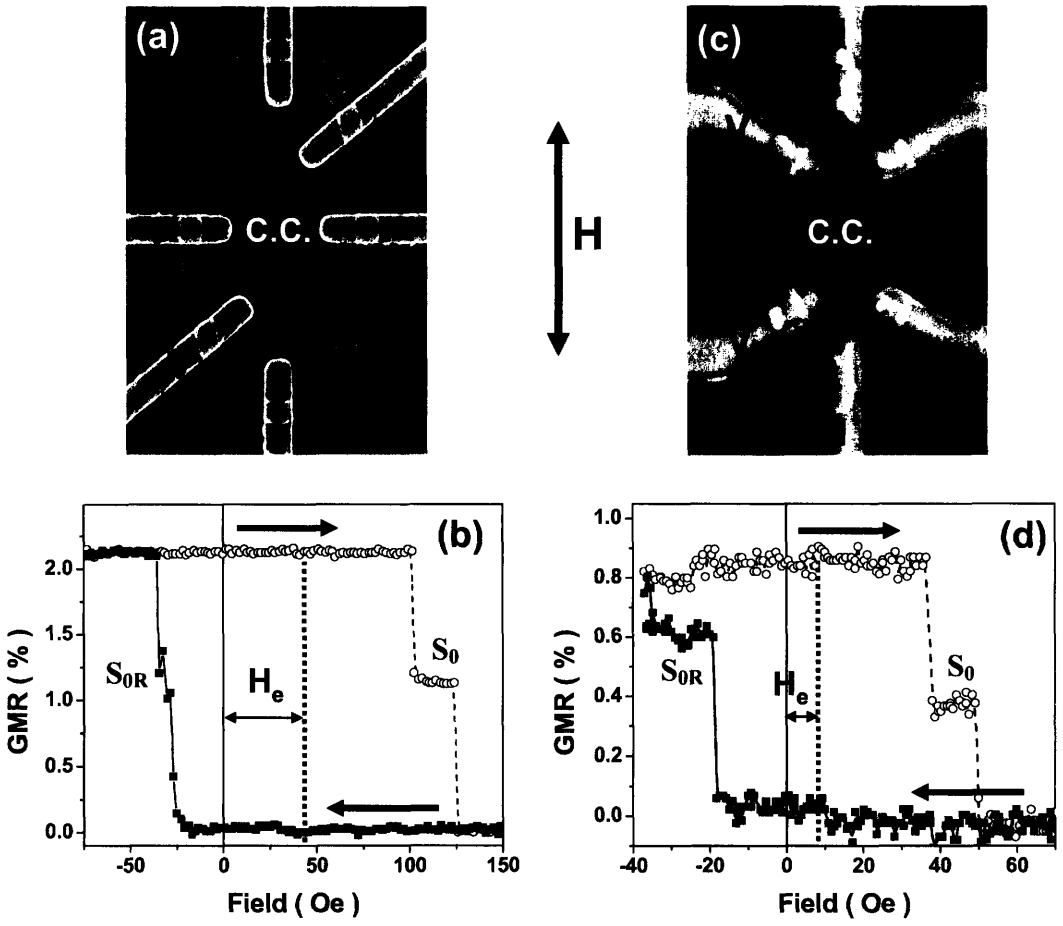

Figure 5.11: Minor loops for both devices in the C.C. with the cobalt in a forward onion state.

The behavior of both rings was also investigated when applying the field in the hard axis direction (Fig. 5.12). In the C.C. (Fig. 5.12.d), both devices display high and low resistance states, as well as an intermediate level in the reversal of the NiFe. However, while at remanence, D1 is still in a low resistance state, D2 is already in an intermediate state, which shows a stronger magnetostatic coupling effect in this hard axis direction due

to shape differences. Furthermore, only D2 shows a clear stable intermediate state for the reversal of the Co.

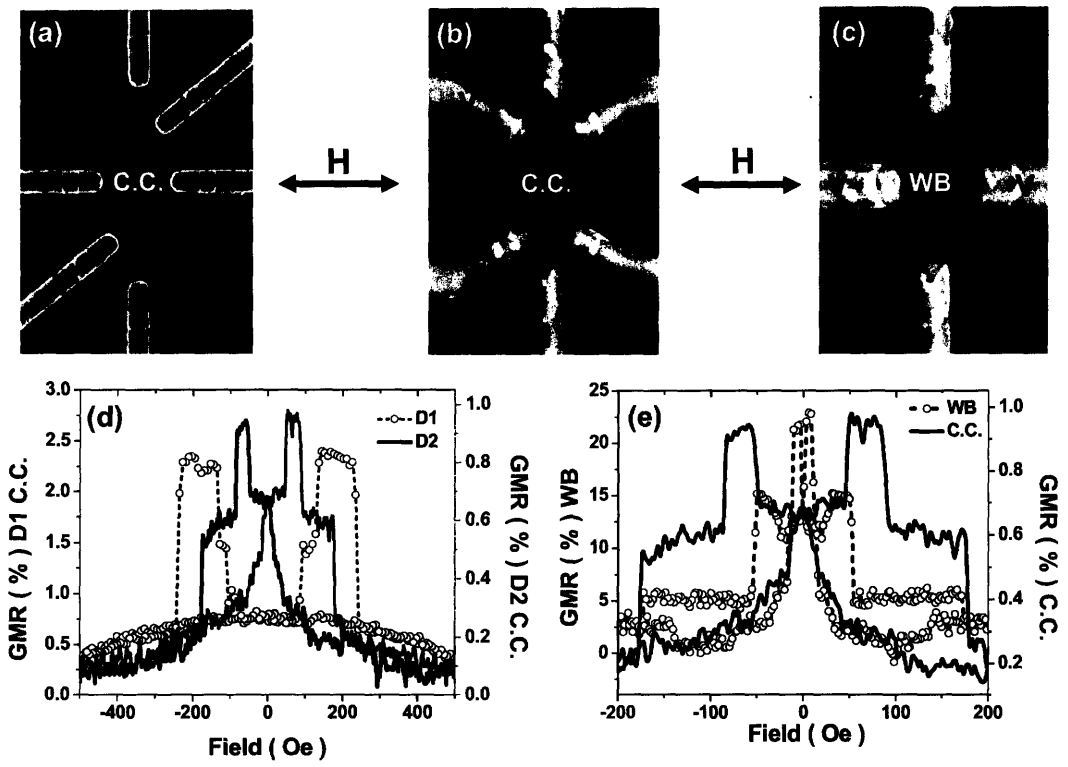

Figure 5.12 Scanning electron micrographs of D1 and D2 in a classical configuration (C.C.) (respectively (a) and (b)) and of D2 in a Wheatstone bridge (WB) configuration (c) with the corresponding GMR responses ((d) and (e)). The field is applied along the hard axis.

The correlation between the C.C. and WB configurations for D2 with the field applied along the hard axis (Fig 5.12.e) is very high: their switching fields can be unequivocally matched. It proves also that in the hard axis configuration, the soft layer switches very asymmetrically, while during the hard layer switching, much less asymmetry is observed, leading to lower resistance plateaus. Moreover, the WB curve shows a shift of ~ 40 % (Fig. 5.14.b) in GMR at very low fields ~ 3.5 Oe, which is a very interesting feature for CIMS.

Fig 5.13 shows the micromagnetic simulation results for D2 with the field applied in the hard axis direction. It allows us first to understand why the resistance is at an intermediate level at remanence (Fig. 5.13.b state S_i): after saturation, in the corners along the hard axis direction (which are not very sharp ~120°), in each ferromagnetic layer, walls of identical chirality are located on top of one another. Such walls will repel one another, because their stray fields add up. The walls in the NiFe will therefore simply propagate along the sides of the rhomboid, and they do so in an asymmetric fashion (Fig 5.13.b, S_{sat} to S_i). This process is energetically less demanding than in an elliptical ring because of the sharp 120° corners.

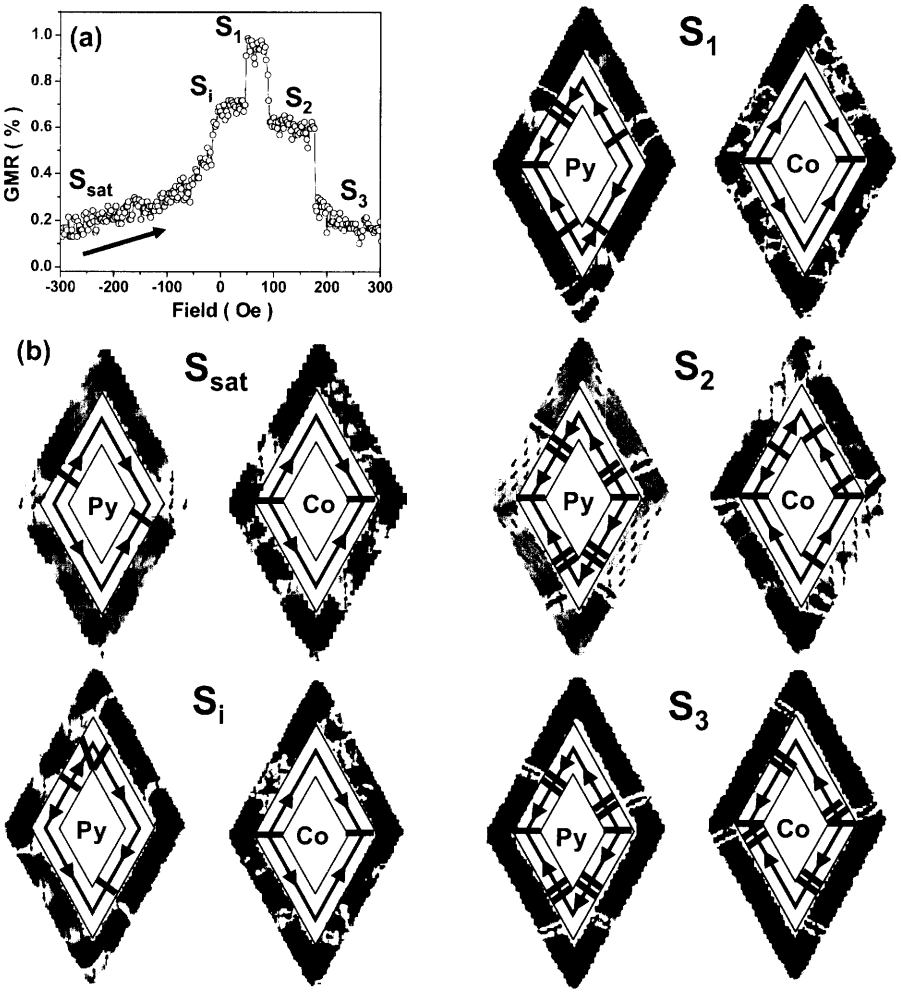

Figure 5.13: (a) A single GMR curve of D2 in C.C. with the field applied along the hard axis (b) Micromagnetic snapshots of both Co and NiFe layer in the S_{sat}, S_i, S_1, S_2, and S_3 states for the rhomboidal ring. The small arrows give the precise magnetization distribution and the schematics the overall domain structure.

The NiFe reverses through the propagation from both end of the short axis of domain walls, as well as through the nucleation of two reverse domains, whereas the Co reverses from the side branches, in a similar fashion as when the field was applied in the easy axis direction. These simulations also show the omnipresence of the 360° walls during the reversals processes in both layers, and their extraordinary stability, even at applied fields as high as 1500 Oe (Fig 5.13.b state S_3) during the simulation. This is experimentally verified through a series of measurements that showed that after very high saturation (3000 Oe), upon cycling the field below 1100 Oe, the return branch was a minor loop, displaying a completely different shape, and increasing the maximum GMR ratio up to 160 % (Fig. 5.14.b). When cycling with higher fields, the behavior became symmetric as expected, and the origin of the aforementioned minor loop behavior was determined: a slight shift in resistance ~ 0.03 Ω gradually occurred around 1000 Oe, and can be

ascribed, in the light of the simulations (Fig 5.13.b state S3) to the asymmetric distribution (especially in the Co) of 360° domain walls. This small shift in resistance (ΔR) is however a ~ 6 % change in effective GMR.

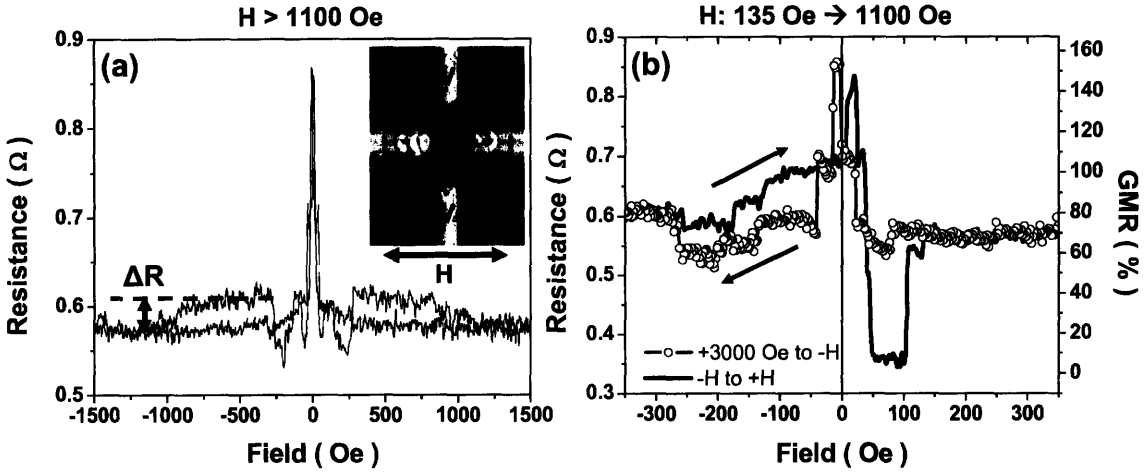

Figure 5.14: (a) A GMR curve of D2 in the WB configuration with a cycling field applied along the hard axis, with extrema values above 1100 Oe. (b) GMR curve upon sweeping the field below 1100 Oe after high positive saturation.

The field induced magnetization switching measurements and simulations in both contact configurations allowed for a good understanding of the magnetization reversal of the rhomboidal PSV ring. Furthermore, the Wheatstone Bridge contact configuration displayed very high effective GMR ratios as well as low switching fields, a very interesting combination that can be exploited for current induced magnetic switching.

5.4 Current induced measurements.

Fig. 5.15.a shows the minor loop of D1 in the easy axis WB configuration, upon saturating at high positive fields (3000 Oe) and cycling to -40 Oe (which is the little plateau at the top of the peak observed in Fig. 5.9.c) and then back up to +40 Oe. Interestingly, when cycling back from -40 Oe to + 40 Oe, a resistance shift to an intermediate value occurs at very low field ~ -1 Oe, while the complete reversal back to the forward onion state occurs at ~ + 18 Oe. For each of these two switchings (J_1 and J_2), CIMS measurements have been conducted, using exactly the same setting used in last chapter, with 100 μs long square current pulses. Bias fields of -3 Oe and +16 Oe were applied for J_1 and J_2 respectively, and the magnetization successfully switched in both cases with current densities of the same order as the one used for the notched bars ~ 10^{11} A/m^2. However, the reproducibility was poor, and therefore those two CIMS were not further investigated.

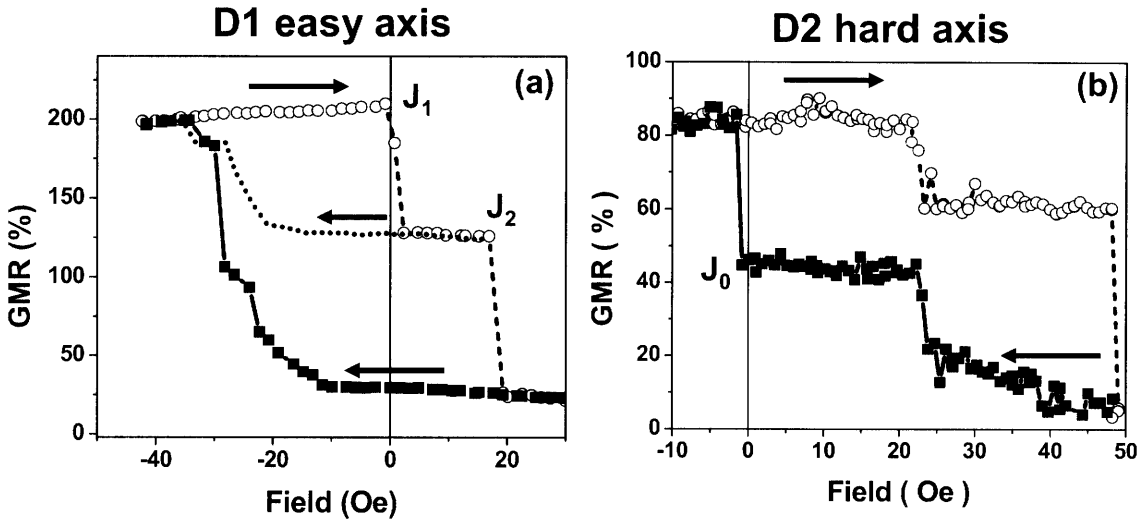

Figure 5.15: WB configuration minor loops with the Co in a forward onion state for D1 with the field applied in the easy axis direction (a) and for D2 in the hard axis direction (b). J_1, J_2, J_0 indicate the magnetization states at which current induced magnetic switchings were accomplished.

Fig. 5.15.b shows the minor loop of D2 in the hard axis WB configuration upon saturating at high positive fields (3000 Oe) and cycling to -10 Oe (which is the little plateau at the top of the first peak after remanence observed in Fig. 5.12.e) and then back up to +50 Oe. After high positive saturation, the field was brought back to remanence and was kept at zero. Successful CIMS was obtained at zero bias field for the first time in a ring device, with an effective GMR jump of ~ 40 % (J_0). Further work needs to be done on this particular configuration to study the reproducibility of such switching, as well as a potential ways to switch back with current the device to its original remanence state before the jump.

CIMS measurements in the elliptical ring in the WB configuration depicted in Fig. 5.8.a with a bias field of 49 Oe and an effective GMR change of ~ 20 % showed that the density of pulses was a determining factor in decreasing the critical current density: increasing the pulse density resulted in a consistently lower switching current. Fig 5.16 clearly illustrates that trend. Successive pulses of 100 μs were applied to the device with amplitudes gradually increasing: with a step of ~ 0.25 mA starting at 0.1 mA, the NiFe switches at ~2.33 mA (Fig. 5.16.a), while with a step of ~0.05 mA starting at 1 mA, it switches at 1.25 mA (Fig. 5.16.b). Interestingly, these switching currents correspond to the same cumulated number of electron having flowed through the cross section of the device which is proportional to the sum of the pulse amplitudes multiplied by the pulse length before the switching (~ 11.3 mA x 100 μs).

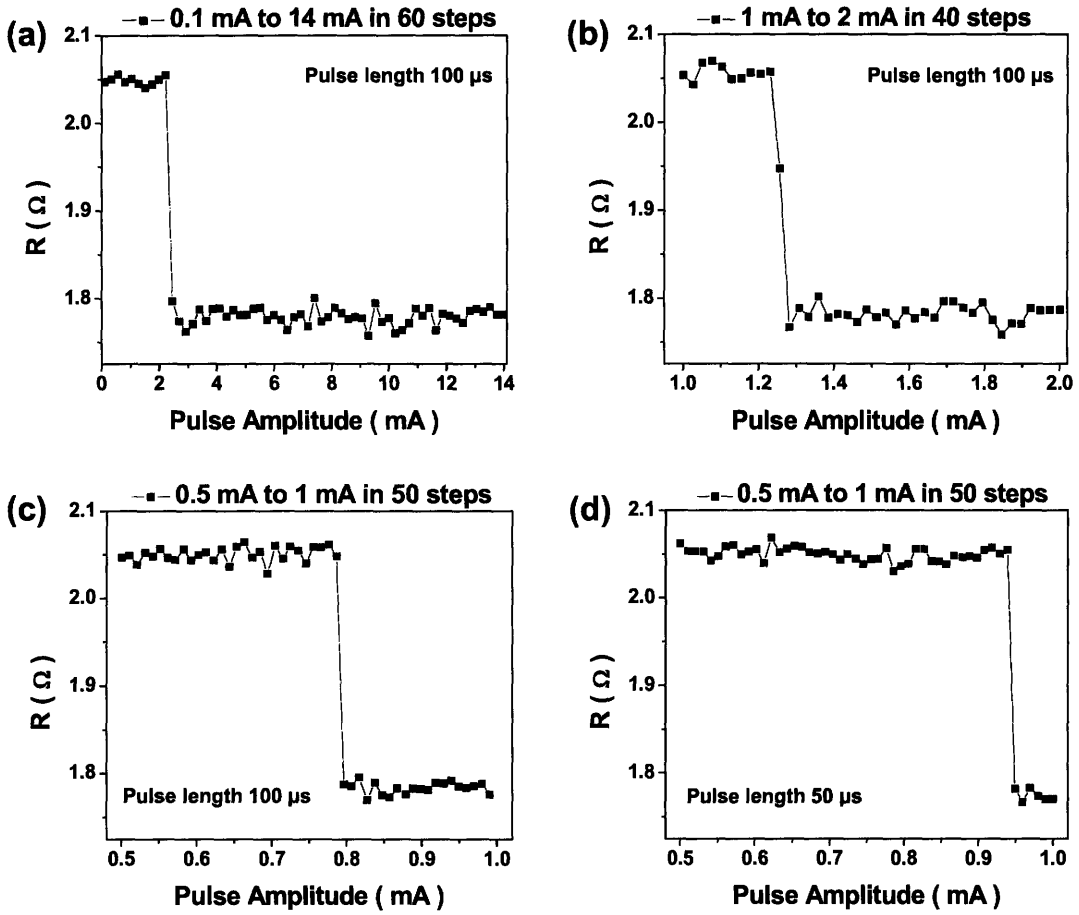

Figure 5.16: Resistance versus pulsed current measurements for D1 in the WB configuration described in Fig. 5.8.a for a positive bias field of + 49 Oe (after positive saturation of + 3000 Oe and an applied reverse field of -225 Oe to set the Co layer in its vortex state). The density of pulses increases from (a) to (b) and the pulse length is divided by two from (c) to (d).

This interpretation in term of cumulated electron flow is strengthened by the measurements shown in Fig. 5.16.c and Fig. 5.16.d, in which the pulse length was divided by two, from 100 µs to 50 µs respectively, while keeping an identical step ~ 0.01 mA and starting point: 0.5 mA. The switching current increased from ~ 0.79 mA to ~ 0.94 mA respectively, which corresponded to similar cumulative electron flows proportional to ~ 18.6 mA x 100 µs and ~ 31.7 mA x 50 µs respectively.

This indicates that the spin structure of the domain wall(s) present in the NiFe must be transformed by the spin polarized current most probably from transverse to vortex configuration, which decreases their effective pinning potential [20].

5.5 Summary.

The comparative study of the field induced magnetization reversal of elliptical and rhomboidal Pseudo Spin Valve rings has been conducted using different contact configurations and with the field applied both along the easy axis and hard axis. The measured giant magnetoresistance response combined with micromagnetic simulations allowed for the understanding of the magnetic reversal in both layers. While the response of rhomboidal rings seems to be similar to that of elliptical rings in the classical contact configuration, the process of the reversal is quite different as inferred by both the Wheatstone bridge contact configuration and the simulations, especially concerning the reversal of the hard Co layer and the large stability of the 360° domain walls. In the elliptical rings, the Co goes through an intermediate vortex state, whereas in the rhomboid, the Co reverses mainly from the center of the side branches, thus leading to a number of 360° domain walls. However, the soft NiFe layer reversed in a similar fashion in both devices, resulting in similar minor loops in the classical contact configuration showing the importance of magnetostatic coupling. Very large effective GMR ratios were obtained in the WB configuration in each device and the relative noise was decreased when going from the classical to the WB contact configuration. The WB configuration measured the asymmetry of the reversal in each layer and displayed low switching fields, which allowed for current induced magnetic switchings under low applied bias fields, even down to 0 Oe, with critical current densities of the order of 10^{11} A/m^2. If the Oersted field has been shown in last chapter to have an important part in the CIMS in PSV microstructures, it was proved here on the elliptical ring that the current modified the spin structure of the domain walls in the soft layer and thus decreased their pinning potential. If further characterized, this phenomenon could be integrated in a logic application using CIMS, in which the input would not be a single current pulse, but a precise sequence of current pulses.

[1] J. Rothman, M. Klaui, L. Lopez-Diaz, C. A. F. Vaz, A. Bleloch, J. A. C. Bland, Z. Cui, and R. Speaks, Phys. Rev. Lett. **86**, 1098 (2001).

[2] X. Zhu, PhD thesis, Mc Guill University , Canada (2002).

[3] S. P. Li, D. Peyrade, M. Natali, A. Lebib, Y. Chen, U. Ebels, L.D. Buba, and K. Ounadjela, Phys. Rev. Lett. **86**, 1102 (2001).

[4] Y. Chen, A. Lebib, S. P. Li, M. Natali, D. Peyrande, and E. Cambril, Microelectron. Eng. **57**, 405 (2001).

[5] F.J. Castaño, C. A. Ross, C. Frandsen, A. Eilez, D. Gil, H. I. Smith, M. Redjdal, and F. B. Humphrey, Phys. Rev. B **67**, 184425 (2003).

[6] F.J. Castaño, C. A. Ross, and A. Eilez, J. Phys. D **36**, 2031 (2003).

[7] F.J. Castaño, C. A. Ross, A. Eilez, W. Jung, Phys. Rev. B **69**, 144421 (2004).

[8] W. Jung, F. J. Castaño, C. A. Ross, R. Menon, A. Patel, E. E. Moon, and H. I. Smith, J. Vac. Sci. Technol. B **22** (6), 3335 (2004).

[9] F.J. Castaño, W. Jung, D. Morecroft, and C. A. Ross Phys. Rev. Lett. **95**, 137201 (2005).

[10] D. Morecroft, F.J. Castaño, W. Jung, J. Feuchtwanger, and C. A. Ross, Appl. Phys. Lett. **88**, 172508 (2006).

[11] C.A. Ross, F.J. Castaño, D. Morecroft, W. Jung, H. I. Smith, T. A. Moore, T. J. Hayward, J. A. C. Bland, T. J. Bromwich, and A. K. Petford-Long, J. Appl. Phys. **99**, 08S501 (2006).

[12] D. Morecroft, F.J. Castaño, W. Jung, and C. A. Ross, J. Appl. Phys. **99**, 08T104 (2006).

[13] F.J. Castaño, D. Morecroft, and C. A. Ross, Phys. Rev. B **74**, 224401 (2006).

[14] M. Klaui, C. A. F. Vaz, J. A. C. Bland, W. Wernsdorfer, G. Faini, and E. Cambril, Appl. Phys. Lett. **81**, 108 (2002).

[15] M-F. Lai, Z-H. Wei, C-R Chang, J. C. Wu, J. H. Kuo, and J-Y. Lai, Phys. Rev. B **67**, 104419 (2003).

[16] L.J. Heyderman, M. Klaui, B. Nohammer, C. A. F. Vaz, J. A. C. Bland, and C. David, Microelectron. Eng. **73-74**, 780 (2004).

[17] J Podbielski, F. Giesen, M. Berginski, N. Hoyer, and D. Grndler, Superlattices Microstruct. **37**, 341 (2005).

[18] D. Buntix, A. Volodin, and C. V. Haesendonck, Phys. Rev. B **70**, 224405 (2004).

[19] Y.G. Yoo, M. Klaui, C. A. F. Vaz, L. J. Heyderman, and J. A. C. Bland, Appl. Phys. Lett. **82**, 2470 (2003).

[20] J. He, Z. Li, and S. Zhang, J. Appl. Phys. **99**, 08G509 (2006).

Conclusion.

The fabrication and the field and current induced magnetization switchings of NiFe/Cu/Co/Au Pseudo-Spin-Valve devices have been investigated and discussed in this dissertation. Using four point probe GMR measurements combined with 3D micromagnetic modeling, the magnetic response of the devices to a field and/or a current was investigated. Different device geometries were defined: notched bars (2.14 μm long, 270 nm wide), an elliptical ring (4 μm-long easy axis, 2 μm-long hard axis and 210 nm wide) and rhomboidal rings (1.6 μm-long easy axis, a 900 nm-long hard axis and 140 nm wide). The magnetic behavior was dominated by shape anisotropy and magnetostatic coupling between the hard (Co) and soft (NiFe) layers. Interactions between current and local magnetization comprised spin-dependent scattering (GMR), Oersted field and spin transfer torque effects.

In the notched bars, the reversal of the soft NiFe layer is initiated from the ends of the bar under the influence of the magnetostatic field from the Co. Intermediate resistance states have been identified corresponding to the presence of domain walls in the notches. Domain wall movement was accomplished in both the soft and hard layers of the PSV using current densities of order 10^{11} A/m^2, in the presence of a biasing magnetic field. The threshold current density as the bias field increased, but in these samples current-induced reversal was not obtained with bias fields below 5 Oe. Reversal of the NiFe layer occurred either in a single step, or in a two-step process depending on the notch configuration and the direction of bias field and current. Current induced magnetization reversal of the Co layer occurred as a single step, for both current and bias field directions. These small bars showed significant magnetostatic interactions between the NiFe and Co layers, and effective pinning of domain walls at the notches. The reversal of the NiFe was driven primarily by the bias field, whilst the Oersted field from the current pulse promoted the reversal at bias fields below the switching field. In these small current-in-plane multilayer structures, modeling indicates that the Oersted field from the current pulse is sufficient to promote domain wall depinning in the soft layer, even in the absence of spin torque effects. The understanding of CIMS in bars was a first step towards the investigation of CIMS in ring structures.

The comparative study of the field induced magnetization reversal of elliptical and rhomboidal Pseudo Spin Valve rings has been conducted using different contact configurations and with the field applied either along the easy axis or along the hard axis. While the response of rhomboidal rings appears to be similar to that of elliptical rings in

the classical contact configuration, the process of the reversal is quite different as inferred from both the Wheatstone bridge contact configuration measurments and the simulations, especially concerning the reversal of the hard Co layer and the very large stability of the 360° domain walls. In the elliptical rings, the Co reverses through an intermediate vortex state, whereas in the rhomboid, the Co reverses mainly from the center of the side branches, thus leading to several 360° domain walls. However, the soft NiFe layer reversed in a similar fashion in both devices, resulting into similar minor loops in the classical contact configuration showing the importance of magnetostatic coupling. Very large effective GMR ratios were obtained in the WB configuration in each device and the relative noise was decreased when going from the classical to the WB contact configuration. The WB configuration measured the asymmetry of the reversal in each layer and displayed low switching fields, which allowed for current induced magnetic switchings under low applied bias fields, even down to 0 Oe, with critical current densities of the order of 10^{11} A/m^2. If the Oersted field has been shown to have an important part in the CIMS of multilayered structures, it was proved on the elliptical ring that the current also modified the spin structure of the domain walls in the soft layer and thus decreased their pinning potential.

Further work needs to be done on CIMS in ring structures, starting with a reproducibility test on the 0 Oe current induced switching in the rhomboidal ring set in a Wheatstone bridge configuration. The ultimate step would be to devise and optimize a ring geometry in which high effective GMR can be attained and in which the asymmetry of the NiFe layer reversal can be controlled, with low switching fields, multiple remanent states, and narrow minor loops thus allowing for current induced reverse switchings under 0 Oe. Such a device would be an ideal candidate for fast magnetic logic, displaying more than two states, and requiring low energy input currents. Work is currently in progress to test the field induced switching reproducibility in the low frequency dynamic range.

Intensive research on patterned magnetoresistive devices started during the late 90's with the discovery of GMR, and today, every computer uses a GMR read head. Most recently, MRAMs based on magnetoresistive cells were made commercially available by Freescale (2006). Considerable attention is focused today on improving the densities and device architectures in such memories. However, to this date, there is little work on magnetic sensors or integrated logic devices on the submicron scale. This thesis suggests that patterned magnetoresistive ring devices could be good candidates for fast logic gates as well as e.g. digital bio-sensors (recently collaborators at the Cavendish Laboratory have demonstrated that concept, using PSV ring devices that we fabricated at MIT [1]).

[1] J. Llandro, T.J. Hayward, D. Morecroft, J. A. C. Bland, F. J. Castaño, I. A. Colin, and C. A. Ross, submitted (April 2007).

Acknowledgements.

I would like to begin by expressing my deep gratitude to Professor Caroline Ross for giving me the opportunity to work in her group on such a great subject. My special thoughts go towards Dr. Fernando Castaño for being a tremendous mentor and friend, and I thank him for always keeping me motivated and positive. I also thank Wonjoon Jung and Filip Ilievski for being there when I needed some answers. Finally, I would like to thank all the members of the group, for their friendship and support.

APPENDIX A

Resolution of the hydrogen molecule in the Heitler-London model.

A.1. System and Hamiltonian.

The system consists of two protons considered as fixed in the Born-Oppenheimer approximation, and two electrons.

The Hamiltonian can be written:

$$\hat{H} = \frac{\hat{P}_1^2}{2m} - \frac{e^2}{\left|\vec{r}_1 - \vec{R}_1\right|} - \frac{e^2}{\left|\vec{r}_1 - \vec{R}_2\right|} + \frac{\hat{P}_2^2}{2m} - \frac{e^2}{\left|\vec{r}_2 - \vec{R}_2\right|} - \frac{e^2}{\left|\vec{r}_2 - \vec{R}_1\right|} + \frac{e^2}{\left|\vec{r}_1 - \vec{r}_2\right|} + \frac{e^2}{\left|\vec{R}_1 - \vec{R}_2\right|} \tag{A.1}$$

where capital lettered vectors indicate the position of the protons, and small ones the electrons. The last term is a constant and the one before last can be treated as a first order perturbation.

The electronic states will be described by a wave function associated with a given energy through the Schrödinger equation:

$$\hat{H}\left|\Psi\right\rangle = E\left|\Psi\right\rangle \tag{A.2}$$

where $\left|\Psi\right\rangle = \left|\Psi(\vec{r}_1, \sigma_1; \vec{r}_2, \sigma_2)\right\rangle$ is the wave function fully describing the electrons' state with σ_1 and σ_2 being the projections of the electron spins along a given z axis. Since the Hamiltonian contains no spin interaction term, the wave function of the electrons can be written as the tensor product between the space wave function and the spin wave function:

$$\left|\Psi(\vec{r}_1, \sigma_1; \vec{r}_2, \sigma_2)\right\rangle = \left|\Phi(\vec{r}_1; \vec{r}_2)\right\rangle \otimes \left|\mathrm{X}(\sigma_1; \sigma_2)\right\rangle \tag{A.3}$$

A.2. Pauli Exclusion Principle and wave functions.

The Pauli exclusion principle states that for fermions (here two electrons), the wave function solution of the Schrödinger equation must be **asymmetric when interchanging the electrons**. Therefore :

$$\left|\Psi(\vec{r}_2,\sigma_2;\vec{r}_1,\sigma_1)\right\rangle = -\left|\Psi(\vec{r}_1,\sigma_1;\vec{r}_2,\sigma_2)\right\rangle \tag{A.4}$$

A symmetric space function must therefore be associated with an asymmetric spin function and vice versa.

Since

$$\left[\hat{H},S_z\right]=\left[\hat{H},S^2\right]=0 \tag{A.5}$$

adding two ½ spins will lead to four spin wave functions:

The **Singlet** state

$$\mathrm{X}_S=\frac{1}{\sqrt{2}}\left(\left|\uparrow\downarrow\right\rangle-\left|\downarrow\uparrow\right\rangle\right) \tag{A.6}$$

with $S=S_z=0$. This function is asymmetric with respect to electron interchange.

The three **Triplet** states $S=1$ which are symmetric when interchanging electrons

$$\mathrm{X}_T=\left|\uparrow\uparrow\right\rangle \tag{A.7}$$

with $S_z=1$

$$\mathrm{X}_T=\frac{1}{\sqrt{2}}\left(\left|\uparrow\downarrow\right\rangle+\left|\downarrow\uparrow\right\rangle\right) \tag{A.8}$$

with $S_z=0$

$$\mathrm{X}_T=\left|\downarrow\downarrow\right\rangle \tag{A.9}$$

with $S_z=-1$

Since the total wave function must be asymmetric, the space function associated with the Singlet spin function must be symmetric Φ_S, and the one associated with the Triplet states must be asymmetric Φ_A.

Let φ_1 and φ_2 be the normalized spatial wave functions of the electrons 1 and 2 respectively when the two protons are infinitely apart, not interacting (i.e. hydrogen atom ground state 1s):

$$\hat{H}_i\left|\varphi_i(\vec{r}_i)\right\rangle=\left(\frac{\hat{P}_i^2}{2m}-\frac{e^2}{\left|\vec{r}_i-\vec{R}_i\right|}\right)\left|\varphi_i(\vec{r}_i)\right\rangle=E_0\left|\varphi_i(\vec{r}_i)\right\rangle \tag{A.10}$$

Since φ_1 and φ_2 are not orthogonal, when the atoms come closer, φ_1 and φ_2 overlap:

$$\gamma = \left| \int \varphi_1^*(\vec{r}) \varphi_2(\vec{r}) d^3\vec{r} \right| > 0 \tag{A.11}$$

See the last section of that appendix for an actual calculus of that integral.

As long as we do not consider the excited states of the two atoms, the space two-electron wave functions can be written:

$$\Phi_S(\vec{r}_1, \vec{r}_2) = \frac{1}{\sqrt{2\left(1+\gamma^2\right)}} \left[\varphi_1(\vec{r}_1)\varphi_2(\vec{r}_2) + \varphi_1(\vec{r}_2)\varphi_2(\vec{r}_1) \right] \tag{A.12}$$

$$\Phi_A(\vec{r}_1, \vec{r}_2) = \frac{1}{\sqrt{2\left(1-\gamma^2\right)}} \left[\varphi_1(\vec{r}_1)\varphi_2(\vec{r}_2) - \varphi_1(\vec{r}_2)\varphi_2(\vec{r}_1) \right] \tag{A.13}$$

A.3. Eigenvalues and discussion.

The energies are:

$$E_{\uparrow\downarrow} = E_S = \left\langle \Phi_S(\vec{r}_1, \vec{r}_2) \middle| \hat{H} \middle| \Phi_S(\vec{r}_1, \vec{r}_2) \right\rangle \tag{A.14}$$

$$E_{\uparrow\uparrow} = E_A = \left\langle \Phi_A(\vec{r}_1, \vec{r}_2) \middle| \hat{H} \middle| \Phi_A(\vec{r}_1, \vec{r}_2) \right\rangle \tag{A.15}$$

$$\boxed{E_{\uparrow\downarrow} = 2E_0 + \frac{U+V}{1+\gamma^2}} \tag{A.16}$$

$$\boxed{E_{\uparrow\uparrow} = 2E_0 + \frac{U-V}{1-\gamma^2}} \tag{A.17}$$

with

$$U = \int \left(H - H_1 - H_2\right) \left|\varphi_1(\vec{r}_1)\right|^2 \left|\varphi_2(\vec{r}_2)\right|^2 d^3\vec{r}_1 d^3\vec{r}_2 \tag{A.18}$$

$$V = \int \left(H - H_1 - H_2\right) \left(\varphi_1^*(\vec{r}_1)\varphi_2^*(\vec{r}_2)\varphi_2(\vec{r}_1)\varphi_1(\vec{r}_2)\right) d^3\vec{r}_1 d^3\vec{r}_2 \tag{A.19}$$

where H_i is defined in (A.10)

The first term in (A.16) and (A.17) corresponds to the total energy of the electrons if the atoms are infinitely separated, and the following terms correspond to the first order perturbation corrections when coulomb forces between the two atoms are taken into account in the singlet spin configuration (A.16) and the triplet (A.17).

The hydrogen molecule will form (in the ground state) if one of these energies is lower than $2E_0$ for some value of the interatomic distance $r = \left|\vec{R}_1 - \vec{R}_2\right|$. Only $E_{\uparrow\downarrow}$ does show a minimum below $2E_0$:

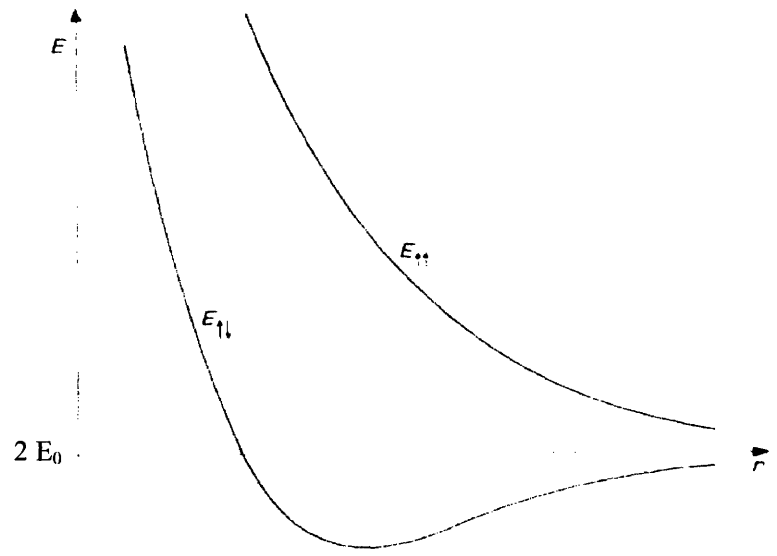

Therefore the hydrogen molecule will be formed, but only if the spins are antiparallel (singlet state), thus forming an antiferromagnetic 'solid'.

A.4. Introduction of the spin Hamiltonian.

If we ignore the higher energy states, it is possible to introduce a spin Hamiltonian whose eigenvalues will be the same as the original one in (A.1), but which shall act only on the spin component of the eigenfunctions and therefore whose eigenfunctions will give the total spin of the corresponding state.

Since for each electron $\hat{S}_i^2 = s_i(s_i+1) = \frac{1}{2}\left(\frac{1}{2}+1\right) = \frac{3}{4}$, then for the two-electron system,

$$\hat{S}^2 = \left(\hat{\vec{S}}_1 + \hat{\vec{S}}_2\right)^2 = \frac{3}{2} + 2\hat{\vec{S}}_1 \bullet \hat{\vec{S}}_2 \qquad \text{(A.20)}$$

Moreover, the eigenvalue of $\hat{S}^2$ is $S(S+1)$, then $\hat{\vec{S}}_1 \bullet \hat{\vec{S}}_2$ has eigenvalue $-\frac{3}{4}$ for the singlet state, and $+\frac{1}{4}$ for the triplet states. Therefore, a spin Hamiltonian thus defined :

$$\hat{H} = \frac{1}{4}\left(E(r)_{\uparrow\downarrow} + 3E(r)_{\uparrow\uparrow}\right) - \left(E(r)_{\uparrow\downarrow} - E(r)_{\uparrow\uparrow}\right)\hat{\vec{S}}_1 \bullet \hat{\vec{S}}_2 \qquad \text{(A.21)}$$

will wave the same pairs of eigenvalue eigenfunctions as the original one.

Resetting the energy origin, we can write:

$$\boxed{\hat{H} = -J(r) \cdot \hat{\vec{S}}_1 \bullet \hat{\vec{S}}_2} \qquad \text{(A.22)}$$

where $J(r) = E(r)_{\uparrow\downarrow} - E(r)_{\uparrow\uparrow}$. This exchange Hamiltonian will favor parallel spins if $J(r)$ is positive and antiparallel if $J(r)$ and negative.

A.5. Calculus of $\gamma = \left| \int \varphi_1^*(\vec{r}) \varphi_2(\vec{r}) d^3\vec{r} \right|$

In this model, each wave function is a 1s hydrogen wave function:

$$\varphi_i(\vec{r}) = \frac{e^{-\frac{r_i}{a_0}}}{\sqrt{a_0^3 \pi}}$$

where r_i is the distance between the electron and the ith nucleus and a_0 the Bohr radius.

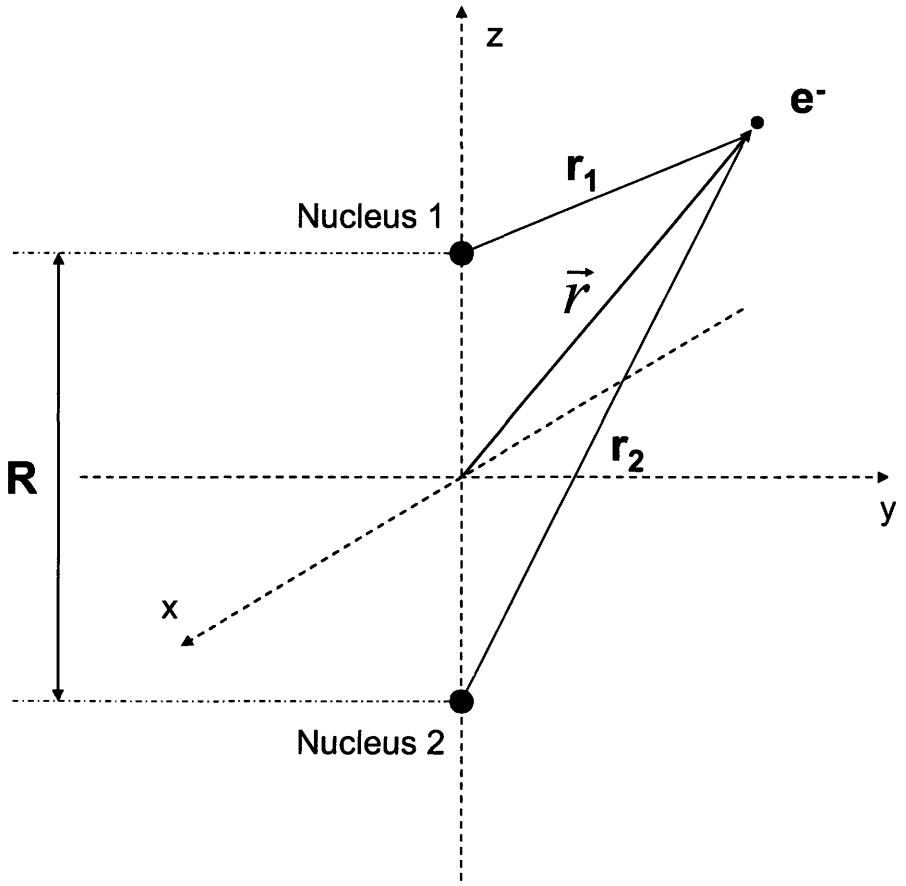

$$\gamma = \int \frac{e^{-\frac{r_1+r_2}{a_0}}}{a_0^3\pi} d^3\vec{r} = \iiint \frac{e^{-\frac{\sqrt{\left(x^2+y^2+\left(z-\frac{R}{2}\right)^2\right)}+\sqrt{\left(x^2+y^2+\left(z+\frac{R}{2}\right)^2\right)}}{a_0}}}{a_0^3\pi} dxdydz$$

This integral becomes easily solvable if we make a change of coordinate into the prolate spheroid coordinate system:

$x = R'\sinh(u)\sin(v)\cos(\phi)$
$y = R'\sinh(u)\sin(v)\sin(\phi)$
$z = R'\cosh(u)\cos(v)$

with $u \in [0;+\infty]$, $v \in [0;2\pi]$ and $\phi \in [0;2\pi]$

The scaling factors are:

$h_u = h_v = R'\sqrt{\sinh^2(u)+\sin^2(v)}$

$h_\phi = R'\sinh(u)\sin(v)$

Using $\cos^2(\alpha)+\sin^2(\alpha)=1$ and $\cosh^2(\alpha)-\sinh^2(\alpha)=1$

$$r_1+r_2 = \frac{R}{2}\sqrt{\left(\sinh^2(u)\sin^2(v)+\left(\cosh(u)\cos(v)-1\right)^2\right)}+\frac{R}{2}\sqrt{\left(\sinh^2(u)\sin^2(v)+\left(\cosh(u)\cos(v)+1\right)^2\right)}$$

where $R' = \frac{R}{2}$ has been set.

$$r_1+r_2 = \frac{R}{2}\sqrt{\left(\cosh(u)-\cos(v)\right)^2}+\frac{R}{2}\sqrt{\left(\cosh(u)+\cos(v)\right)^2}$$

Remembering that $\cosh(\alpha) \geq 1$,

$r_1+r_2 = R\cosh(u)$

The integral becomes:

$$\gamma = \iiint_{u,v,\phi} \frac{e^{-\frac{R\cosh(u)}{a_0}}}{8a_0^3\pi} R^3 \sinh(u)\sin(v)\left(\sinh^2(u)+\sin^2(v)\right) dudvd\phi$$

Integrating over v and ϕ is straightforward.

$$\gamma = \int_{u=0}^{+\infty} \frac{e^{-\frac{R\cosh(u)}{a_0}}}{2a_0^3} R^3 \left(\frac{2}{3}\sinh(u) + \sinh^3(u) \right) du$$

The first term of that integral is straightforwardly integrable, the second requires two successive steps of integration by parts.

$$\gamma = \left[-\frac{R^2}{3a_0^2} e^{\frac{R\cosh(u)}{a_0}} \right]_0^{+\infty} + \left[-\frac{R^2}{2a_0^2}\sinh^2(u) e^{\frac{R\cosh(u)}{a_0}} \right]_0^{+\infty} + \left[-\frac{R}{a_0}\cosh(u) e^{\frac{R\cosh(u)}{a_0}} \right]_0^{+\infty} + \left[-e^{\frac{R\cosh(u)}{a_0}} \right]_0^{+\infty}$$

$$\boxed{\gamma = e^{-\frac{R}{a_0}} \left(1 + \frac{R}{a_0} + \frac{R^2}{3a_0^2} \right)}$$

APPENDIX B

Proof of

$$E_{magnetostatic} = -\frac{\mu_0}{2}\int_{sample} \vec{H}_{demag}(\vec{r}) \bullet \vec{M}(\vec{r}) dV = \frac{\mu_0}{2}\int_{space} H^2_{demag}(\vec{r}) dV$$

First, since the magnetization is zero outside the sample, the first integral can be done over all space. We then decompose:

$$\vec{H}_{demag}(\vec{r}) \bullet \vec{M}(\vec{r}) = -\vec{\nabla}\Phi(\vec{r}) \bullet \vec{M}(\vec{r}) = \Phi(\vec{r}) \cdot \vec{\nabla} \bullet \vec{M}(\vec{r}) - \vec{\nabla}\left(\Phi(\vec{r}) \cdot \vec{M}(\vec{r})\right)$$

From Maxwell's equation we have

$$\vec{\nabla} \bullet \vec{M}(\vec{r}) = \vec{\nabla} \bullet \left(\frac{\vec{B}}{\mu_0} - \vec{H}_{demag}\right) = -\vec{\nabla} \bullet \vec{H}_{demag}$$

So we can further decompose:

$$-\Phi(\vec{r}) \cdot \vec{\nabla} \bullet \vec{H}_{demag}(\vec{r}) = \vec{\nabla}\Phi(\vec{r}) \bullet \vec{H}_{demag}(\vec{r}) - \vec{\nabla}\left(\Phi(\vec{r}) \cdot \vec{H}_{demag}(\vec{r})\right) = -\vec{H}^2_{demag}(\vec{r}) - \vec{\nabla}\left(\Phi(\vec{r}) \cdot \vec{H}_{demag}(\vec{r})\right)$$

In the end:

$$E_{magnetostatic} = -\frac{\mu_0}{2}\int_{space} \left(-\vec{\nabla}\left(\Phi\vec{M} + \Phi\vec{H}_{demag}\right) - H^2_{demag}\right) dV$$

Let us prove that

$$\int_{space} \vec{\nabla}\left(\Phi\vec{M}\right) dV = 0$$

$$\int_{space} \vec{\nabla}\left(\Phi\vec{H}_{demag}\right) dV = 0$$

Let us consider a large sphere of radius R at which center the sample is placed and that is equivalent from that distance to a dipole moment $\vec{m} = \vec{M}V$ along the z axis.

Obviously from the Stokes relation,

$$\int_{Sphere} \vec{\nabla} \bullet \left(\vec{\mathrm{T}}\right) dV = \iint_{Surface} \vec{\mathrm{T}} \bullet \vec{n} \cdot dS \xrightarrow[R \to +\infty]{} \int_{Space} \vec{\nabla} \bullet \left(\vec{\mathrm{T}}\right) dV$$

Since the magnetization is zero outside the sample and therefore on the surface of any sphere containing the sample, $\int_{space} \vec{\nabla}\left(\Phi \vec{M}\right) dV = 0$

Now for the last one, far from the sample, the dipole field approximation can be made:

$$\iint_{Surface} \Phi \vec{H}_{demag} \bullet \vec{n} \cdot dS = \int_{\varphi=0}^{2\pi} \int_{\theta=0}^{\pi} \Phi(R,\theta,\varphi) \vec{H}_{demag}(R,\theta,\varphi) \bullet \vec{e}_r \cdot R^2 \sin(\theta) d\theta d\varphi$$

where $\Phi(R,\theta,\varphi) = \frac{\vec{m} \bullet \vec{R}}{4\pi R^3}$ and $\vec{H}_{demag}(R,\theta,\varphi) = -\frac{\left(3\left(\vec{m} \bullet \vec{R}\right)\vec{R} - R^2 \vec{m}\right)}{4\pi R^5}$

so

$$\iint_{Surface} \Phi \vec{H}_{demag} \bullet \vec{n} \cdot dS = -\frac{1}{(4\pi)^2} \int_{\varphi=0}^{2\pi} \int_{\theta=0}^{\pi} \frac{2\left(\vec{m} \bullet \vec{R}\right)^2}{R^5} \sin(\theta) d\theta d\varphi$$

$$\iint_{Surface} \Phi \vec{H}_{demag} \bullet \vec{n} \cdot dS = -\frac{m^2}{4\pi R^3} \int_{\theta=0}^{\pi} \cos^2(\theta) \sin(\theta) d\theta d\varphi$$

We then obtain:

$$\iint_{Surface} \Phi \vec{H}_{demag} \bullet \vec{n} \cdot dS = -\frac{m^2}{4\pi R^3} \left[-\cos^3(\theta)\right]_0^{\pi} = -\frac{m^2}{2\pi R^3}$$

and

$$-\frac{m^2}{2\pi R^3} \xrightarrow[R \to +\infty]{} 0$$

And therefore

$$\int_{space} \vec{\nabla}\left(\Phi \vec{H}_{demag}\right) dV = 0$$

So in the end we proved that

$$\boxed{E_{magnetostatic} = \frac{\mu_0}{2} \int_{space} H_{demag}^2 dV}$$

APPENDIX C

Calculus of the demagnetizing field inside a uniformly magnetized sphere, using the same notations as in section 2.1.3.2.

At the center of the sphere, $\vec{r} = \vec{0}$, and equation 2.26 can be written:

$$\vec{H} = \frac{1}{4\pi}\iint \frac{\vec{M}\bullet\vec{n}}{R^3}(-\vec{r}\,')d^2S = \frac{1}{4\pi}\int_{\varphi=0}^{2\pi}\int_{\theta=0}^{\pi} -\frac{M_0\cos(\theta)}{R^3}\mathrm{R}\vec{\mathrm{e}}_R\, R^2\sin(\theta)d\theta d\varphi$$

With $R\ \ \theta\ \ \varphi$ being the spherical coordinates of any point on the surface of the sphere.

And since $\vec{e}_R = \sin(\theta)\cos(\varphi)\vec{e}_x + \sin(\theta)\sin(\varphi)\vec{e}_y + \cos(\theta)\vec{e}_z$

$$\vec{H} = -\frac{M_0}{4\pi}\int_{\varphi=0}^{2\pi}\int_{\theta=0}^{\pi}\cos(\theta)\sin(\theta)\cdot\begin{vmatrix}\sin(\theta)\cos(\varphi)\\ \sin(\theta)\sin(\varphi)\\ \cos(\theta)\end{vmatrix}\cdot d\theta d\varphi$$

Since $\int_0^{2\pi}\sin(\varphi)d\varphi = \int_0^{2\pi}\cos(\varphi)d\varphi = 0$

$$\vec{H} = -\frac{M_0}{4\pi}\int_{\varphi=0}^{2\pi}\int_{\theta=0}^{\pi}\cos^2(\theta)\sin(\theta)\cdot d\theta\cdot d\varphi\vec{e}_z = -\frac{M_0}{2}\left[-\frac{\cos^3(\theta)}{3}\right]_0^{\pi}\vec{e}_z = -\frac{M_0}{3}\vec{e}_z$$